Theoretical study on adiabatic and non-adiabatic dynamics of argon cluster ions

アルゴンクラスターイオンの
断熱・非断熱過程の理論的研究

IKEGAMI, Tsutomu

池　上　　努

①

学位論文

Theoretical study on adiabatic and non-adiabatic dynamics of argon cluster ions

(アルゴンクラスターイオンの断熱・非断熱過程の理論的研究)

平成 8 年 8 月 博士 (理学) 申請
東京大学大学院理学系研究科 化学専攻

池上 努
IKEGAMI, Tsutomu

Acknowledgment

The present work is started when the author joined Kondow group at the university of Tokyo, where he was engaged in the experiment of the photodissociation of cluster ions. The author would like to express his sincere appreciation to Professor T. Kondow, for his kind guidance and comment throughout this work. The author is also grateful to Professor T. Nagata. Most of the author's knowledge on vacuum experiments of molecular systems came from him. Another gratitude will be sent to Professor T. Tahara, whose attitude to science has influenced the author. Thanks are due to Dr. S. Nonose, Dr. J. Hirokawa, Dr. F. Mafune, Dr. M. Nagamine, Dr. T. Sugai, Dr. T. Tsukuda, Dr. M. Ichihashi, Dr. Y. Takeda, Dr. H. Yasumatu, Dr. H. Yoshida, and all other members of the laboratory, for their valuable advice and fellowship.

In order to estimate the position of the photoabsorption band for cluster ions, the author was suggested to do *ab initio* calculations. Since then, collaboration with Iwata group at Keio university started, and eventually he got a position there. The author wishes to express his unfeigned thankfulness to Professor S. Iwata, for his considerate supervision and criticism on the work. The author also greatly appreciated the hearty encouragement of Professor K. Kaya. Acknowledgment should go to Professor M. A. Johnson at Yale University, for his empathic consultation when the author was in two mind whether to move to Keio University or not. The author is also thankful to Professor M. Tsukada for his valuable advice at the very beginning of the theoretical calculations. Another gratitude will be sent to Dr. S. Sekine: he was kind enough to introduce the author to the basic UNIX operation and *ab initio* programs. Thanks are due to Professor A. Nakajima, Dr. H. Matsuzawa, Dr. S. Nanbu, Mr. Y. Ueno, Mr. J. Irisawa, and all other members in Iwata group and Kaya group, as well as all the staffs in the Department of Chemistry, for their meaningful remarks and warm hospitality.

The Iwata group has moved to Institute for Molecular Science (IMS) on 1994. The author also joined the theoretical groups at IMS. The author acknowledges very useful and stimulating discussion with the members at IMS. Thanks are due to Dr. S. Ten-no, Mr. T. Tsurusawa, Dr. T. Asada, Professor H. Someda, Professor A. Shudo, Dr. S. Takada, Dr. N. Tomita, Mr. K. Nobusada, and others. The author also thanks Professor S. Yabushita at Keio University for the valuable suggestion.

Finally, the author will acknowledge the following computational and financial supports. The first program code written on a personal computer was transported to a RISC workstation borrowed from Kubota INC. It was then transported to the TKYVAX computer at the University of Tokyo meson science laboratory (UTMSL), and most of the works on the static properties were done on this machine. The *ab initio* calculation on Ar_3^+ cluster ion was performed on HITAC M-680 at the computer center of IMS. A part of the work was supported by the Grant-in-Aid for Scientific Research from Ministry of Education, Science and Culture (Nos. 0423102, 05453024, 04243104, and 07240229).

Contents

Chapter 1

General introduction

A cluster is an aggregate of atoms or molecules, isolated in the gas phase. The motivation for the cluster science originates from both fields of molecules and condensed matter. From the molecule point of view, the cluster is an augmented molecule, which is large enough that the statistics starts to play an essential role. The cluster is also viewed as downsized liquid/solid, which are manageable with sophisticated calculations developed for molecular systems. Recent advance in the vacuum and the laser technologies has enabled us to generate, separate, and investigate the clusters, and many works have been carried out on such cluster systems. Thanks to those studies, the cluster starts to unveil its own face: the cluster is a small scale many-body system, and taking it as augmented molecules or downsized liquid/solid is somewhat misleading.

Besides the conventional physical parameters such as volume and internal energy, the cluster has another dimension: the number of the components within the cluster, which is usually referred as "cluster size". Some physical observables of the cluster are strongly dependent on the cluster size. The stability of the cluster is a representative example that manifests the size dependency. If a cluster with a specific size is stabler than the others, its abundance observed in the mass spectra becomes large, and is referred as "magic number".

In the cluster systems, the stability does not correspond directly to the enthalpy for the cluster dissociation. A "stable" cluster here is a cluster that has a long life time. In a typical case, the binding energy of the cluster is smaller than its internal energy. Due to the limited degrees of freedom of the cluster, a sufficient amount of the internal energy may be condensed in an internal mode related to the dissociation via a fluctuation. In that sense, the cluster is not an isolated system but is even an open system, as its components may be changed through evaporation. Based on the model of the evaporating clusters, the relative dissociation enthalpy can be deduced from the rate of the evaporation.

It is a common method to deposit energy into a cluster and to pursue the following process, for studying the dynamics of the cluster such as an evaporation process. The energy deposition is performed through photoexcitation or collision with inert gas, being followed by photodissociation or collision-induced dissociation (CID). From a theoretical point of view, the treatment of the dynamics is confronted by several difficulties. In homogeneous clusters, basic electronic structures of its components are the same by definition, which are interacting with each other. Therefore, the electronic system of the cluster itself is heavily degenerated. The Born-Oppenheimer approximation breaks down and many potential energy surfaces start to couple together. Those electronic surfaces must be obtained at the same accuracy, as many electronic potential surfaces are involved in the dynamics. Secondly, non-adiabatic couplings between the potential surfaces must be calculated, which require electronic wavefunctions. Therefore, the pair-wise additive model potentials are not appropriate. And lastly, the full quantum treatment of the non-adiabatic process requires unrealistic amount of computational effort. A part of the degrees of freedom in the cluster should be treated classically, though the partitioning is not straightforward.

In this work, several difficulties in the theoretical treatment of the cluster are tackled taking an argon cluster

ion as an example. In Chapter 2, an electronic Hamiltonian for the argon cluster ion is discussed. The most widely used method on the calculation of electronic states is the *ab initio* molecular orbital method. Along with the recent amazing advance in the computer technology, the *ab initio* method has successfully widened its applicability. However, the calculation of the electronic states involved in the dynamics of the cluster is still beyond its scope. For example, Ar_{20}^{+} has 60 electronic states within 5 eV from the ground state, and calculation of whole of them is almost impossible even as a single point calculation. Instead of leaning on the *ab initio* method, an electronic Hamiltonian is constructed by using the empirical method based on the valence bond theory. The Hamiltonian for the large cluster is built from an available information on potential energy surfaces of the small cluster by using the chemical intuition of the valence bond structure. Roughly speaking, the Hamiltonian thus constructed corresponds to an effective CI matrix in the *ab initio* word. All the 3p valence hole states in the argon cluster ion are calculated equivalently. Analytical expressions for derivatives of the potential energy surfaces and non-adiabatic coupling vector are also derived for a further use in the dynamical calculation.

In Chapter 3, static properties of the argon cluster ion is discussed. The properties include the most stable structure on the ground potential energy surface and transition energies to excited states. At the most stable structure, whole charge in the cluster is localized on a few atoms forming an ion core, which acts as a strong chromophore. In other words, the ion core is solvated in the rest of the neutral argon atoms. A quantitative method to evaluate the solvation interaction energy for a certain electronic state of the ion core is presented there. The experimentally observed spectral shift of the argon cluster ion is explained in terms of the solvation effect on the ion core.

In Chapter 4, dynamics of the argon cluster ion in the electronic ground state is discussed. Because of large degrees of freedom, there are many local minima on the potential energy surface. The ground minimum only gives a representative structure of the cluster ion , and it is not suitable to estimate experimental observables from it. However, it is almost impossible to locate all of the minima, unless the size of the cluster is very small. The local minima may be connected through higher order stationary points, and isomerization among them may occur frequently. Those strong unharmonicity of the potential surface makes it hard to acquire correct statistics from stationary points only, even though all of them are obtained.

In the argon cluster ion, the interaction of solvent atoms with the ion core is site-specific, so that variation of the solvation shell may be important. Instead of finding local minima and taking statistical average over them, the molecular dynamics (MD) calculation is performed to simulate the photoabsorption spectra of the argon cluster ion. The formula to calculate the photoabsorption cross section from the MD structures are also derived here.

In Chapter 5, non-adiabatic dynamics, allowing transition between different adiabatic states, is discussed, based on the photodissociation process of the cluster ion. The photodissociation process starts from the elec-

tronic ground state, which absorbs light and promotes to an excited state. Evaporation of argon atoms from the cluster follows, releasing its excess energy of the parent cluster. A smaller cluster in its electronic ground state is left after the evaporation. This implies that the transition from the photoexcited state to the ground state should take place somewhere during the photodissociation process. The photodissociation process is too rapid for the radiative relaxation to proceed, so that non-adiabatic transition should play an important role.

There have been no works reported on the studies of non-adiabatic processes in complex systems such as clusters. One problem is in obtaining many electronic potential surfaces, which are coupled together and take roles in the non-adiabatic dynamics. The other problem is in the algorithm to manage the non-adiabatic transition. The full quantum calculation is not tractable due to the large degrees of freedom. The conventional surface hopping trajectory method gives one solution, but it requires *a priori* information on the location of avoided crossings, which is not available for complex systems.

Here, the effective Hamiltonian described in Chapter 2 are combined with Tully's surface hopping trajectory method. The effective Hamiltonian makes it possible to calculate whole the electronic states, while the Tully's method enables us to treat non-adiabatic processes consistently without any *a priory* knowledge on the system except for the electronic Hamiltonian. The underlying concept in the Tully's method is discussed, and modification of the procedure is proposed for ease of the calculation. The method is applied for the photodissociation process of Ar_3^+ and Ar_7^+, as examples for the simple and complex photodissociation processes, respectively.

Chapter 2

Electric hamiltonian

Abstract

Construction of an electronic Hamiltonian for the system of the argon cluster ion is described here. The diatomics-in-molecules (DIM) method is employed, in which the total Hamiltonian is represented as the sum of atomic and diatomic Hamiltonians. Because of this structure of the DIM Hamiltonian, the derivatives of its matrix elements with respect to the nuclear coordinates are readily obtained. The gradient of the potential energy surfaces, the non-adiabatic coupling vectors, and the Hessian matrices may be calculated from these derivatives. An electric dipole operator is also defined in the DIM fashion. Some of the potential surfaces and the transition moments are compared with *ab initio* results for Ar_3^+.

2.1 DIM model Hamiltonian

The Born-Oppenheimer electronic Hamiltonian of a molecule is written in the atomic unit system as

$$\mathcal{H} = -\sum_i \frac{1}{2}\nabla_i^2 - \sum_A \sum_i \frac{Z_A}{r_{Ai}} + \sum_{i<j} \sum \frac{1}{r_{ij}} + \sum_{A<B} \sum \frac{Z_A Z_B}{r_{AB}}, \tag{2.1}$$

where the subscript i and j denote electron in the molecule, A and B are the index to the constituent atoms, and Z_A is the nuclear charge of the atom A. In the DIM formalism, the Hamiltonian above is divided into the sum of the atomic and the diatomic Hamiltonians [1],

$$\mathcal{H} = \sum_{A>B}^{n} \sum \mathcal{H}^{AB} - (n-2) \sum_A^n \mathcal{H}^A, \tag{2.2}$$

where $\mathcal{H}^{AB}$ and $\mathcal{H}^A$ are diatomic and atomic Hamiltonians, respectively, and n is the size of the cluster, Ar_n^+. By use of Eq. 2.2, the total Hamiltonian matrix can be constructed from the atomic and diatomic Hamiltonian matrices with a set of appropriate basis functions.

2.1.1 Basis set

A set of many-electron wavefunctions $\{\Xi_A^w\}$ is employed as a basis set to calculate the matrix elements of the Hamiltonian for Ar, Ar^+, Ar_2 and Ar_2^+. The wavefunction Ξ_A^w represents the state with a hole at the p_w orbital of the A-th atom of Ar_n^+, and is approximated as [2]

$$\Xi_A^w = S_1 S_2 \cdots P_A^w \cdots S_n, \qquad (1 \le A \le n,\, w = x, y, z), \tag{2.3}$$

where the subscripts are the index to the of Ar atoms in Ar_n^+. The functions P_A^w and S_i $(i = 1 \ldots n)$ are assumed to be the *exact* wavefunctions of Ar^+ with the symmetry of p_w and those of Ar, respectively. The spin-orbit interaction is ignored in this representation, though it is easily incorporated semiempirically [3]. The excited states of Ar and Ar^+ are not considered, as those states are beyond the energy scope of the current interest. Within the DIM framework, the orthonormality among the basis functions is premised to be valid [1].

2.1.2 Atomic and diatomic Hamiltonian

As the basis functions Ξ_A^w are the product of the atomic wavefunctions, the atomic Hamiltonian matrix is readily obtained from the experimental value:

$$\langle \Xi_A^w | \mathcal{H}^C | \Xi_B^v \rangle = \begin{cases} \mathrm{IP(Ar)}\delta_{AC} & (A = B \text{ and } w = v) \\ 0 & (\text{otherwise}) \end{cases}, \tag{2.4}$$

Here, IP(Ar) is the ionization energy of an argon atom (15.76 eV), and δ_{AC} is the Kronecker's delta. The total electronic energy of n neutral Ar atoms is taken as the origin of the energy.

The matrix elements for the diatomic Hamiltonian are as follows:

$$\langle \Xi_A^w | \mathcal{H}^{CD} | \Xi_B^v \rangle = \begin{cases} H^{AB}_{AwBv} & (\{A,B\} = \{C,D\}) \\ \mathrm{ArDN}(R_{CD}) & (A = B \text{ and } v = w \text{ and } A \notin \{C,D\}) \\ 0 & (\text{otherwise}) \end{cases} , \tag{2.5}$$

where ArDN(R) is a potential energy function of the neutral dimer Ar_2 ($^1\Sigma_g^+$), R_{CD} is a distance between atoms C and D, and H^{AB} is a Hamiltonian matrix of the dimer ion Ar_2^+. The potential curve proposed by Watts and McGee [4] is used for the ArDN(R).

$$\mathrm{ArDN}(R) = \epsilon \left[\exp\{\alpha(1-r)\} \sum_{i=0}^{5} A_i (r-1)^i - \sum_{i=0}^{2} \frac{C_{2i+6}}{r^{2i+6} + \delta} \right] \tag{2.6}$$

$$r = \frac{R}{R_m} \tag{2.7}$$

A_0	0.278	C_6	1.107	ϵ/k_B (K)	142.1
A_1	-4.504	C_8	0.170	R_m (Å)	3.761
A_2	-8.331	C_{10}	0.013	σ (Å)	3.361
A_3	-25.27				
A_4	-102.0			α	12.5
A_5	-113.3			δ	0.01

The Hamiltonian matrix H^{AB} is calculated from the potential curves of the dimer ion Ar_2^+. Within the electronic space spanned by the basis set $\{\Xi_A^w\}$, there are six electronic states for Ar_2^+: $^2\Sigma_u^+$, $^2\Pi_u$, $^2\Pi_g$, and $^2\Sigma_g^+$ with two Π state doubly degenerated. These electronic states are expanded by using the simple picture of the valence-bond theory as

$$^2\Sigma_u^+ = \frac{1}{\sqrt{2}}(\Upsilon_A^z + \Upsilon_B^z) \tag{2.8}$$

$$^2\Pi_u{}^x = \frac{1}{\sqrt{2}}(\Upsilon_A^x + \Upsilon_B^x) \tag{2.9}$$

$$^2\Pi_u{}^y = \frac{1}{\sqrt{2}}(\Upsilon_A^y + \Upsilon_B^y) \tag{2.10}$$

$$^2\Pi_g{}^x = \frac{1}{\sqrt{2}}(\Upsilon_A^x - \Upsilon_B^x) \tag{2.11}$$

$$^2\Pi_g{}^y = \frac{1}{\sqrt{2}}(\Upsilon_A^y - \Upsilon_B^y) \tag{2.12}$$

$$^2\Sigma_g^+ = \frac{1}{\sqrt{2}}(\Upsilon_A^z - \Upsilon_B^z), \tag{2.13}$$

where the basis set $\{\Upsilon_A^w\}$ is same as $\{\Xi_A^w\}$, but quantized in the direction to the body fixed coordinate of the dimer AB, taking the molecular axis as z-axis. Rewriting Eq. 2.8~2.13, a set of the wavefunctions

$$\Psi_{AB} \equiv \{^2\Sigma_u^+, {}^2\Pi_u{}^x, {}^2\Pi_u{}^y, {}^2\Pi_g{}^x, {}^2\Pi_g{}^y, {}^2\Sigma_g^+\} \tag{2.14}$$

is connected to the basis set

$$\Upsilon_{AB} \equiv \{\Upsilon^x_A, \Upsilon^y_A, \Upsilon^z_A, \Upsilon^x_B, \Upsilon^y_B, \Upsilon^z_B\} \tag{2.15}$$

via an unitary transformation U:

$$\Psi_{AB} = \Upsilon_{AB} U, \tag{2.16}$$

$$U = \frac{1}{\sqrt{2}} \begin{pmatrix} 0 & 1 & 0 & 1 & 0 & 0 \\ 0 & 0 & 1 & 0 & 1 & 0 \\ 1 & 0 & 0 & 0 & 0 & 1 \\ 0 & 1 & 0 & -1 & 0 & 0 \\ 0 & 0 & 1 & 0 & -1 & 0 \\ 1 & 0 & 0 & 0 & 0 & -1 \end{pmatrix}. \tag{2.17}$$

The Hamiltonian matrix H^{AB} becomes diagonal in the space spanned by Ψ_{AB}, and its diagonal elements are the potential energy of the electronic state of the dimer ion Ar_2^+. The matrix H^{AB} in the Υ_{AB} space is then calculated as

$$H^{AB}_{\Upsilon} = \left(\begin{array}{c|c} Q & J \\ \hline J & Q \end{array}\right), \tag{2.18}$$

$$Q = \begin{pmatrix} Q_p & 0 & 0 \\ 0 & Q_p & 0 \\ 0 & 0 & Q_s \end{pmatrix}, \tag{2.19}$$

$$J = \begin{pmatrix} J_p & 0 & 0 \\ 0 & J_p & 0 \\ 0 & 0 & J_s \end{pmatrix}, \tag{2.20}$$

$$Q_s = \frac{1}{2}(E(^2\Sigma_u^+) + E(^2\Sigma_g^+)) \tag{2.21}$$

$$Q_p = \frac{1}{2}(E(^2\Pi_u) + E(^2\Pi_g)) \tag{2.22}$$

$$J_s = \frac{1}{2}(E(^2\Sigma_u^+) - E(^2\Sigma_g^+)) \tag{2.23}$$

$$J_p = \frac{1}{2}(E(^2\Pi_u) - E(^2\Pi_g)), \tag{2.24}$$

where $E()$'s are the potential energy for the corresponding electronic states of the dimer ion Ar_2^+, and are the functions of the internuclear distance between A and B.

When the molecular axis of the dimer AB is aligned to

$$(x, y, z) \equiv (\sin\theta\cos\phi, \sin\theta\sin\phi, \cos\theta), \tag{2.25}$$

the set Υ_{AB} is transformed from the space fixed basis set Ξ_{AB},

$$\Xi_{AB} \equiv \{\Xi_A^x, \Xi_A^y, \Xi_A^z, \Xi_B^x, \Xi_B^y, \Xi_B^z\}, \tag{2.26}$$

by rotating θ around the y-axis, and then rotating ϕ around the z-axis. The corresponding unitary operator is

$$\mathcal{R} = \exp(-i\mathcal{L}_z\phi)\exp(-i\mathcal{L}_y\theta), \tag{2.27}$$

where $\mathcal{L}_y$ and $\mathcal{L}_z$ are the angular momentum operator. As $\{\Xi_A^w\}$ are the product of the atomic wavefunctions (see Eq. 2.3), the matrix representation of $\mathcal{R}$ is readily calculated as

$$R = \left(\begin{array}{c|c} C(\theta,\phi) & 0 \\ \hline 0 & C(\theta,\phi) \end{array}\right), \tag{2.28}$$

$$C(\theta,\phi) = \begin{pmatrix} \cos\theta\cos\phi & -\sin\phi & \sin\theta\cos\phi \\ \cos\theta\sin\phi & \cos\phi & \sin\theta\sin\phi \\ -\sin\theta & 0 & \cos\theta \end{pmatrix}, \tag{2.29}$$

$$\Upsilon_{AB} = \Xi_{AB} R. \tag{2.30}$$

Finally, H^{AB} in the Ξ_{AB} space is given as follows:

$$H^{AB} = R \cdot H_{\Upsilon}^{AB} \cdot R^{-1} = \left(\begin{array}{c|c} M & N \\ \hline N & M \end{array}\right), \tag{2.31}$$

$$M(\text{or } N) = \begin{pmatrix} f_1 & f_2 & f_3 \\ f_2 & f_4 & f_5 \\ f_3 & f_5 & f_6 \end{pmatrix}, \tag{2.32}$$

$$f_1 = p + (s-p)x^2 \tag{2.33}$$

$$f_2 = (s-p)xy \tag{2.34}$$

$$f_3 = (s-p)zx \tag{2.35}$$

$$f_4 = p + (s-p)y^2 \tag{2.36}$$

$$f_5 = (s-p)yz \tag{2.37}$$

$$f_6 = p + (s-p)z^2, \tag{2.38}$$

where (x, y, z) are defined in Eq. 2.25, p and s are Q_p and Q_s (or J_p and J_s for the matrix N), respectively.

The potential energy curves of Ar_2^+ are calculated by using *ab initio* method. The HF-SCF calculation is performed on the neutral Ar_2 to obtain a set of molecular orbitals (MO). The MIDI4* (4321/421/1) basis set

is used in the calculation, taking the exponent in the diffuse function as 0.68. The POL-CI method is then applied using the MO set to calculate the four electronic states of Ar_2^+. In making reference configurations, the 1s, 2s, and 2p orbitals are frozen, and the rest of 15 electrons are arbitrarily packed into 3s and 3p orbitals. The POL-CI space is generated by exciting 3p electron in the reference configuration into unoccupied orbitals. A dimension of the CI calculations is $150 \sim 170$. The calculated potential energies are interpolated by using the third order natural spline functions, and used in the calculation of Eqs. 2.21~2.24. The obtained potential curves are shown in Fig. 2.1.

2.2 Gradient of the potential energy surface

In order to optimize the geometry of the cluster efficiently, or to obtain the forces exerted on the nuclei, the analytic gradient of the potential energy surface in terms of the nuclear coordinates is indispensable. The derivative of the potential energy surface for an electronic eigen state with respect to a nuclear coordinate is written as

$$\frac{\partial V_i}{\partial Q_a} = \frac{\partial}{\partial Q_a}\langle\Psi_i|\mathcal{H}|\Psi_i\rangle, \tag{2.39}$$

where Q_a is one of the nuclear coordinate, which behaves parametrically in $\mathcal{H}$, and Ψ_i is the i-th eigenfunction of $\mathcal{H}$, $\mathcal{H}\Psi_i = V_i\Psi_i$. The right hand side of Eq. 2.39 becomes

$$\begin{aligned} \text{r.h.s.} &= \langle\Psi_i|\frac{\partial\mathcal{H}}{\partial Q_a}|\Psi_i\rangle + V_i\left(\langle\frac{\partial\Psi_i}{\partial Q_a}|\Psi_i\rangle + \langle\Psi_i|\frac{\partial\Psi_i}{\partial Q_a}\rangle\right) &(2.40)\\ &= \langle\Psi_i|\frac{\partial\mathcal{H}}{\partial Q_a}|\Psi_i\rangle. &(2.41)\end{aligned}$$

The last equation is approved as Ψ_i is normalized:

$$\begin{aligned} 1 &= \langle\Psi_i|\Psi_i\rangle &(2.42)\\ 0 &= \langle\frac{\partial\Psi_i}{\partial Q_a}|\Psi_i\rangle + \langle\Psi_i|\frac{\partial\Psi_i}{\partial Q_a}\rangle. &(2.43)\end{aligned}$$

Using the diabaticity of the basis set,

$$\langle\Xi_A^w|\frac{\partial}{\partial Q_a}|\Xi_B^v\rangle = 0, \tag{2.44}$$

the matrix elements of $\frac{\partial\mathcal{H}}{\partial Q_a}$ may be calculated from the derivatives of the matrix elements of $\mathcal{H}$,

$$\frac{\partial}{\partial Q_a}\langle\Xi_A^w|\mathcal{H}|\Xi_B^w\rangle = \langle\Xi_A^w|\frac{\partial\mathcal{H}}{\partial Q_a}|\Xi_B^w\rangle. \tag{2.45}$$

Therefore, the gradient of the potential energy can easily be evaluated if the analytical derivatives of the matrix elements are known.

The DIM Hamiltonian matrix H, which is the matrix representation of $\mathcal{H}$, has $3n \times 3n$ elements, and each of them has to be differentiated with any of $3n$ nuclear coordinates. Since H is represented as a sum of atomic and

diatomic Hamiltonian matrices, the derivatives of the matrix elements can be decomposed into those of each *fragment* matrix. The derivative of the atomic *fragment* matrix, H^A, turns out to be zero, as H^A is a constant diagonal matrix (Eq. 2.4). The diatomic *fragment* matrix for a given pair $A-B$, H^{AB}, has $3(n-2)+36$ non-zero elements (Eq. 2.5). These elements are the functions of R_{AB}, which is the internuclear distance between A and B. The first $3(n-2)$ elements are the diagonal elements for the basis function Ξ_C^v ($C \neq A, B$), and are calculated from Eq. 2.5 as

$$\frac{\partial \mathrm{ArDN}}{\partial X_A} = \frac{\partial \mathrm{ArDN}}{\partial R_{AB}} x \tag{2.46}$$

$$\frac{\partial \mathrm{ArDN}}{\partial Y_A} = \frac{\partial \mathrm{ArDN}}{\partial R_{AB}} y \tag{2.47}$$

$$\frac{\partial \mathrm{ArDN}}{\partial Z_A} = \frac{\partial \mathrm{ArDN}}{\partial R_{AB}} z, \tag{2.48}$$

where (X_A, Y_A, Z_A) is the position of the atom A, and (x, y, z) is the unit vector directing from B to A. The derivative with respect to the position of the atom B merely changes the signs of the equations above. The rest of 36 elements are those of the 6×6 submatrix for Ξ_C^v ($C = A$ and B; $v = x$, y, and z), whose elements are given in Eqs. 2.31~2.38. The derivatives of the elements with respect to the position of the atom A are given as follows:

$$\frac{\partial f_1}{\partial X_A} = kx^3 + (p' - 2w)x \tag{2.49}$$

$$\frac{\partial f_1}{\partial Y_A} = kx^2 y + p' y \tag{2.50}$$

$$\frac{\partial f_1}{\partial Z_A} = kx^2 z + p' z \tag{2.51}$$

$$\frac{\partial f_2}{\partial X_A} = kx^2 y - wy \tag{2.52}$$

$$\frac{\partial f_2}{\partial Y_A} = kxy^2 - wx \tag{2.53}$$

$$\frac{\partial f_2}{\partial Z_A} = kxyz \tag{2.54}$$

$$\frac{\partial f_3}{\partial X_A} = kx^2 z - wz \tag{2.55}$$

$$\frac{\partial f_3}{\partial Y_A} = kxyz \tag{2.56}$$

$$\frac{\partial f_3}{\partial Z_A} = kxz^2 - wx \tag{2.57}$$

$$\frac{\partial f_4}{\partial X_A} = kxy^2 + p'x \tag{2.58}$$

$$\frac{\partial f_4}{\partial Y_A} = ky^3 + (p' - 2w)y \tag{2.59}$$

$$\frac{\partial f_4}{\partial Z_A} = ky^2 z + p' z \tag{2.60}$$

$$\frac{\partial f_5}{\partial X_A} = kxyz \tag{2.61}$$
$$\frac{\partial f_5}{\partial Y_A} = ky^2z - wz \tag{2.62}$$
$$\frac{\partial f_5}{\partial Z_A} = kyz^2 - wy \tag{2.63}$$

$$\frac{\partial f_6}{\partial X_A} = kxz^2 + p'x \tag{2.64}$$
$$\frac{\partial f_6}{\partial Y_A} = kyz^2 + p'y \tag{2.65}$$
$$\frac{\partial f_6}{\partial Z_A} = kz^3 + (p' - 2w)z, \tag{2.66}$$

where

$$w = \frac{p - s}{R_{AB}} \tag{2.67}$$
$$s' = \frac{\partial s}{\partial R_{AB}} \tag{2.68}$$
$$p' = \frac{\partial p}{\partial R_{AB}} \tag{2.69}$$
$$k = s' - p' + 2w. \tag{2.70}$$

The derivatives in terms of the position of the atom B are given by changing the sign of the formulae.

2.3 Non-adiabatic coupling vector

A non-adiabatic coupling vector is a basic parameter when we consider molecular dynamics beyond the Born-Oppenheimer approximation. It is also required in a calculation of a Hessian matrix for potential surfaces. The non-adiabatic coupling vector between two eigen functions of an electronic Hamiltonian, Ψ_i and Ψ_j, is defined as

$$d_{ij} \equiv \langle \Psi_i | \nabla | \Psi_j \rangle, \tag{2.71}$$

where ∇ is a differential operator with respect to nuclear coordinates. The vector d_{ij} may be calculated without differentiating the wavefunction, which is usually a time consuming process. As Ψ_i and Ψ_j are the eigen functions of the Hermitian,

$$0 = \langle \Psi_i | \mathcal{H} | \Psi_j \rangle \tag{2.72}$$

is approved for $i \neq j$. Applying $\frac{\partial}{\partial Q_a}$ operator on both side of Eq. 2.72, we get

$$0 = V_j \langle DoD\Psi_i Q_a | \Psi_j \rangle + V_i \langle \Psi_i | \frac{\partial \Psi_j}{\partial Q_a} \rangle + \langle \Psi_i | \frac{\partial \mathcal{H}}{\partial Q_a} | \Psi_j \rangle \tag{2.73}$$
$$= (V_i - V_j) \langle \Psi_i | \frac{\partial}{\partial Q_a} | \Psi_j \rangle + \langle \Psi_i | \frac{\partial \mathcal{H}}{\partial Q_a} | \Psi_j \rangle, \tag{2.74}$$

where V_i and V_j are the eigen values of Ψ_i and Ψ_j, respectively, and Q_a is an arbitrary nuclear coordinate. The last equation is approved from the orthonormality of the eigen functions, $\langle\Psi_i|\Psi_j\rangle = 0$. Therefore, the nonadiabatic couplings are calculated from the derivatives of the Hamiltonian as

$$d_{ij} = -\frac{\langle\Psi_i|\nabla\mathcal{H}|\Psi_j\rangle}{V_i - V_j}. \tag{2.75}$$

For the case of $i = j$, d_{ii} becomes a pure imaginary and can not be calculated from the above formula. It is, however, not required in the following calculations.

2.4 Hessian of the potential energy surface

To survey potential surfaces and to find the stationary points on them, the Hessian matrix for the potential surface is a powerful tool. Elements of the Hessian matrix for the surface of the i-th electronic eigen state are written in general as

$$\frac{\partial^2 V_i}{\partial Q_a \partial Q_b} = \frac{\partial}{\partial Q_a}\frac{\partial}{\partial Q_b}\langle\Psi_i|\mathcal{H}|\Psi_i\rangle, \tag{2.76}$$

where Q_a and Q_b are arbitrary nuclear coordinates, which appear in the $\mathcal{H}$ as parameters, and Ψ_i is the i-th eigen function of the electronic Hamiltonian $\mathcal{H}$, $\mathcal{H}\Psi_i = V_i\Psi_i$. The right side of Eq. 2.76 is expanded as

$$\text{r.h.s.} = \frac{\partial}{\partial Q_a}\langle\Psi_i|\frac{\partial\mathcal{H}}{\partial Q_b}|\Psi_i\rangle \tag{2.77}$$

$$= \langle\frac{\partial\Psi_i}{\partial Q_a}|\frac{\partial\mathcal{H}}{\partial Q_b}|\Psi_i\rangle + \langle\Psi_i|\frac{\partial\mathcal{H}}{\partial Q_b}|\frac{\partial\Psi_i}{\partial Q_a}\rangle + \langle\Psi_i|\frac{\partial^2\mathcal{H}}{\partial Q_a\partial Q_b}|\Psi_i\rangle. \tag{2.78}$$

Inserting an identical operator, $\mathbf{1} \equiv \sum_k |\Psi_k\rangle\langle\Psi_k|$, into Eq. 2.78, we get

$$\text{r.h.s.} = \sum_k \left\{ \langle\frac{\partial\Psi_i}{\partial Q_a}|\Psi_k\rangle\langle\Psi_k|\frac{\partial\mathcal{H}}{\partial Q_b}|\Psi_i\rangle + \langle\Psi_i|\frac{\partial\mathcal{H}}{\partial Q_b}|\Psi_k\rangle\langle\Psi_k|\frac{\partial\Psi_i}{\partial Q_a}\rangle \right\} + \langle\Psi_i|\frac{\partial^2\mathcal{H}}{\partial Q_a\partial Q_b}|\Psi_i\rangle. \tag{2.79}$$

From the orthonormality of $\{\Psi_k\}$, we can deduce that the operator $\frac{\partial}{\partial Q_a}$ behaves as an anti-hermitian,

$$\langle\Psi_j|\Psi_k\rangle = \delta_{ij} \tag{2.80}$$

$$\langle\frac{\partial\Psi_j}{\partial Q_a}|\Psi_k\rangle + \langle\Psi_j|\frac{\partial\Psi_k}{\partial Q_a}\rangle = 0 \tag{2.81}$$

$$\langle\Psi_j|\frac{\partial}{\partial Q_a}|\Psi_k\rangle = -\langle\Psi_k|\frac{\partial}{\partial Q_a}|\Psi_j\rangle^*, \tag{2.82}$$

where * denotes taking a complex conjugate. Meanwhile, $\frac{\partial\mathcal{H}}{\partial Q_a}$ is a hermitian: applying $\frac{\partial}{\partial Q_a}$ to $\langle\Psi_j|\mathcal{H}|\Psi_k\rangle$, we get

$$\langle Psi_j|\frac{\partial\mathcal{H}}{\partial Q_a}|\Psi_k\rangle = \frac{\partial}{\partial Q_a}\langle\Psi_j|\mathcal{H}|\Psi_k\rangle + (V_k - V_j)\langle\Psi_j|\frac{\partial}{\partial Q_a}|\Psi_k\rangle \tag{2.83}$$

and then, exchanging subscripts j and k, and using the anti-hermiticy of the operator $\frac{\partial}{\partial Q_a}$, we get

$$\langle Psi_k|\frac{\partial\mathcal{H}}{\partial Q_a}|\Psi_j\rangle = \frac{\partial}{\partial Q_a}\langle\Psi_j|\mathcal{H}|\Psi_k\rangle^* + (V_j - V_k)\left(-\langle\frac{\partial\Psi_k}{\partial Q_a}|\Psi_j\rangle\right) \tag{2.84}$$

$$= \langle Psi_j|\frac{\partial\mathcal{H}}{\partial Q_a}|\Psi_k\rangle^*. \tag{2.85}$$

Using these relations, Eq. 2.79 becomes

$$\text{r.h.s.} = \sum_k 2\Re\left\{\langle\Psi_i|\frac{\partial\mathcal{H}}{\partial Q_b}|\Psi_k\rangle\langle\Psi_k|\frac{\partial}{\partial Q_a}|\Psi_i\rangle\right\} + \langle\Psi_i|\frac{\partial^2\mathcal{H}}{\partial Q_a\partial Q_b}|\Psi_i\rangle, \tag{2.86}$$

where the function $\Re(x)$ gives a real part of x. We can drop the term $k = i$, as it gives a pure imaginary number inside $\{\}$. Inserting Eq. 2.75 into 2.86, we get the final expression of

$$\frac{\partial^2 V_i}{\partial Q_a\partial Q_b} = -\sum_{k\neq i}\Re\left\{\frac{\langle\Psi_i|\frac{\partial\mathcal{H}}{\partial Q_b}|\Psi_k\rangle\langle\Psi_k|\frac{\partial\mathcal{H}}{\partial Q_a}|\Psi_i\rangle}{V_k - V_g}\right\} + \langle\Psi_i|\frac{\partial^2\mathcal{H}}{\partial Q_a\partial Q_b}|\Psi_i\rangle. \tag{2.87}$$

Using the diabaticity of the basis set, the matrix representation of $\frac{\partial^2\mathcal{H}}{\partial Q_a\partial Q_b}$ is calculated from the Hessian of the matrix element of $\mathcal{H}$;

$$\langle\Xi_A^w|\frac{\partial^2\mathcal{H}}{\partial Q_a\partial Q_b}|\Xi_B^v\rangle = \frac{\partial^2}{\partial Q_a\partial Q_b}\langle\Xi_A^w|\mathcal{H}|\Xi_B^v\rangle. \tag{2.88}$$

There are $3n\times 3n$ elements in the Hamiltonian matrix, and the Hessian matrix of $3n\times 3n$ dimension should be calculated for each element. By virtue of the structure of the DIM Hamiltonian, the Hessian of the Hamiltonian matrix may be calculated from the Hessian of the atomic and the diatomic Hamiltonian matrices. The atomic part vanishes as it is a constant matrix (see Eq. 2.4). The diatomic part, H^{AB}, has $3(n-2)+36$ non-zero elements. These elements are the functions of the internuclear distance R_{AB}, so that there are only $6x6$ non-zero elements in the Hessian of the element. The first $3(n-2)$ elements are the diagonal elements for Ξ_C^w, $C\neq A$ or B, and whose Hessian is given as follows:

$$\frac{\partial^2\text{ArDN}}{\partial X_A\partial X_A} = \frac{\partial^2\text{ArDN}}{\partial {R_{AB}}^2}x^2 + \frac{1}{r}\frac{\partial\text{ArDN}}{\partial R_{AB}}(1-x^2) \tag{2.89}$$

$$\frac{\partial^2\text{ArDN}}{\partial Y_A\partial Y_A} = \frac{\partial^2\text{ArDN}}{\partial {R_{AB}}^2}y^2 + \frac{1}{r}\frac{\partial\text{ArDN}}{\partial R_{AB}}(1-y^2) \tag{2.90}$$

$$\frac{\partial^2\text{ArDN}}{\partial Z_A\partial Z_A} = \frac{\partial^2\text{ArDN}}{\partial {R_{AB}}^2}z^2 + \frac{1}{r}\frac{\partial\text{ArDN}}{\partial R_{AB}}(1-z^2) \tag{2.91}$$

$$\frac{\partial^2\text{ArDN}}{\partial X_A\partial Y_A} = \left(\frac{\partial^2\text{ArDN}}{\partial {R_{AB}}^2} - \frac{1}{r}\frac{\partial\text{ArDN}}{\partial R_{AB}}\right)xy \tag{2.92}$$

$$\frac{\partial^2\text{ArDN}}{\partial Y_A\partial Z_A} = \left(\frac{\partial^2\text{ArDN}}{\partial {R_{AB}}^2} - \frac{1}{r}\frac{\partial\text{ArDN}}{\partial R_{AB}}\right)yz \tag{2.93}$$

$$\frac{\partial^2\text{ArDN}}{\partial Z_A\partial X_A} = \left(\frac{\partial^2\text{ArDN}}{\partial {R_{AB}}^2} - \frac{1}{r}\frac{\partial\text{ArDN}}{\partial R_{AB}}\right)zx, \tag{2.94}$$

where (X_A, Y_A, Z_A) is the position of the atom A, and (x, y, z) is the unit vector directing from B to A. Substituting one of the subscript A for B changes the sign of the formulae, and substituting both of the subscripts doesn't change the sign. The rest of 36 elements are given in Eqs. 2.31~2.38, and their Hessians are given as follows:

$$\frac{\partial^2 f_1}{\partial X_A\partial X_A} = \alpha x^4 + (\delta+5\beta)x^2 + \frac{p'-2w}{R_{AB}} \tag{2.95}$$

$$\frac{\partial^2 f_1}{\partial Y_A \partial Y_A} = \alpha x^2 y^2 + \delta y^2 + \beta x^2 + \frac{p'}{R_{AB}} \tag{2.96}$$

$$\frac{\partial^2 f_1}{\partial Z_A \partial Z_A} = \alpha x^2 z^2 + \delta z^2 + \beta x^2 + \frac{p'}{R_{AB}} \tag{2.97}$$

$$\frac{\partial^2 f_1}{\partial X_A \partial Y_A} = \alpha x^3 y + (\delta + 2\beta) xy \tag{2.98}$$

$$\frac{\partial^2 f_1}{\partial X_A \partial Z_A} = \alpha x^3 z + (\delta + 2\beta) xz \tag{2.99}$$

$$\frac{\partial^2 f_1}{\partial Y_A \partial Z_A} = \alpha x^2 yz + \delta yz \tag{2.100}$$

$$\frac{\partial^2 f_2}{\partial X_A \partial X_A} = \alpha x^3 y + 3\beta xy \tag{2.101}$$

$$\frac{\partial^2 f_2}{\partial Y_A \partial Y_A} = \alpha x y^3 + 3\beta xy \tag{2.102}$$

$$\frac{\partial^2 f_2}{\partial Z_A \partial Z_A} = \alpha xyz^2 + \beta xy \tag{2.103}$$

$$\frac{\partial^2 f_2}{\partial X_A \partial Y_A} = \alpha x^2 y^2 + \beta(x^2 + y^2) - \frac{w}{R_{AB}} \tag{2.104}$$

$$\frac{\partial^2 f_2}{\partial X_A \partial Z_A} = \alpha x^2 yz + \beta yz \tag{2.105}$$

$$\frac{\partial^2 f_2}{\partial Y_A \partial Z_A} = \alpha x y^2 z + \beta xz \tag{2.106}$$

$$\frac{\partial^2 f_3}{\partial X_A \partial X_A} = \alpha x^3 z + 3\beta xz \tag{2.107}$$

$$\frac{\partial^2 f_3}{\partial Y_A \partial Y_A} = \alpha x y^2 z + \beta xz \tag{2.108}$$

$$\frac{\partial^2 f_3}{\partial Z_A \partial Z_A} = \alpha x z^3 + 3\beta xz \tag{2.109}$$

$$\frac{\partial^2 f_3}{\partial X_A \partial Y_A} = \alpha x^2 yz + \beta yz \tag{2.110}$$

$$\frac{\partial^2 f_3}{\partial X_A \partial Z_A} = \alpha x^2 z^2 + \beta(x^2 + z^2) - \frac{w}{R_{AB}} \tag{2.111}$$

$$\frac{\partial^2 f_3}{\partial Y_A \partial Z_A} = \alpha xyz^2 + \beta xy \tag{2.112}$$

$$\frac{\partial^2 f_4}{\partial X_A \partial X_A} = \alpha x^2 y^2 + \delta x^2 + \beta y^2 + \frac{p'}{R_{AB}} \tag{2.113}$$

$$\frac{\partial^2 f_4}{\partial Y_A \partial Y_A} = \alpha y^4 + (\delta + 5\beta) y^2 + \frac{p' - 2w}{R_{AB}} \tag{2.114}$$

$$\frac{\partial^2 f_4}{\partial Z_A \partial Z_A} = \alpha y^2 z^2 + \delta z^2 + \beta y^2 + \frac{p'}{R_{AB}} \tag{2.115}$$

$$\frac{\partial^2 f_4}{\partial X_A \partial Y_A} = \alpha x y^3 + (\delta + 2\beta) xy \tag{2.116}$$

$$\frac{\partial^2 f_4}{\partial X_A \partial Z_A} = \alpha x y^2 z + \delta x z \tag{2.117}$$

$$\frac{\partial^2 f_4}{\partial Y_A \partial Z_A} = \alpha y^3 z + (\delta + 2\beta) y z \tag{2.118}$$

$$\frac{\partial^2 f_5}{\partial X_A \partial X_A} = \alpha x^2 y z + \beta y z \tag{2.119}$$

$$\frac{\partial^2 f_5}{\partial Y_A \partial Y_A} = \alpha y^3 z + 3\beta y z \tag{2.120}$$

$$\frac{\partial^2 f_5}{\partial Z_A \partial Z_A} = \alpha y z^3 + 3\beta y z \tag{2.121}$$

$$\frac{\partial^2 f_5}{\partial X_A \partial Y_A} = \alpha x y^2 z + \beta x z \tag{2.122}$$

$$\frac{\partial^2 f_5}{\partial X_A \partial Z_A} = \alpha x y z^2 + \beta x y \tag{2.123}$$

$$\frac{\partial^2 f_5}{\partial Y_A \partial Z_A} = \alpha y^2 z^2 + \beta(y^2 + z^2) - \frac{w}{R_{AB}} \tag{2.124}$$

$$\frac{\partial^2 f_6}{\partial X_A \partial X_A} = \alpha x^2 z^2 + \delta x^2 + \beta z^2 + \frac{p'}{R_{AB}} \tag{2.125}$$

$$\frac{\partial^2 f_6}{\partial Y_A \partial Y_A} = \alpha y^2 z^2 + \delta y^2 + \beta z^2 + \frac{p'}{R_{AB}} \tag{2.126}$$

$$\frac{\partial^2 f_6}{\partial Z_A \partial Z_A} = \alpha z^4 + (\delta + 5\beta) z^2 + \frac{p' - 2w}{R_{AB}} \tag{2.127}$$

$$\frac{\partial^2 f_6}{\partial X_A \partial Y_A} = \alpha x y z^2 + \delta x y \tag{2.128}$$

$$\frac{\partial^2 f_6}{\partial X_A \partial Z_A} = \alpha x z^3 + (\delta + 2\beta) x z \tag{2.129}$$

$$\frac{\partial^2 f_6}{\partial Y_A \partial Z_A} = \alpha y z^3 + (\delta + 2\beta) y z, \tag{2.130}$$

where

$$\alpha = \frac{\partial k}{\partial R_{AB}} - \frac{3k}{R_{AB}} \tag{2.131}$$

$$\beta = \frac{k}{R_A B} \tag{2.132}$$

$$\delta = \frac{\partial^2 p}{\partial {R_{AB}}^2} - \frac{p'}{R_{AB}}, \tag{2.133}$$

while w, p', and k are defined in Eqs. 2.67~2.70. Again, substituting one of the subscript A for B changes the sign of the formulae, and substituting both of the subscripts doesn't change the sign.

2.5 Transition dipole moment

The matrix elements of the electronic dipole operator are evaluated by using the localized point charge model. The electronic dipole operator, $\mathcal{M}$, is divided into the sum of the atomic dipole operators, $\mathcal{M}^A$, as [5]

$$\mathcal{M} = \sum_A \mathcal{M}^A. \tag{2.134}$$

The matrix representation of $\mathcal{M}^A$ becomes diagonal with the basis set $\{\Xi_A^w\}$ under the localized point charge model,

$$\langle \Xi_B^w | \mathcal{M}^A | \Xi_C^v \rangle = \begin{cases} \boldsymbol{R}_A & A = B = C \text{ and } w = v = (x, y, z) \\ 0 & \text{otherwise,} \end{cases} \tag{2.135}$$

where $\boldsymbol{R}_A = (X_A, Y_A, Z_A)$ is the position of atom A relative to the center of mass of the cluster. Therefore, the matrix representation of $\mathcal{M}$ also becomes diagonal as

$$\langle \Xi_A^w | \mathcal{M} | \Xi_B^v \rangle = \begin{cases} \boldsymbol{R}_A & A = B \text{ and } w = v = (x, y, z) \\ 0 & \text{otherwise.} \end{cases} \tag{2.136}$$

2.6 Comparison with ab initio results: Ar_3^+

The potential energy surfaces of Ar_3^+ having $C_{\infty v}$ and C_{2v} symmetries in the electronic ground state are shown in Fig. 2.2. In Fig. 2.2a, two bond lengths, R_1 and R_2, in a linear form ($C_{\infty v}$) are varied independently from $2.0 \sim 4.0$ Å. In Fig. 2.2b, the bond angle and the bond lengths with $R_1 = R_2$ are varied in the ranges of $60 \sim 180°$ and $2.0 \sim 4.0$ Å, respectively. Here, the energy at the dissociation limit, $Ar^+ + 2Ar$, is taken to be 0 eV. These potential surfaces show that Ar_3^+ has a linear symmetric equilibrium geometry with $R_1 = R_2 = 2.60$ Å. Its bond dissociation energy with respect to $Ar_2^+ + Ar$ is 0.25 eV. The comparison of the equilibrium structure and the bond dissociation energy with other results are summarized in Table 2.1. In these studies, the equilibrium structure of Ar_3^+ is symmetric linear, except for the recent *ab initio* result by Bowers [6]. Our DIM result overestimates the bond dissociation energy by *ca.* 0.05 eV as compared with the experimental results. It may result from the underestimation of the repulsive part of the potential energy, as discussed below.

The DIM potential energy surfaces also agree in shape with the *ab initio* surfaces [7]. Figure 2.3 shows the potential curves in $D_{\infty h}$ symmetry as a function of the bond lengths, $R_1 (= R_2)$. Potential curves calculated with an *ab initio* method are also plotted in the figure. The *ab initio* method employed is same as that used in the calculation of the potential curves of Ar_2^+ (p. 10). A good agreement with the *ab initio* results is obtained, especially in the attractive region. In the repulsive region, however, the potential energies are systematically smaller than the *ab initio* results [7]. It might be inherent to the DIM method because of the neglect of the overlap integrals in the model.

Figure 2.4 shows the comparison of the oscillator strength curves of the DIM (solid) and our *ab initio* CI (broken) calculations [7]. The curves in Fig. 2.4a are those against the antisymmetric stretching mode, $R_1 - R_2$, at a linear conformer ($C_{\infty v}$) with a fixed $R_1 + R_2 = 5.30$ Å. The curves in Fig. 2.4b are against the bending mode at an equilateral triangle conformer (C_{2v}) with a fixed $R_1 (= R_2) = 2.65$ Å. The oscillator strength curves less than 0.01 at any $R_1 - R_2$ and θ values are not shown in the figure. The agreement of two calculations is remarkable, particularly for the most prominent transition (to $2^2\Sigma^+$ in $C_{\infty v}$ and to 2^2A_1 in C_{2v}) which is the only allowed transition at the equilibrium structure ($D_{\infty h}$). The DIM method tends to overestimate the "forbidden" transition moments at structures deviated far from the equilibrium structure. Thus, no serious errors in evaluating the photoabsorption cross sections are expected except for the high vibrational states. The point charge model can account for only the excitation of the charge-transfer (or, more properly in the present case, hole-transfer) type. The agreement of the DIM with the *ab initio* CI shows that all of these excited states are of the hole-transfer type. Though the intra-atomic excitations are included in the *ab initio* CI calculations, they have no contribution to the transition moments. Table 2.2 summarizes a comparison of the oscillator strength and excitation energy of the $1^2\Sigma_g^+ \leftarrow 1^2\Sigma_u^+$ transition at the equilibrium structure. All the calculated oscillator strengths agree with each other except for Gadea and Amarouche's. The calculated excitation energies agree well with the energy at the peak of the observed spectrum, 2.38 eV (520 nm) [8–10].

A calculation for Ar_3^+ including a spin-orbit interaction is also performed within the atoms-in-molecules (AIM) approximation [11]. The equilibrium structure is not influenced by introduction of the spin-orbit interaction into the calculation. The shapes of the potential energy surfaces and the oscillator strengths near the equilibrium structure are not affected either. Accordingly, the spin-orbit interaction is ignored in the following calculation.

Bibliography

[1] J. C. Tully, in *Semiempirical Methods of Electronic Structure Calculation*, edited by G. A. Segal (Plenum, New York, 1977); J. C. Tully, Adv. Chem. Phys. **42**, 63 (1980); P. J. Kuntz, in *Atom-molecule collision theory*, edited by R. B. Bernstein (Plenum, New York, 1979).

[2] P. J. Kuntz and J. Valldorf, Z. Phys. D–Atoms, Molecules and Clusters **8**, 195 (1988).

[3] J. S. Cohen and B. Schneider, J. Chem. Phys. **61**, 3230 (1974).

[4] R. O. Watts and I. J. McGee, *Liquid state chemical physics* (Wiley, New York, 1976).

[5] J. C. Tully, J. Chem. Phys. **64**, 3182 (1976).

[6] M. T. Bowers, W. E. Palke, K. Robins, C. Roehl, and S. Walsh, Chem. Phys. Lett. **180**, 235 (1991).

[7] T. Ikegami, T. Kondow, and S. Iwata, unpublished data.

[8] N. E. Levinger, D. Ray, K. K. Murray, A. S. Mullin, C. P. Schulz, and W. C. Lineberger, J. Chem. Phys. **89**, 71 (1988).

[9] Z. Y. Chen, C. R. Albertoni, M. Hasegawa, R. Kuhn, and A. W. Castleman Jr., J. Chem. Phys. **91**, 4019 (1989).

[10] T. F. Magnera and J. Michl, Chem. Phys. Lett. **192**, 99 (1992).

[11] J. S. Choen and B. Schneider, J. Chem. Phys. **61**, 3230 (1974).

[12] H.-U. Böhmer, and S. D. Peyerimhoff, Z. Phys. D–Atoms, Molecules and Clusters **3**, 195 (1986).

[13] W. R. Wadt, Appl. Phys. Lett. **38**, 1030 (1981).

[14] F. X. Gadea and M. Amarouche, Chem. Phys. **140**, 385 (1990).

[15] I. Last and T. F. George, J. Chem. Phys. **93**, 8925 (1990).

[16] R. G. Keesee, and A. W. Castleman, Jr., J. Phys. Chem. Ref. Data **15**, 1011 (1986).

[17] K. Hiraoka and T. Mori, J. Chem. Phys. **92**, 4408 (1990).

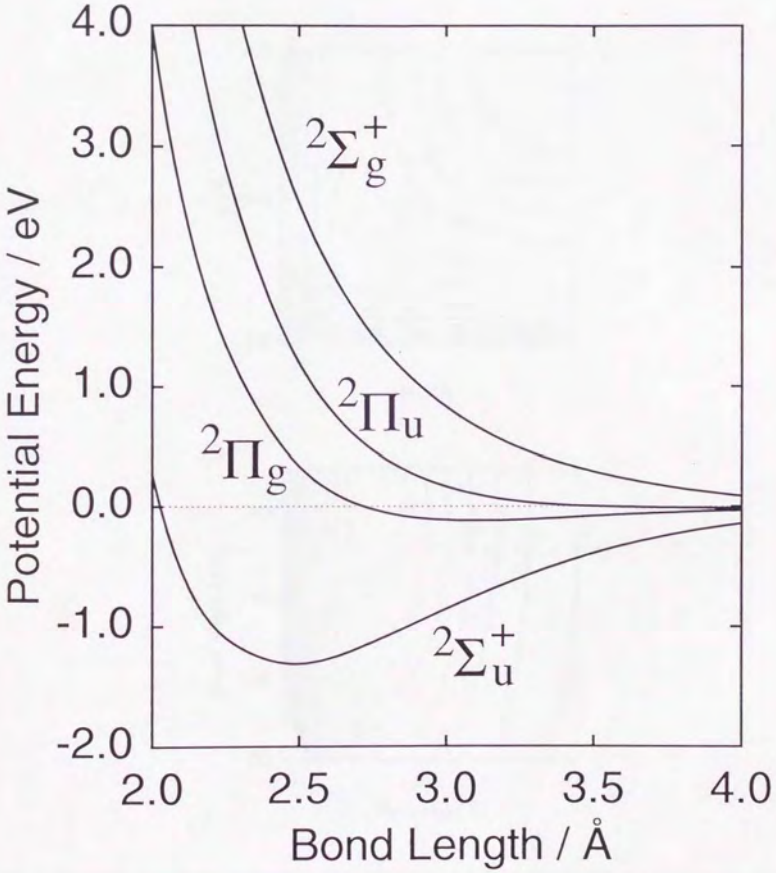

Figure 2.1: Four potential curves calculated by an *ab initio* method.

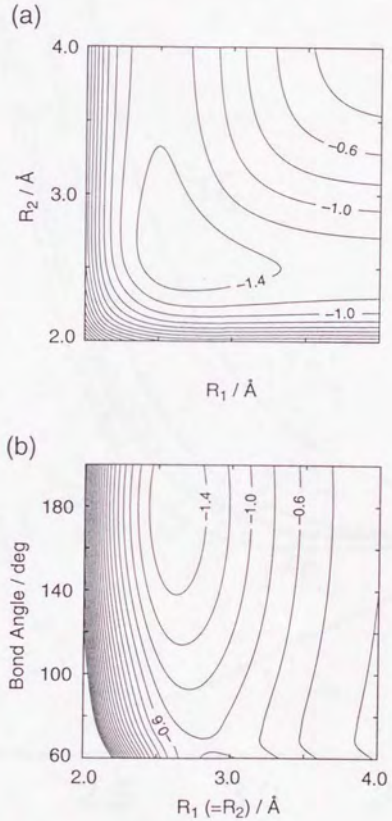

Figure 2.2: The contour maps of the potential energy surfaces of Ar_3^+ calculated with the DIM model. The unit of the energy shown in the figure is eV. The energy is measured from Ar + Ar + Ar^+. (a) $C_{\infty v}$ symmetry, (b) C_{2v} symmetry.

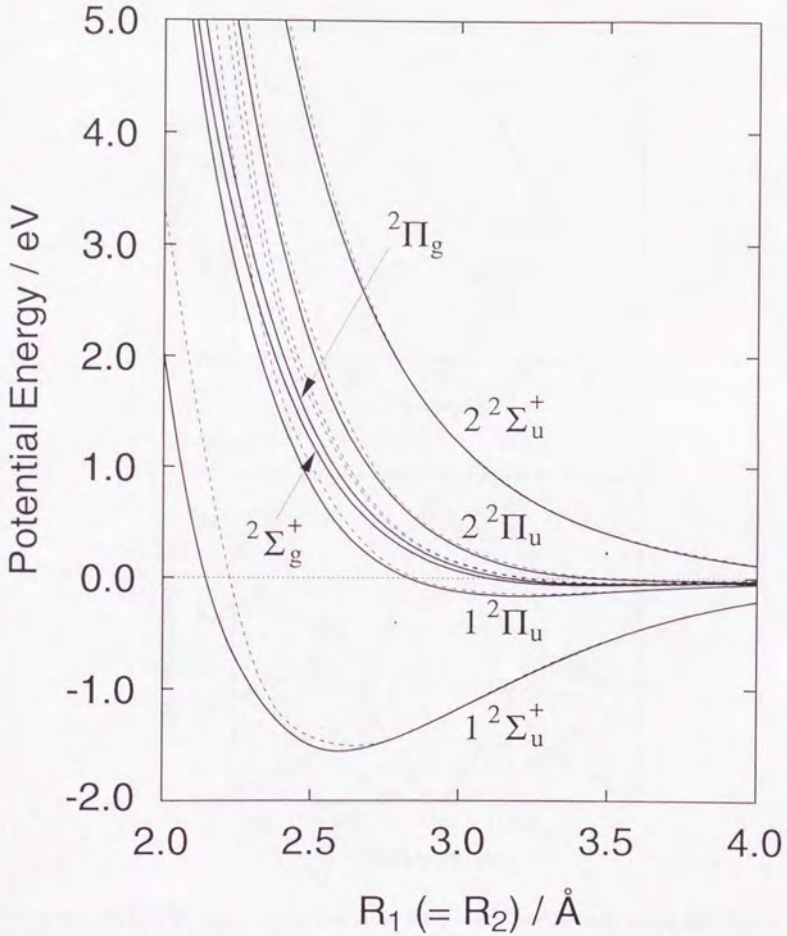

Figure 2.3: The potential energy curves of Ar_3^+ in the linear symmetric form ($D_{\infty h}$). All of 3p valence hole states are shown. The DIM curves are plotted in solid lines, while *ab initio* curves are plotted in thin broken lines.

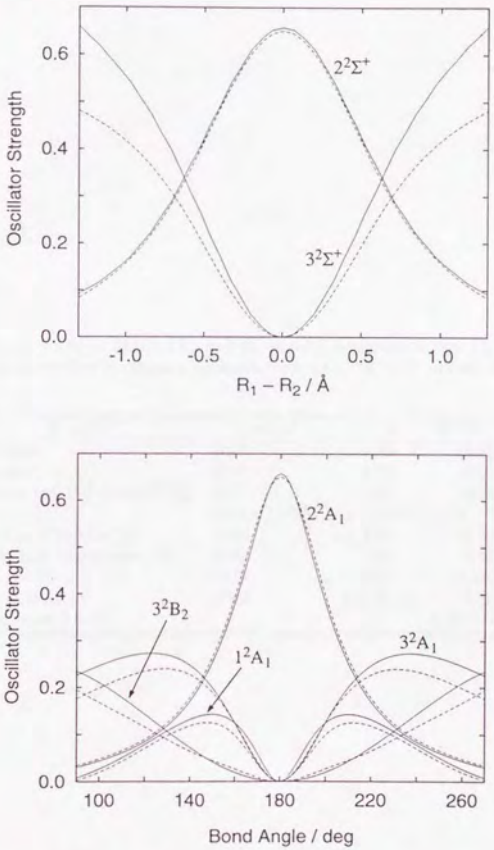

Figure 2.4: The oscillator strengths as a function of the antisymmetric and bending coordinates. The *ab initio* values [7] are shown in broken lines. (a) The antisymmetric vibrational mode, $R_1 + R_2 = 5.30$ Å. (b) The bending mode, $R_1 = R_2 = 2.65$ Å.

Table 2.1: A comparison of the bond length (R) and the bond dissociation energy (BDE) of Ar_3^+ with other works. All the equilibrium structures are linear symmetric, except for the linear asymmetric structure by Bowers *et al.*

Authors	method	R / Å	BDE / eV
This work	DIM	2.60	0.25
Ikegami et al. [7]	POL-CI	2.65	0.20
Böhmer and Peyerimhoff [12]	MRD-CI	2.62	0.16
Wadt [13]	POL-CI/DIM	– / 2.67	0.18 / 0.13
Kuntz and Valldorf [2]	DIM	2.61	0.19
Gadea and Amarouche [14]	DIM	2.59	0.17
Last and George [15]	DIIS	2.59	0.203
Bowers *et al.* [6]	MP2	2.47/2.73	0.15
Experiment [16,17]		–	$0.18 \sim 0.22$

Table 2.2: A comparison with other works: The oscillator strength (f) and excitation energy (ΔE) of $1^2\Sigma_g^+ \rightarrow 1^2\Sigma_u^+$ transition at the equilibrium structure of Ar_3^+.

Authors	method	f	ΔE / eV
This work	DIM	0.69	2.36
Ikegami et al. [7]	POL-CI	0.65	2.36
Wadt [13]	POL-CI	0.61	2.36
Gadea and Amarouche [14]	DIM	1.6	2.34
Last and George [15]	DIIS	0.66	2.26

Chapter 3

Static properties

Abstract

The most stable structures of Ar_n^+, $n = 3 \sim 27$, are determined with the analytical gradient method for the diatomics-in-molecules Hamiltonian. The charge is found to be localized on the central three atoms, which form the trimeric ion core. The first solvation shell evolves around the ion core and is completed at $n = 25$. The distribution of the oscillator strength is evaluated at the optimized structures. The calculation shows that the photoabsorption band is in the visible region, which originates from the $^2\Sigma_g^+ - 1^2\Sigma_u^+$ transition of the Ar_3^+ ion core, and is red-shifted with the increase of the cluster size, reproducing the experimental results. The red-shift is explained in terms of the solvated ion core model, in which the excited state of the ion core interacts strongly with the surrounding solvent atoms.

3.1 Introduction

Last few years, geometric and electronic structures of argon cluster cation, Ar_n^+, have been intensely studied both experimentally and theoretically [1–16]. Most of the experimental results have indicated that the large cluster ion consists of a small ionic entity surrounded by neutral Ar atoms. In a number of theoretical calculations, the ionic entity was assumed to be a dimer ion [1–4], because of its large binding energy (1.33 eV) [17]. In the Diatomics-in-Molecules (DIM) calculations, however, Kuntz and Valldorf have shown that a trimer ion, Ar_3^+, is the ion core in the cluster ions up to $n \simeq 13$ [5]. They have also found that the positive charge starts to delocalize on the 4th atom as n increases from 14 to 19. Similarly, Last and George have predicted the presence of the trimeric ion core in Ar_n^+, $n = 3 \sim 6$, by using the diatomics-in-ionic-systems (DIIS) method [6] that introduces a polarization effect into the DIM method. Böhmer and Peyerimhoff have performed Monte-Carlo (MC) simulation on Ar_n^+, $n = 3 \sim 27$ [7], assuming both dimeric and trimeric ion cores. In comparison with the observed magic numbers [8,9], they have concluded that a trimer ion is more likely the ion core of Ar_n^+ than a dimer ion.

Experimentally, Levinger *et al.* have measured photoabsorption spectra of Ar_n^+, $n = 3 \sim 40$ [10]. They observed a broad and intense band peaking near 520 nm in the range of $n = 3 \sim 15$. For $n = 15 \sim 20$, this band peak shifts smoothly from 520 nm to 600 nm, and does not change any more for $n > 20$. This characteristic shift might be explained with the finding by Kuntz and Valldorf that the ion core in the cluster changes from Ar_3^+ to Ar_4^+ as n increases from 15 to 20, though they did not examine the change of the photoabsorption spectra with the cluster size. Haberland et al. have measured the absorption spectra more extensively up to $n = 80$ [11], and have found another red shift between $n = 6$ and 9. Also the n dependence of the photoionization threshold energies of Ar_n has been experimentally studied in detail [12,13]. The ionization energies of Ar_n thus obtained are well described in terms of the trimeric ion core in a small n region in comparison with MC calculations [7]. The angular and the kinetic energy distributions of both ionic [15] and neutral [16] photofragments of Ar_n^+ have given a further support of the trimeric ion core model: The bimodal velocity distributions of neutral photofragments, which is characteristic of Ar_3^+, are observed up to $n \simeq 13$ [16]. The presence of the trimeric ion core is also observed in a single crystal of argon, which is regarded as the large cluster-size limit. The 3p valence hole in crystal is self-trapped among three Ar atoms [18,19].

These theoretical and experimental works indicate that the ion core, Ar_3^+, is formed in the size range of $n < 20$, but it is still ambiguous in the larger n region whether the ion core of Ar_3^+ persists or not. In order to solve this problem, the geometry of the cluster ions ($n = 3 \sim 27$) is fully optimized by using the DIM model introduced by Kuntz and Valldorf. The oscillator strength distribution from the electronic ground state is also calculated, and the spectral shift observed at $n = 15 \sim 20$ is successfully reproduced in the calculation. This shift is analyzed in terms of the solvated ion core model, in which the optically-allowed excited electronic state

of the ion core interacts with the hole states of solvent atoms.

3.2 Calculation

The construction of the DIM Hamiltonian and the analytic gradient of the potential surface are fully documented in sections 2.1 and 2.2 (pp. 7, 11). Here, the algorithm used for the geometrical optimization of the clusters are described. In finding the most stable structures on the potential surface of the electronic ground state, the steepest descent method is employed using the analytic gradient of the surface. Starting from an arbitrary initial structure, all the atoms are moved in the direction of the gradient vector. The magnitude of the displacement is tweaked in every displacement such that the potential energy at a new configuration becomes lower than that at the previous one. The optimization procedure is continued until the absolute value of the gradient become less than 10^{-5} eVÅ^{-1}.

The most stable structure of Ar_3^+ is carefully determined from extensive calculations of the potential energy surface. The initial geometry for Ar_n^+, $n = 4 \sim 22$, is generated by adding an Ar atom randomly to the most stable structure of the cluster Ar_{n-1}^+. Since many local minima are expected to exist, 30 to 100 initial geometries are examined. For $n > 22$, several initial structures were chosen by inspection. The optimized structures are confirmed to have no imaginary frequency by diagonalizing the Hessian matrix, so that they are not located at the stationary points but at the true local minima.

3.3 Results and Discussion

3.3.1 Bonding energies and magic numbers of Ar_n^+ ($n = 4 \sim 27$)

The most stable structures determined for Ar_n^+ are shown in Fig. 3.1. The blackness of the shade on each atom is roughly proportional to the hole density on the atom in the ground state. The scale of the density is given at the bottom of the figure. For example, the charge density is 0.5 on the central atom and 0.25 on each side atom in Ar_3^+. In all the examined cluster ions, the trimer cation Ar_3^+ forms the ion core inside the cluster, and the surrounding atoms are left nearly neutral in the ground electronic state.

The stabilization energy of the most stable structures against the corresponding dissociation limits,

$$E_n = E(Ar^+) + (n-1)E(Ar) - E(Ar_n^+), \tag{3.1}$$

is summarized in Table 3.1. The bond dissociation energies, $\Delta E_n = E_{n-1} - E_n$, are between 0.06 and 0.08 eV, which are in good agreement with experimental values [20]. The general trend of the n dependence of the dissociation energy is consistent with the Monte-Carlo calculations at 10 K based on the trimeric ion core picture [7].

The relative binding energy, $\Delta E_n/\Delta E_{n+1}$, is plotted as a function of the cluster size in Fig. 3.2. The pronounced stability at a certain cluster size n, which is called "magic numbers", is found as shown if Fig. 3.2; our theoretical magic numbers are 13, 16, 19, 22 and 25. On the other hand, the experimentally obtained magic numbers are 13, 23, 26, ... by Harris *et al.* [9], and 14, 16, 19, 21, 23 and 27 by Ding and Hesslich [8]. Very recently, Wei, Shi and Castleman (WSC) have determined the n dependence of the relative binding energy for Xe_n^+ experimentally [21], which is also shown in Fig. 3.2; their magic numbers are 13, 16, 19, 23, 25 and 29. It should be noted that the experimental magic numbers of Xe_n^+ agree with ours except for $n = 22$. This agreement is reasonable because the WSC's experiment determines the magic numbers from the relative binding energies, $\Delta E_n/\Delta E_{n+1}$ [21], for the first time. The magic numbers have been determined so far from the intensity anomalies in the mass spectra. In the latter type of experiments, there are always possibilities that the ion intensity is determined not only by the stability of the cluster ion, but also by other factors, such as the abundance of the parent neutral clusters and the photoionization efficiency. Note that the remarkable instability of Ar_{20}^+ observed in the mass spectrum [8–10] can not be seen in both our and WSC's plots in Fig. 3.2. This instability may be related to the dynamics in the formation of the cluster ion.

3.3.2 Structural evolution of Ar_n^+

As shown in Fig. 3.1, the neutral atoms surround an axis of the Ar_3^+ ion core, aggregating with each other for the cluster size from $n = 4$ to 13. At Ar_{13}^+, two 5-membered rings are completed in a staggered conformation around the ion core. Two rings grow simultaneously, that is, a single 5-membered ring does not appear at $n = 8$. The neutral atoms are attached at one end of the ion core in $Ar_{14}^+ \sim Ar_{19}^+$, and a pentagonally pyramidal cap is completed in Ar_{19}^+. This cap contains a 5-membered ring, but again it is not formed first. The apex atom of the pyramidal cap, which first appears in Ar_{17}^+, is necessary to stabilize the ring. A neutral atom starts to attach on the other end of the ion core as the cluster grows from $Ar_{20}^+ \sim Ar_{25}^+$. Six neutral atoms form another cap, closing the first solvation shell composed of 22 atoms in Ar_{25}^+.

To see the underlying rules in the evolution of the cluster, and to elucidate the determining factors in the stabilization of the cluster, the structural characteristics in each of Ar_n^+ are discussed below in more details and compared with previous works. The most stable structure of Ar_4^+ is a distorted T-shape, consisting of an Ar_3^+ ion core and a loosely bound neutral Ar atom. The neutral atom is bound at the side between the center and the end atoms of the Ar_3^+ ion core. It is located at 3.32 Å away from the axis of the ion core, and shifts by 1.01 Å from the central atom to the side one. The structure of the ion core is almost same as that of Ar_3^+. A linear structure with internuclear distances of 2.65, 2.57, and 3.15 Å is also found to be a local minimum, and the energy is higher only by 0.003 eV than the distorted T-shape. This result agrees with Last and George's [6]. On the other hand, Kuntz and Valldorf, and Böhmer and Peyerimhoff have calculated

that the linear isomer is more stable than the distorted T-shaped isomer [5, 7]. In all of these calculations, including ours, the calculated energy difference is too small to determine which isomer is more stable. The calculated photoabsorption spectrum of both isomers (see section 3.3.3) shows that the excitation energy of the T-shaped isomer is close to those of the trimer ion, while that of the linear isomer is shifted to lower energy (as that of the large cluster ions). Experimental measurements show that the spectrum of Ar_4^+ is very similar to that of Ar_3^+ [10, 11]. Therefore, it is more probable that the most of the tetramer ions are produced in a distorted T-shape under an ordinary experimental condition. Why is the distorted T-shape more stable than the others such as the exact T-shape? The interaction between the ion core and a neutral atom is essentially the polarization force, so that the distribution of the positive charge (hole) is important. The ground state of the trimer ion is $^2\Sigma_u^+$, and the hole is located on the σ_u 3p orbitals on each atom. The resident probability is twice as large on the center atom as on the end atoms. The distorted T-shape is more stable because the neutral atom can be attracted by both the center atom and one of the end atoms of the trimeric ion core.

The most stable structure of Ar_5^+ is the one that a neutral dimer is attached perpendicularly to the axis of Ar_3^+ ion core. Similarly to a neutral Ar atom in Ar_4^+, the dimer is located between the center atom and the one of the end atoms of the Ar_3^+ ion core. The bond distance of the neutral dimer is 3.76 Å.

In the present approximation, the interaction energy between the induced dipole moments of two atoms is not taken into account. By using the distributed point charge model and the polarizability of an Ar atom, the interaction energy is estimated to be repulsive by 0.001 eV, which is too small to influence the structure of the cluster. In fact, our structure is in good agreement with that of Last and George, whose calculations include the polarization terms.

The ion core Ar_3^+ becomes gradually bent as the cluster size increases up to $n = 11$, because the neutral atoms are added unevenly to the core. For instance, the bond angle of $(Ar–Ar–Ar)^+$ in Ar_{11}^+ ($[Ar_3]^+Ar_8$) is 172.4°. Meanwhile, the bond lengths of the ion core are still nearly symmetric and elongated only by 0.3 % in comparison with those of Ar_3^+.

The most stable structure of Ar_{13}^+ is an icosahedron that is slightly compressed along the molecular axis of the Ar_3^+ ion core, and belongs to the D_{5d} point group. The structure of the ion core becomes again almost same as Ar_3^+. The neutral atoms are located at 3.32 Å apart from the axis, which is nearly equal to the distance between the neutral atom and the Ar_3^+ core in Ar_4^+. The shortest distance between two neutral atoms is 3.66 Å, which is shorter by 2.7 % than the bond length of the van der Waals dimer, Ar_2.

Once the cap starts to grow at one end of the icosahedron in the size range from $n = 14$ to 19, the ion core distorts to an asymmetric form ($C_{\infty v}$), and the charge distribution within the ion core becomes asymmetric. In Ar_{16}^+ ($[Ar_3]^+Ar_{13}$), for example, the two Ar-Ar distances in the core are 2.55 and 2.71 Å with the Ar-Ar distance of the capped site shorter than the other, and the charge density on the capped end is twice as large as that on the open end. The similar charge disparity is found when the trimer Ar_3^+ is distorted from the symmetric

configuration.

In Ar_{19}^+, four Ar atoms are lined with the spacings 2.66, 2.58 and 3.31 Å, and are surrounded by three 5-membered rings. Namely, Ar_{19}^+ has a five-fold symmetry. The charge is still localized within the three Ar atoms, as is also evident from the geometry of the axial four atoms. The distances between the axis and the surrounding neutral atoms range from 3.23 to 3.37 Å. An isomer of Ar_{19}^+ having two triangular Ar_3 caps at both ends of the ion core of Ar_{13}^+ is also located at a local minimum, but the energy is higher by 0.046 eV than that of the most stable structure discussed above.

Two structures of Ar_{20}^+ are shown in Fig. 3.1. In the most stable structure, denoted by (20), an additional atom is attached to Ar_{19}^+ in the second solvation shell. The additional atom is separated by 5.69 Å from the axis of the ion core. In the other meta-stable structure, denoted by (20'), the atom starts to form a new cap at the other end of the ion core. The energy of (20') is higher only by 0.005 eV than that of the structure (20). The relative binding energy calculated with the meta-stable isomer is plotted by boxes (□) in Fig. 3.2. When another atom is added to form Ar_{21}^+, the most stable structure has a neutral dimer at the uncapped end of the ion core. In fact, from this structure the isomer (20') is deduced.

In Ar_{25}^+, the five-fold axis and the center of symmetry appear again as in the case of Ar_{13}^+ with a very stable packing of neutral atoms, which has been also observed by Böhmer and Peyerimhoff [7]. The structure of Ar_{25}^+ consists of a linear symmetric pentamer with the spacings of 3.53, 2.62, 2.62, and 3.53 Å and four 5-membered rings in staggered conformations. The atoms of the inner rings are separated from the axis by 3.33 Å, whereas the atoms of the outer rings are separated by 3.22 Å. The bond lengths of the ion core are symmetrically elongated by 0.8 % from that of Ar_3^+.

Böhmer and Peyerimhoff have determined the structures of $Ar_{24}^+ \sim Ar_{27}^+$ with the second solvation shell [7]. We also examined the similar structures for Ar_{23}^+ and Ar_{24}^+, but found that they are at local minima. However, we cannot exclude the possibility that the more distorted structure with the second shell (not examined in the present work) may be the most stable. The second solvation shell appears again in Ar_{26}^+ and Ar_{27}^+. The additional neutral atoms are located at the almost same site as in the most stable structure of Ar_{20}^+, separated by 5.70 Å from the axis of the ion core.

3.3.3 Spectral properties of Ar_n^+

The distribution of the oscillator strength for the transition from the electronic ground state is calculated for all the clusters at the optimized geometry. Figure 3.3 shows the size dependence of the oscillator strength distribution. The lengths of the horizontal bars in the figure are proportional to the calculated oscillator strengths. Up to $n = 10$, the most intense band shifts to a higher energy with the cluster size, while a few intense bands start to appear in a lower energy from $n = 11$. Hereafter the former and the latter are called

the H-branch and the L-branch, respectively. In some sizes, the L-branch splits into two or three bands, and gradually converges to 2.0 eV with the increase of the cluster size. An average excitation energy weighted by the oscillator strengths, $\Delta\bar{E}_n$, is defined as

$$\Delta\bar{E}_n = \frac{\sum_i f_{i0}(E_n^i - E_n^0)}{\sum_i f_{i0}}, \tag{3.2}$$

where E_n^i is the energy of the i-th excited state and f_{i0} is the oscillator strength of the transition between the ground and the i-th excited state. The script 0 denotes the ground state. The center of the absorption spectrum in wavelength, $\bar{\lambda}_n$, is defined as $\bar{\lambda}_n = hc/\Delta\bar{E}_n$, and its size dependence is plotted in Fig. 3.4. As shown in the figure, $\bar{\lambda}_n$ increases abruptly from 520 to 580 nm at $n = 11$. The experiment of Levinger *et al.* [10] have given this abrupt red shift. However, the present calculations do not predict another red shift observed by Haberland *et al.* in the size range from $n = 6$ to 9 [11]. This disagreement may originate from the averaging procedure (Eq. 3.2), because a trace of the L-branch is found for $n \geq 6$ in Fig. 3.3. It is also likely that the L-branch is strongly enhanced by the vibrational excitation. The effects of the vibrational excitation on the spectra will be discussed in Chapter 4.

3.3.4 Solvated ion core model

As mentioned above, the oscillator strength distribution consists of H- and L-branches. A major branch switches from H- to L-branch in the vicinity of $n = 10$. In this subsection, we scrutinize the character of two branches and the underlying physics in the switching of the main branch. Figure 3.5 shows the charge (hole) distribution of a representative final state for each branch in Ar_5^+, Ar_{10}^+, and Ar_{16}^+. For comparison, a charge distribution of $1^2\Sigma_g^+$ state of Ar_3^+, which is the final state of the visible absorption band [22–25], is also shown. In Ar_5^+, the oscillator strength to the excited state in the H-branch (the upper part of Fig. 3.5b) is larger than that in the L-branch, whereas in Ar_{16}^+, that in the L-branch (the lower part of Fig. 3.5d) is larger. In Ar_{10}^+, the final states of both branches have the nearly equal oscillator strengths. It is concluded by comparing the charge distributions of (a), the upper part of (b) and the lower part of (d) in Fig. 3.5 that the core part of the optically allowed state has the similar charge distribution to that of the $1^2\Sigma_g^+$ state of the trimer ion. The following two important characteristics are derived from this observation: (1) the most intense transition is characterized as the intra ion core excitation, and (2) as the cluster size increases, this excited state of the ion core is first shifted to a higher energy, is strongly mixed with the electronic states having the positive hole in the surrounding (solvent) atoms at around $n = 10$, and finally is moved to the L-branch.

To analyze these characteristic behaviors, the electronic configuration space, $\{\ \Xi_i;\ 1 \leq i \leq 3n\ \}$, is divided into two subspaces; a core subspace and a surrounding subspace. The core subspace, $\mathcal{P}_C$, is spanned by the core states ($\{\ \Xi_\alpha,\ 1 \leq \alpha \leq 9\ \}$), where the positive hole is confined in the central three atoms forming the ion core. The rest of the space, $\mathcal{P}_S$, is spanned by the surrounding states ($\{\ \Xi_\beta,\ 10 \leq \beta \leq 3n\ \}$), where the hole

is delocalized among the solvent atoms. Within each subspace, the Hamiltonian matrix is diagonalized; the eigenstates of each Hamiltonian are the C-states $\{ \Phi_i^C,\ 0 \leq i \leq 8 \}$ and the S-states $\{ \Phi_j^S,\ 1 \leq j \leq 3n-9 \}$, respectively. The energies of the C- and S-states relative to the true ground state of each cluster ion (see Table 3.1) are shown in Figs. 3.6a and b. Figure 3.6a demonstrates that the C-states remain the characters of the electronic states of Ar_3^+. Note that the electrostatic interaction between the ion core and the neutral solvent atoms is included in the sub-Hamiltonian matrix. The distribution of the S-states in Fig. 3.6b is irregularly broadened with the cluster size; the irregularity is a reflection of the "solvent" structure. The true eigenstates of the clusters are represented by a linear combination of C- and S-states. They are obtained by diagonalizing the transformed Hamiltonian matrix, which has only non-zero off-diagonal elements between the C- and the S-states.

The true electronic ground state consists chiefly of the *ground* C-state (Φ_0^C) alone, because Φ_0^C is energetically isolated from the other states. Similarly, the true highest excited state is mostly the 8th *excited* C-state (Φ_8^C). The rest of the excited states are the mixtures of the C- and S-states, and thus the positive charge is delocalized all over the cluster ion. The energy levels of the *excited* C-states, especially Φ_3^C, Φ_4^C, and Φ_5^C, are overlapped with those of the S-states, resulting in the strong interaction between the C- and the S-states.

It is the third *excited* C-state, Φ_3^C, that corresponds to the optically allowed $^2\Sigma_g^+$ state of an isolated Ar_3^+. The energy of Φ_3^C does not change with the cluster size as shown in Fig. 3.6a. The oscillator strength distribution among the true excited states of the cluster ion may be correlated to the distribution of Φ_3^C in the wavefunctions. That is, the change of the oscillator strength distribution in Figs. 3.3 and 3.4 with the cluster size n results from the change of the mixing of Φ_3^C to the true excited states. We analyze how the mixing is changed with n, particularly around $n = 10$. To do so, we extract an effective solvent state, Φ_{eff}^S, from the S-states, such that the interaction between Φ_{eff}^S and Φ_3^C is maximized. First, the S-states, $\{ \Phi_j^S \}$, are unitary-transformed to $\{ \Phi_j^{S\prime} \}$, such that the matrix elements $\langle \Phi_3^C | \mathcal{H} | \Phi_j^{S\prime} \rangle$ $(j = 2, 3, \cdots, 3n-9)$ are zero except for $j = 1$. Unfortunately, the resulting $\Phi_1^{S\prime}$ interacts also strongly with the other C-states: the interaction energy with either Φ_7^C or Φ_8^C is larger than that with Φ_3^C in the size range from $n = 4$ to 10. To construct more appropriate Φ_{eff}^S, the mixing of the C-states other than Φ_3^C with $\Phi_1^{S\prime}$ has to be partly introduced. Those C-states, except for Φ_3^C, that have more than 0.1 eV interaction energy with $\Phi_1^{S\prime}$, i. e., $|\langle \Phi_i^C | \mathcal{H} | \Phi_1^{S\prime} \rangle| > 0.1$ eV $(i \neq 3)$, are included in the mixing. The effective surrounding state, Φ_{eff}^S, is thus determined by diagonalizing a small Hamiltonian matrix; Φ_{eff}^S is easily assigned among the eigenstates by seeing the coefficient of $\Phi_1^{S\prime}$.

Once Φ_{eff}^S is determined, the problem is reduced to a two-level problem between Φ_3^C and Φ_{eff}^S. The Hamiltonian matrix elements are plotted as a function of the cluster size, n, in Fig. 3.7; the diagonal elements (E_3^C and E_{eff}^S) in (a) and the off-diagonal element $H_{fig:CSlevel} = \langle \Phi_3^C | \mathcal{H} | \Phi_{eff}^S \rangle$ in (b). The energies of two adiabatic states Ψ_H and Ψ_L, obtained by diagonalizing 2 by 2 matrix, are also plotted in Fig. 3.7a. The energy levels of the core state and the surrounding state, E_3^C and E_{eff}^S, cross at $n = 10$. For $n < 10$, E_{eff}^S is lower than

E_3^C, and thus the main component of Ψ_H is the optically-allowed Φ_3^C state. On the other hand, for $n > 10$, E_{eff}^S becomes higher than E_3^C, and the Φ_3^C state starts to contribute substantially to Ψ_L. Another interesting finding is that off-diagonal element between Φ_3^C and Φ_{eff}^S suddenly increases at $n = 15$ and 21, which may result in the appreciable spectral shift found in Fig. 3.4.

To examine the appropriateness of the two-level model, the averaged excitation energy of Ψ_H and Ψ_L weighted by the oscillator strength (a dotted line) is compared with $\Delta\bar{E}_n$ in Fig. 3.4. The two plots are well correlated to each other, implying that the present simplified model works well in interpreting the observed spectral shift with the cluster size.

The abrupt increase of the off-diagonal matrix element at $n = 15$ and 21 indicates that the atoms attached to the ends of the ion core play an important role in the core-solvent interaction and the spectral shift. The hole orbitals, which is the molecular orbital containing the positive hole, are shown schematically in Fig. 3.8 for Φ_3^C (a) and Φ_{eff}^S (b) of Ar_{15}^+. The hole orbital of Φ_3^C (Fig. 3.8a) is extended along the axis of the ion core. In the hole orbital of Φ_{eff}^S (Fig. 3.8b), the atoms attached to the end of the ion core have large coefficients to interact strongly with Φ_3^C. This interaction explains the jump of the off-diagonal element at $n = 15$ and 21. Note that the linear Ar_4^+ mentioned in section 3.3.2 shows the similar spectral shift as the larger clusters. The other interesting feature seen in Fig. 3.8b is that the p orbitals on the atoms in the rings are directed toward the ion core axis with the in-phase manner. It is expected that the interaction between the ring and the ion core increases gradually as the rings are constructed in the size range from $n = 4$ to 13, as seen in Fig. 3.7b. These in-phase p orbitals interact with themselves, which is responsible to the systematic increase of the diagonal element of Φ_{eff}^S. As shown in the end-view of the Fig. 3.8b, these orbitals have the bonding character among the intra-ring atoms. A hole in the bonding orbital destabilizes the cluster ion, resulting in the increase of E_{eff}^S.

The present model calculation suggests that the main character of the photoexcited states of Ar_n^+ is always the optically allowed state of Ar_3^+, so that the photodissociation process is expected to be similar to Ar_3^+. Indeed, up to Ar_6^+, the velocity distribution of Ar^+ fragment ion from the photoexcited Ar_n^+ resembles to that of Ar_3^+ [15]. The Ar^+ fragment is unable to be detected for the cluster ions larger than Ar_7^+, probably because the exiting Ar^+ interacts strongly with the residual atoms of the cluster and the charge is transferred back to the residual. On the other hand, the fast neutral fragments, which are characteristic of the Ar_3^+ photodissociation [16], are observed up to $n \simeq 13$, as an interaction with the residuals is weak. Ejection of the fast neutral fragments is not observed for $n \geq 14$ [16]. These results indicate that the Ar atoms attached to the ends of the ion core also affect the photodissociation process of the ion core. The photodissociation process itself will be discussed in more detail at Chapter 5.

3.3.5 Properties of the adiabatic states

The inner products between the true eigenstates of Ar_n^+ and each C-state are evaluated to reveal how the core states $\{ \Phi_i^C, 0 \leq i \leq 8 \}$ are distributed in the wavefunctions of Ar_n^+. The absolute values of the inner products,

$$|\langle \Phi_i^C | \Psi \rangle| \qquad \text{for } i = 0, 3, \text{ and } 8 \tag{3.3}$$

$$(|\langle \Phi_i^C | \Psi \rangle|^2 + |\langle \Phi_{i+1}^C | \Psi \rangle|^2)^{1/2} \qquad \text{for } i = 1, 4, \text{ and } 6, \tag{3.4}$$

are shown in Fig. 3.9. These C-states correspond to $1^2\Sigma_u^+$, $1^2\Sigma_g^+$, and $2^2\Sigma_u^+$ states of Ar_3^+ for $i = 0$, 3, and 8, and $1^2\Pi_u$, $1^2\Pi_g$, and $2^2\Pi_u$ for $i = 1$, 4, and 6, respectively. The C-states corresponding to Π states of Ar_3^+, such as Φ_1^C and Φ_2^C, are nearly degenerated.

As shown in Fig. 3.9c, the inner product with Φ_3^C ($1^2\Sigma_g^+$ of Ar_3^+) is split in higher and lower components in energy; the way of the splitting is consistent with the above model calculation. The $1^2\Pi_g$ core state shows similar splitting (Fig. 3.9d), suggesting a strong interaction between the S-states and $1^2\Pi_g$ core states. On the other hand, $1^2\Sigma_u^+$ and $2^2\Sigma_u^+$ core states (Figs. 3.9a, f) have always the character of the corresponding pure core state, independent of the cluster size. It is because Φ_0^C and Φ_8^C are energetically isolated from all the S-states. The transition from $1^2\Sigma_u^+$ to $2^2\Sigma_u^+$ is vibronically allowed for Ar_3^+ [22] and observed in the UV region up to $n = 7$ [26]. The present work suggests that the UV band does not shift with the cluster size. The $1^2\Pi_u$ and $2^2\Pi_u$ core states (Figs. 3.9b, e) show an intermediate behavior, since the energy levels of (Φ_1^C, Φ_2^C) and (Φ_4^C, Φ_5^C) are in the lower and upper marginal region of the level distribution of the S-states, respectively. As the cluster size increases, the upper part of the S-state begins to overlap with $2^2\Pi_u$ core state (Φ_4^C, Φ_5^C), while the $1^2\Pi_u$ core state (Φ_1^C, Φ_2^C) stays near the lower boundary of the distribution (see Fig. 3.6). Therefore, $2^2\Pi_u$ core state (Φ_4^C, Φ_5^C) interacts more strongly with the S-states. It is reflected in Fig. 3.9e: the $2^2\Pi_u$ core state shifts appreciably to a higher energy and a group of solvent states that are dominated by (Φ_4^C, Φ_5^C) evolves at ~ 2 eV.

3.4 Conclusion

1. The most stable structures of Ar_n^+, $n = 3 \sim 27$, were determined with the DIM model.

2. The shift of the absorption band in the size range from $n = 15$ to 20 [10,11] was well reproduced in the calculation. The shift was explained by an electronic interaction between the ion core and the surrounding solvent atoms. The interaction depended strongly on the position of the solvent atoms relative to the ion core.

3. Although the excited states of the ion core interacted strongly with the surrounding atoms, the character of Ar_3^+ remained even in the larger clusters.

Bibliography

[1] J. J. Sáenz, J. M. Soler, and N. García, Surf. Sci. **156**, 121 (1985).

[2] H. Haberland, Surf. Sci. **156**, 305 (1985).

[3] E. E. Polymeropoulos and J. Brickmann, Surf. Sci. **156**, 563 (1985).

[4] P. G. Lethbridge, G. Del Mistro, and A. J. Stace, J. Chem. Phys. **93**, 1995 (1990).

[5] P. J. Kuntz and J. Valldorf, Z. Phys. D–Atoms, Molecules and Clusters **8**, 195 (1988).

[6] I. Last and T. F. George, J. Chem. Phys. **93**, 8925 (1990).

[7] H. -U. Böhmer and S. D. Peyerimhoff, Z. Phys. D–Atoms, Molecules and Clusters **11**, 239 (1989).

[8] A. Ding and J. Hesslich, Chem. Phys. Lett. **94**, 54 (1983).

[9] I. A. Harris, R. S. Kidwell, and J. A. Northby, Phys. Rev. Lett. **53**, 2390 (1984).

[10] N. E. Levinger, D. Ray, M. L. Alexander, and W. C. Lineberger, J. Chem. Phys. **89**, 5654 (1988).

[11] H. Haberland, B. von Issendorff, T. Kolar, H. Kornmeier, C. Ludewigt, and A. Risch, Phys. Rev. Lett. **67**, 3290 (1991); Issendorff, H. Kornmeier, W. Orlik, T. Kolar, C. Ludewigt, T. Reiners, and A. Risch, in *Physics and Chemistry of Finite Systems*, edited by P. Jena, S. N. Khanna, and B. K. Rao (Kluwer, Dordrecht, 1992).

[12] W. Kamke, J. de Vries, J. Krauss, E. Kaiser, B. Kamke, and I. V. Hertel, Z. Phys. D–Atoms, Molecules and Clusters **14**, 339 (1989).

[13] G. Ganteför, G. Bröker, E. Holub-Krappe, and A. Ding, J. Chem. Phys. **91**, 7972 (1989).

[14] K. Mitsuke and K. Ohno, J. Phys. Chem. **93**, 501 (1989).

[15] T. Nagata, J. Hirokawa, and T. Kondow, Chem. Phys. Lett. **176**, 526 (1990).

[16] T. Nagata and T. Kondow, J. Chem. Phys. **98**, 290 (1993).

[17] R. G. Keesee, and A. W. Castleman, Jr., J. Phys. Chem. Ref. Data **15**, 1011 (1986).

[18] P. G. Le Comber, R. J. Loverland, and W. E. Spear, Phys. Rev. B **11**, 3124 (1975).

[19] M. Umehara, Phys. Rev. B **33**, 4237 (1986).

[20] K. Hiraoka and T. Mori, J. Chem. Phys. **90**, 7143 (1989).

[21] S. Wei, Z. Shi, and A. W. Castleman Jr., J. Chem. Phys. **94**, 8604 (1991).

[22] T. Ikegami, T. Kondow, and S. Iwata, unpublished data.

[23] W. R. Wadt, Appl. Phys. Lett. **38**, 1030 (1981).

[24] F. X. Gadea and M. Amarouche, Chem. Phys. **140**, 385 (1990).

[25] T. Nagata, J. Hirokawa, T. Ikegami, and T. Kondow, Chem. Phys. Lett. **171**, 433 (1990).

[26] M. J. DeLuca and M. A. Johnson, Chem. Phys. Lett. **162**, 445 (1989).

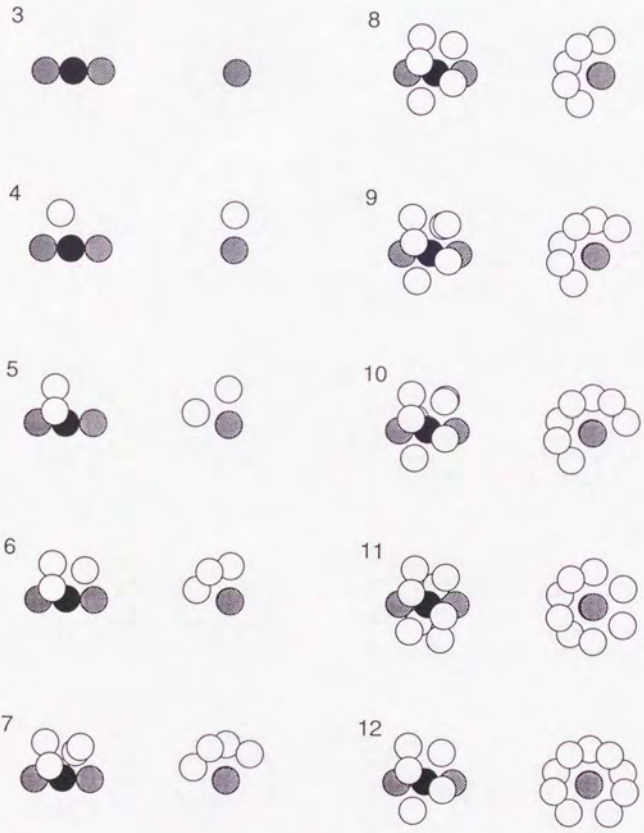
3
4
5
6
7
8
9
10
11
12

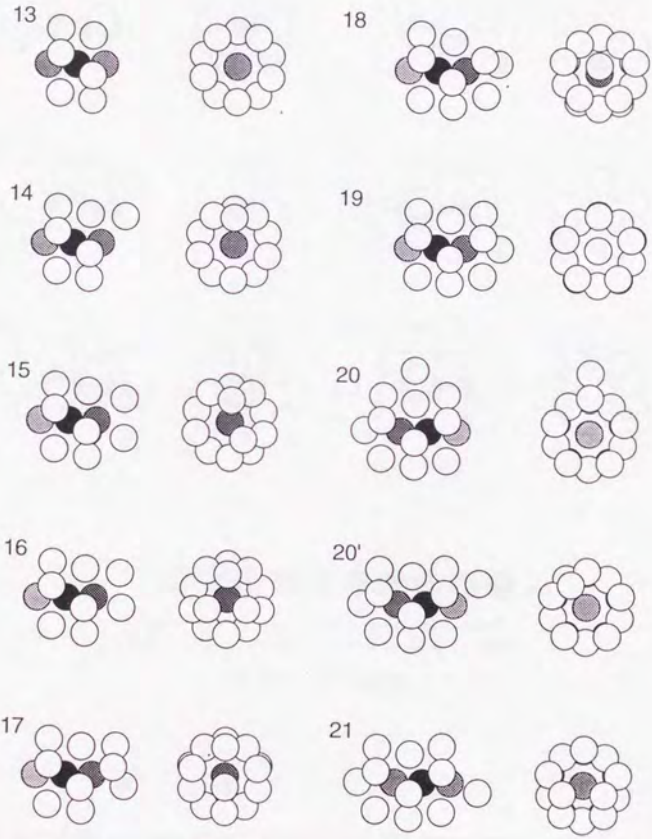
13
18
14
19
15
20
16
20'
17
21

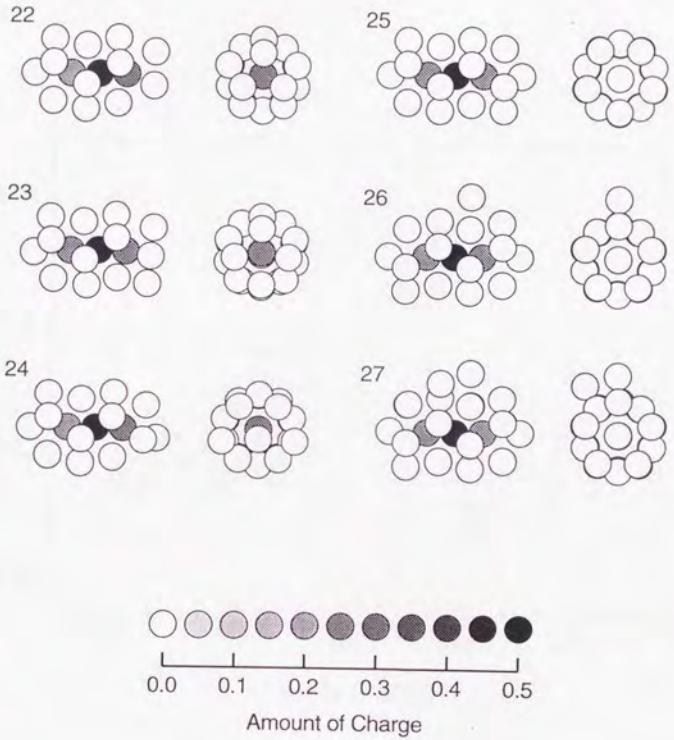

Figure 3.1: The most stable structures of Ar_n^+, $n = 3 \sim 27$. The structures are shown both in side- and end-views. The blackness of the shade on atoms reflects the charge density. Note that the figure is inverted from left to right between (20) and (20') to see the formation of the second cap more clearly.

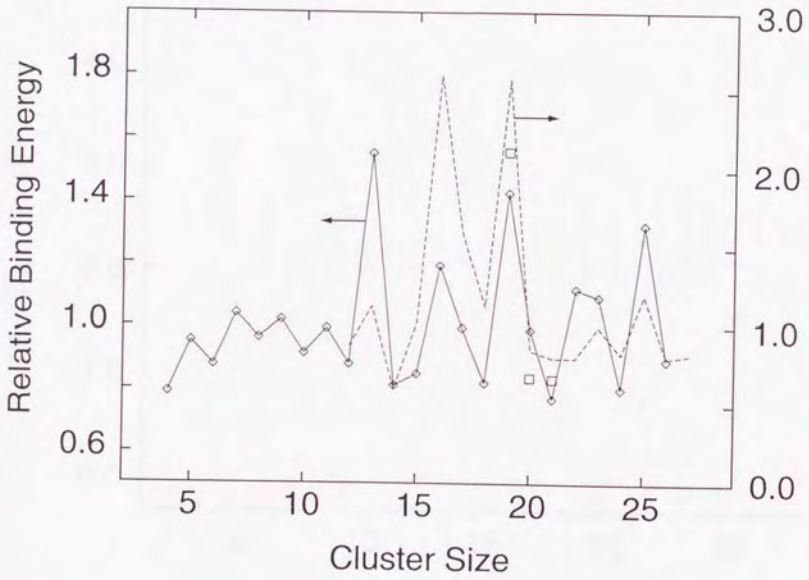

Figure 3.2: The ratio $\Delta E_n/\Delta E_{n+1}$ (relative binding energy) is calculated for the most stable structure and plotted by diamonds ($\diamond$). The boxes ($\square$) are evaluated using a local minimum structure of Ar_{20}^+ (see text). The experimental values for Xe_n^+ [21] are also shown by the broken line.

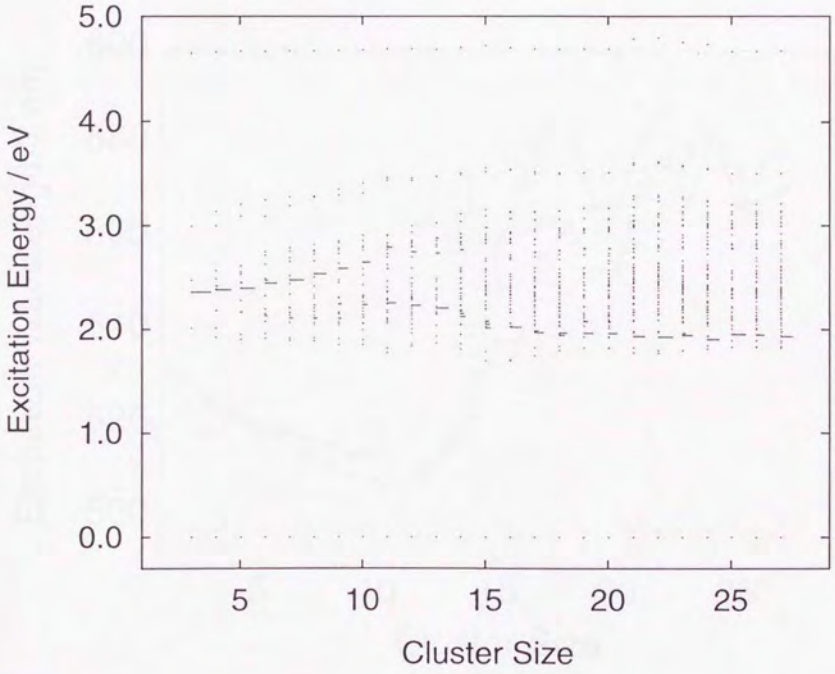

Figure 3.3: The oscillator strength distribution from the ground state. The abscissa and ordinate are the cluster size and the excitation energy, respectively. The length of the horizontal bar is proportional to the corresponding oscillator strength. Even the state having zero oscillator strength is shown by dot to indicate the energy position of the electronic state.

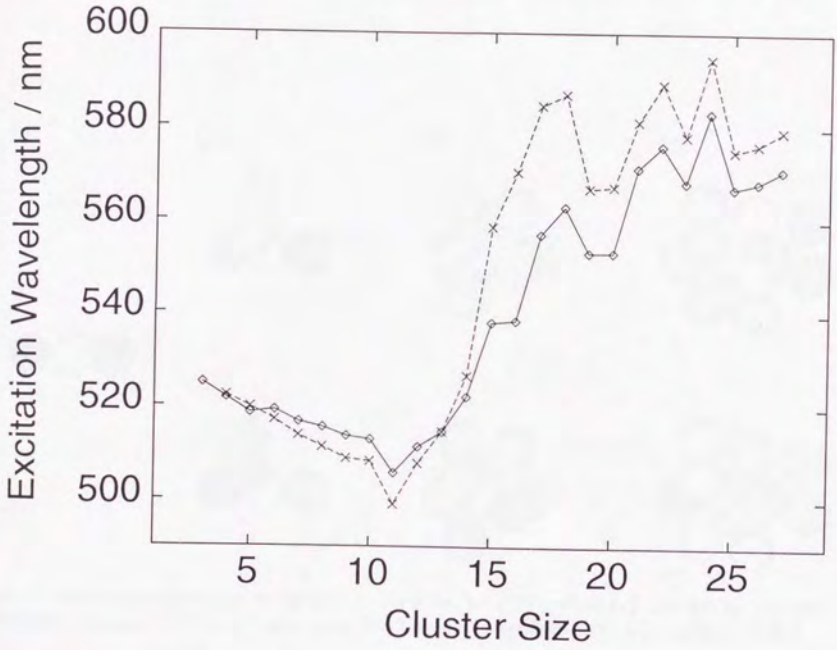

Figure 3.4: The expectation values of wavelength for the transition from the ground states. Diamonds (◇) are calculated from all the electronic state. Xes (×) are calculated from the two-level solvated ion core model (see text).

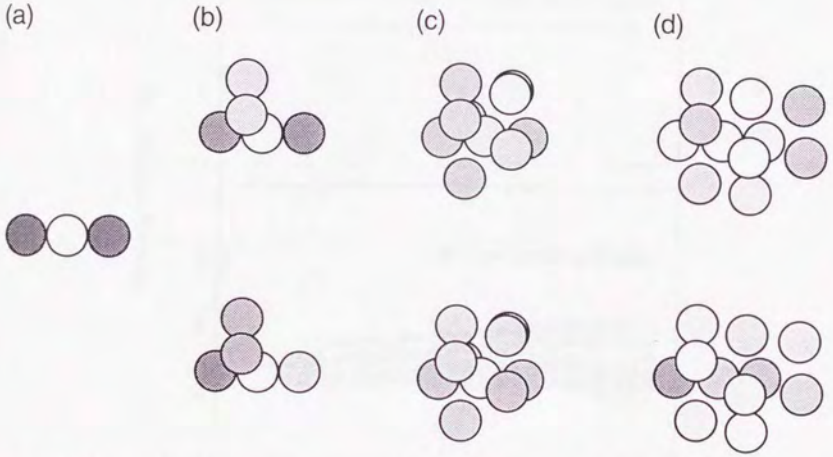

Figure 3.5: The charge distributions of the photoexcited state. (a) $1^2\Sigma_g^+$ state of Ar_3^+. (b)~(d) the electronic excited state belonging to H-branch (upper figure) and L-branch (lower figure). (b) Ar_5^+, (c) Ar_{10}^+, (d) Ar_{16}^+.

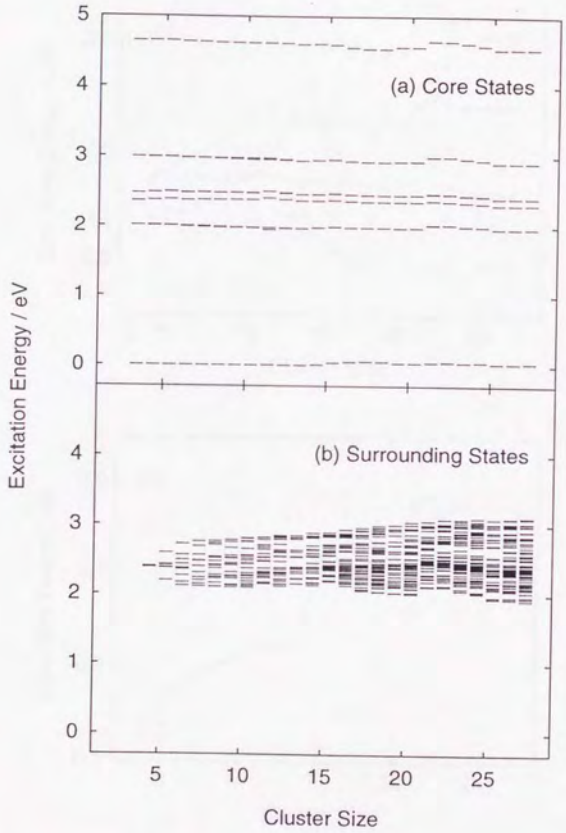

Figure 3.6: The energy levels of C-states and S-states. The abscissa and the ordinate are the cluster size and the energy of the C- or S-states relative to the ground state, respectively. (a) C-states, (b) S-states.

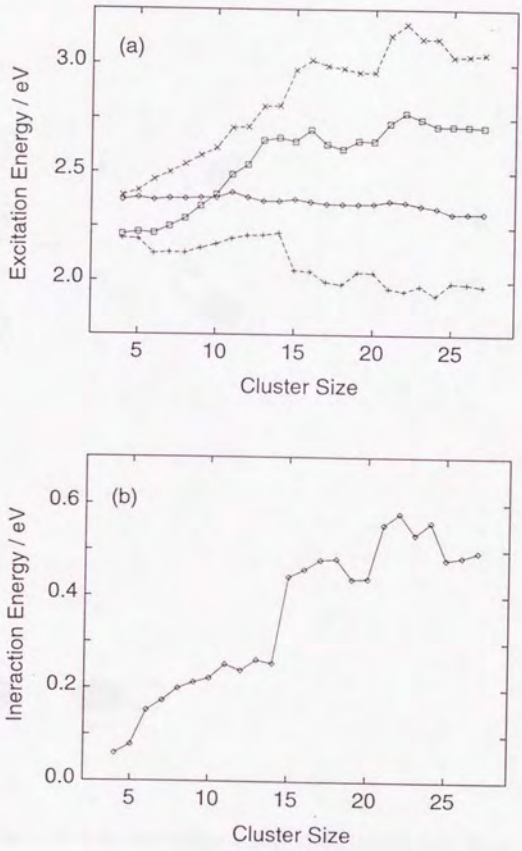

Figure 3.7: The n-dependence of the two-level model. (a) The energy of Ψ_L (+) and Ψ_H (×) in the two-level model, and the diagonal elements of Φ_3^C (◇) and Φ_{eff}^S (□). (b) The off-diagonal element $\langle \Phi_3^C | \mathcal{H} | \Phi_{eff}^S \rangle$.

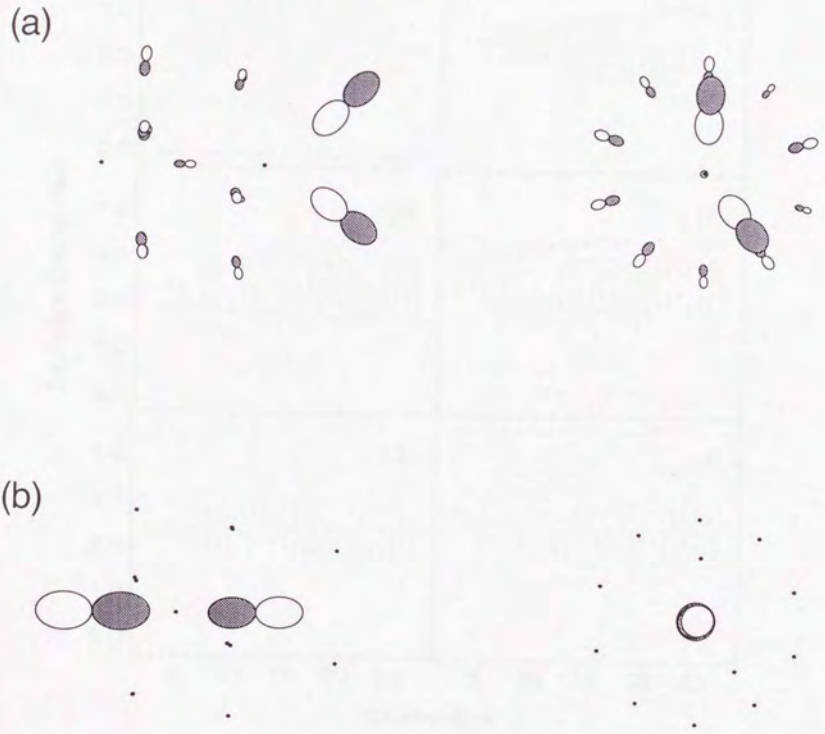

Figure 3.8: The schematic views of the hole orbitals in Ar_{15}^{+}. Left: the side view, Right: the end view. The darkness distinguishes a sign of the orbital. (a) Φ_3^C, (b) Φ_{eff}^S.

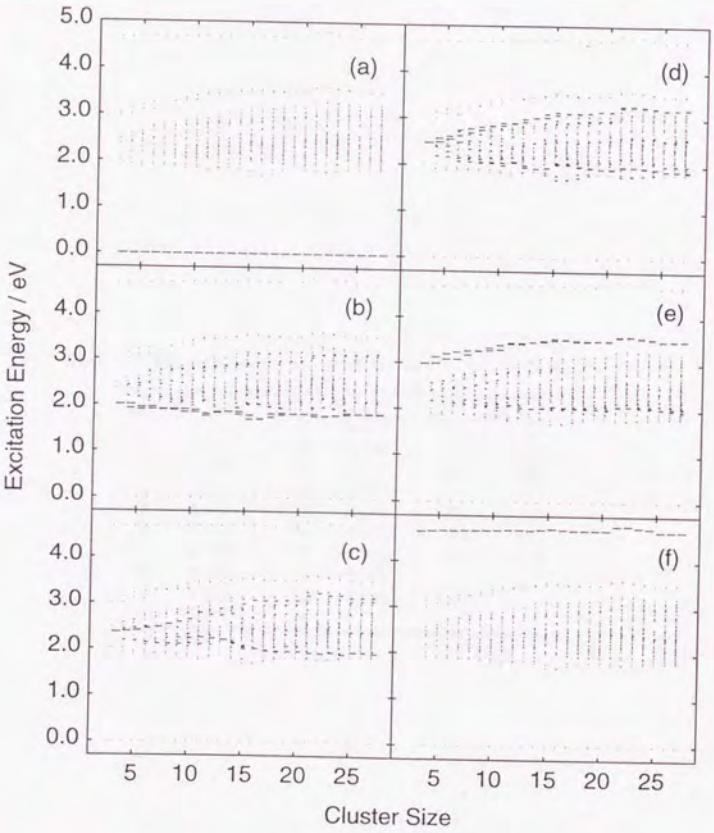

Figure 3.9: The absolute value of the inner product, Eqs. 3.3 and 3.4, between the true eigenstates of Ar_n^+ and the C-states. The abscissa and ordinate are the cluster size and the excitation energies. The length of the horizontal bar is proportional to the corresponding inner product. Even the state having zero inner product is shown by dot to indicate the energy position of the electronic state. (a) $1^2\Sigma_u^+$ (Φ_0^C), (b) $1^2\Pi_u$ (Φ_1^C, Φ_2^C), (c) $1^2\Sigma_g^+$ (Φ_3^C), (d) $1^2\Pi_g$ (Φ_4^C, Φ_5^C), (e) $2^2\Pi_u$ (Φ_6^C, Φ_7^C), (f) $2^2\Sigma_u^+$ (Φ_8^C).

Table 3.1: The stabilization energy of Ar_n^+ in the most stable structure.

n	E_n / eV	n	E_n / eV	n	E_n / eV
		11	−2.076	21	−2.773
		12	−2.151	22	−2.849
3	−1.558	13	−2.237	23	−2.916
4	−1.604	14	−2.293	24	−2.978
5	−1.663	15	−2.361	25	−3.055
6	−1.724	16	−2.441	26	−3.113
7	−1.795	17	−2.508	27	−3.178
8	−1.862	18	−2.575		
9	−1.932	19	−2.658		
10	−2.001	20	−2.715		

Chapter 4

Molecular dynamics

Abstract

The photoabsorption spectra of argon cluster ions, Ar_n^+, are calculated for $n = 4$ to 25. The internal motion of the cluster is accounted for by the molecular dynamics method. The diatomics-in-molecules (DIM) potential energy surface is used for the calculation. There are basically two peaks in the spectra. At a low internal energy, the primary peak shifts from 510 nm to 550 nm at $n \simeq 10$, and then shifts abruptly to 600 nm at $n \simeq 14$. As the internal energy increases, the spectra become broad and the clear transition disappears. The spectral shift is explained by the solvation of the ion core in the cluster, with the rest of the constituent atoms acting as solvent atoms. The first red shift is due to the crossover of the energy levels between the ion core and the solvent shell. The second one takes place because the solvation energy is increased abruptly, which is explained in terms of the structural change in the solvation shell.

4.1 Introduction

What is the color of the argon clusters? It is transparent, of course, as both the gas phase and the crystal phase of the argon are colorless in the visible and the UV regions. On the other hand, the argon cluster *cations* Ar_n^+ are tinted [1–6,6–10]. The molar absorption coefficient of Ar_3^+ at 520 nm is indeed as large as 9×10^4 $mol^{-1}dm^3cm^{-1}$ [2], which is larger than that of the permanganate ion MnO_4^{2-}·aq by a factor of 10! For the larger clusters, the charge is localized on the central three atoms in the cluster ion forming the Ar_3^+ ion core [7–15], which acts as a chromophore within the cluster.

The peak wavelength of this strong absorption band is shifted toward red as the cluster size n increases [7,8]. Levinger *et al.* first observed the red shift as n increases from 15 to 20 in an one-step manner. From their n-dependence of the photodissociation cross sections at several wavelengths, the peak position is shifted from 520 nm to 600 nm as n increases from 15 to 20. The further shifting was not observed for the larger clusters. Recently, Haberland *et al.* have measured the whole photodissociation spectra for each cluster up to $n = 60$ [8], and found that the spectral shift occurs in a two-step manner. The peaks in their spectra shift from 510 nm to 540 nm as n increases from $n = 6$ to 9, and then shift to 590 nm as n increases from 16 to 21.

In Chapter 3, we determined the most stable structures of the argon clusters and found that the expected peak positions in these zero Kelvin structures do shift to red as the cluster size n increases. The red shift occurs in a one step manner from $n = 11$ to 18, in good agreement with the Levinger's observation. However, we failed to explain the behavior observed by Haberland, especially the first red-shift occurred between $n = 6$ and 9. The calculated peak position was, on the contrary, shifted to blue in the cluster size from $n = 3$ to 10.

In fact, an important aspect of the cluster was not accounted for in the previous calculations: The thermal motion of the cluster was ignored. The amount of the red shift is strongly dependent on the position of the solvent argon atoms relative to the Ar_3^+ chromophore. Since the structure of the cluster is very floppy, the spectra of the cluster may be heavily affected by the thermal motion.

In this chapter, the finite temperature effects on the spectra are examined by using the molecular dynamics method. The thermal nuclear motion of the cluster is also discussed from the view point of the solvation effect.

4.2 Calculation

4.2.1 Trajectory calculation

The classical molecular dynamics is calculated on the potential energy surface of the electronic ground state. The nuclear equation of motion is written as

$$\frac{dQ_i}{dt} = \frac{P_i}{m_i} \tag{4.1}$$

$$\frac{dP_i}{dt} = F_i, \tag{4.2}$$

where i is the index to the constituent atoms, Q_i is the position of the i-th atom, P_i is the momentum associated with Q_i, and m_i is the mass of the i-th atom. The forces exerted on the nuclei, F_i, are obtained from the gradient of the potential energy surface of the electronic ground state. The potential surface is calculated from the DIM Hamiltonian, which is documented in Chapter 2. The analytical gradient method is also described there.

The Eqs. 4.1 and 4.2 are numerically integrated by using the Adams' formula. The fourth order predictor and the fifth order corrector are employed:

$$x_0 = x_1 + \frac{h}{720}(1901dx_1 - 2774dx_2 + 2616dx_3 - 1274dx_4 + 251dx_5) \tag{4.3}$$

$$x = x_0 + \frac{h}{288}(95dx_0 - 475dx_1 + 475dx_2 - 475dx_3 + 475dx_4 - 95dx_5) \tag{4.4}$$

where x is an integrand (Q and P), h is width of an integral step, x_1 is the x value in the previous step, and dx_i is a time derivative of x at i steps before. The derivative dx_0 is calculated by using a set of x_0. The fourth order Runge-Kutta method is used for the preparation at the startup.

The integration time step is $h = 2.4$ fs. To calculate the gradient, the electronic wave function Ψ_g must be re-calculated step-by-step at each geometry. To avoid a full diagonalization of the Hamiltonian matrix, Ψ_g is solved with the inverse iteration method associated with the Cholesky decomposition of the Hamiltonian matrix. The initial value is taken from the Ψ_g in the previous time step, and the origin of the energy is properly shifted to accelerate the convergence.

The trajectory calculation is started at high internal energy: about 20 % of the trajectories dissociate thermally within 6 ps. The translational and the rotational motions of the cluster are eliminated at the very beginning of the trajectory. The surviving trajectories are annealed for $10 \sim 25$ ps down to an appointed internal energy. The origin of the internal energy is taken at the energy of the most stable structure [10] with no kinetic energy. The annealing process is followed by an idling run of 1.2 ps and then, 50 snap shots of the trajectory are sampled at every 97 fs intervals. A Total number of 2500 snap shots are sampled from 50 independent trajectories. The drift of the total energy is confirmed to be less than 0.01 % throughout the sampling processes. The momenta of the center of mass and the angular momenta around the center of mass are also confirmed to remain at the initial value of zero.

4.2.2 Spectrum calculation

The photoabsorption spectrum is calculated as an ensemble average among the snap shot structures sampled from the trajectories. The photoabsorption rate W_{if} from the initial state i to the final state f of a randomly

oriented molecule is written as

$$W_{if} = s_0 |M_{if}|^2 I(\omega_{if}) \tag{4.5}$$

$$s_0 = \frac{1}{4\pi\epsilon_0}\frac{4\pi^2}{3c\hbar^2}, \tag{4.6}$$

where $\hbar\omega_{if}$ is the excitation energy from i to f, $I(\omega)d\omega$ is the energy of the linearly polarized light at the angular velocity of $\omega \sim \omega + d\omega$ passing through a unit area par a unit time, and M_{if} is the transition dipole moment between i and f. As the actual light source is not ideally monochromatic, the measured intensity of the light is not $I(\omega)$ but

$$I_{\rm obs} = \int_{\delta\omega} I(\omega)\, d\omega, \tag{4.7}$$

where the integration is performed over the line width of the light source $\delta\omega$ at the transition frequency ω_{if}. The number density of photons n_c is defined by

$$I_{\rm obs} = n_c c\, \hbar\omega_{if}. \tag{4.8}$$

The photoabsorption cross section from i to f, σ_{if}, is then defined by

$$W_{if} = \sigma_{if} n_c c. \tag{4.9}$$

Inserting (4.5) and (4.8) into (4.9), we obtain

$$\sigma_{if} = s_0 \hbar\omega_{if} |M_{if}|^2 \frac{I(\omega_{if})}{I_{\rm obs}}. \tag{4.10}$$

The photoabsorption cross section to a discrete excited state, σ_{if}, is dependent on the property of the light source, namely the shape of $I(\omega)$. However, if the final state f is distributed continuously around $\delta\omega$, Eq. 4.10 may be integrated over f smearing out the $I(\omega)$ dependence. If $\delta\omega$ is small enough that $\hbar\omega_{if}|M_{if}|^2$ does not change much in the integral region, the integration of Eq. (4.10) over f results in

$$\sigma_{\rm obs} = s_0 \hbar\omega_{if} |M_{if}|^2 \frac{df}{d\omega}, \tag{4.11}$$

by substituting the integral variable f for ω. Note that the observed cross section is not an average of σ_{if} but a sum of them.

To calculate $\sigma_{\rm obs}$ from the ensemble of the MD structure, the eq. (4.11) is averaged over some finite $\Delta\omega$ range:

$$\sigma_{\rm obs} \simeq \frac{1}{\Delta f}\int_{f\in\Delta f} s_0 \hbar\omega_{if} |M_{if}|^2\, df\, \frac{\Delta f}{\Delta\omega}. \tag{4.12}$$

The transition dipole moment M_{if} is written as

$$M_{if} = \langle \Phi_i(Q) | \mu_{if}(Q) | \Phi_f(Q) \rangle, \tag{4.13}$$

where Φ_i and Φ_f are the nuclear wave function of the initial and the final state, respectively, and μ is the dipole operator. Here, the integration over the electronic coordinates has already been performed, and $\langle\rangle$ means the integration over the nuclear coordinates only. Approximating Φ_f by the delta-function, $\Phi_f = \delta(Q - Q_f)$, we obtain

$$\sigma_{\rm obs} \simeq \frac{1}{\Delta\omega} \int_{f\in\Delta f} s_0 \hbar\omega_{if} |\Phi_i(Q_f)|^2 |\mu_{if}(Q_f)|^2 \, df. \tag{4.14}$$

Assuming that the integration in eq. (4.14) can be replaced by an ensemble average over the sampled MD structures, the final expression becomes

$$\sigma_{\rm obs} \approx \frac{1}{N_s} \frac{1}{\Delta\omega} \sum_{k=1}^{N_s} \sum_{j\in\Delta\omega} s_0 \hbar\omega_{ij} |\mu_{ij}(Q_k)|^2, \tag{4.15}$$

where the sum over k is taken for the sampled structures, and the sum j runs over the excited states at the k-th structure. In the final expression, all the possible choices of Φ_i and of the electronic states of f are included.

4.3 Results

The trajectories are calculated at several internal energies. The temperature T is defined by the amount of the internal energy E per degree of freedom:

$$E = (3n - 6)kT, \tag{4.16}$$

where k is the Boltzmann's constant. The photoabsorption spectra are shown in Figs. 4.1a–d for T = 10 K, 20 K, 40 K, and 60 K, respectively. The resolution of the spectra, $\Delta\omega$, is 10 nm. Note that the temperature of 60 K is high enough for the large cluster to dissociate in a time scale of nano seconds. Such dissociative trajectories could not be observed experimentally, but are calculated for comparison.

As the temperature increases, the spectrum becomes broader and the peak intensity is lowered significantly. However, a common feature still remains. The peak at 520 nm in the spectrum of the tetramer, which is very close to the spectrum of the trimer, persists up to $n = 10$. The peak shifts slightly to shorter wavelength with the increase of the cluster size. Meanwhile, the shoulder at $\sim$ 550 nm starts to grow for clusters with $n \simeq 8$, and overwhelms the 520 nm peak at around $n \simeq 11$. This newly formed peak then shifts abruptly to 620 nm at $n = 13 \sim 14$, and stays unchanged for $n > 15$.

The experimental spectra are observed at the wavelength longer than 500 nm [8]. For the comparison with the experimental work, the position of the first peak after 500 nm in the calculated spectra is obtained by fitting it to a gaussian function. They are indicated in Fig. 4.1 by small arrows. The wavelength at the peak is plotted in Fig. 4.2 as a function of the cluster size and is compared with the experimental results. The quantitative agreement with the experimental result is not satisfactory, but the two-step red shift feature is reproduced in the calculation at low temperatures.

4.4 Discussion

4.4.1 Anisotropy of the solvent effect

As was discussed in Chapter 3, the spectral red shift is due to the solvent effect of neutral argon atoms on the Ar_3^+ chromophore. To demonstrate the anisotropy of the solvent effect, the potential energy surface and the excitation wavelength of Ar_4^+ are depicted in Fig. 4.3 as a function of the position of a solvent atom. The geometry of the central Ar_3^+ ion core is fixed to that of Ar_3^+. The excitation wavelength is calculated from the averaged excitation energy weighted by the oscillator strength, $\Delta\bar{E}$:

$$\Delta\bar{E} = \frac{\sum_i f_{i0}(E_i - E_0)}{\sum_i f_{i0}}, \tag{4.17}$$

where E_i is the energy of the i-th excited state, f_{i0} is the oscillator strength between the i-th excited state and the ground state, and the sum is taken over all the excited states. A strong red shift occurs when the solvent atom attached near the ion core axis (an axial site), while the one attached at the side of the ion core (an equatorial site) does not cause the red shift. The appearance of the Fig. 4.3 does not change much by the deformation of the ion core.

The amount of the red shift is approximately additive with respect to an addition of solvent atoms. The excitation energy is estimated with the assumption of the additivity as

$$\Delta\bar{E}_n = \sum_{i=1}^{n-3}(\Delta\bar{E}_4^i - \Delta\bar{E}_3) + \Delta\bar{E}_3, \tag{4.18}$$

where $\Delta\bar{E}_3$ is the averaged excitation energy of the ion core calculated without the solvent atoms, and $\Delta\bar{E}_4^i$ is that of the tetramer ion constructed from the ion core and the i-th solvent atom. The shift in the excitation energy, $\Delta\bar{E}_n - \Delta\bar{E}_3$ and $\Delta\bar{E}_n - \Delta\bar{E}_3$, is compared for several structures in Fig. 4.4. These structures are sampled from trajectories of Ar_{15}^+ at the internal energy of 80 K. Though the estimated value, $\Delta\bar{E}_n - \Delta\bar{E}_3$, always overestimate the red shift, the deviation from the real value, $\Delta\bar{E}_n - \Delta\bar{E}_3$, is fairly small. Judging from the additivity, each solvent atom can be considered as an independent perturber on the photoexcited state of the ion core.

4.4.2 Distribution of the solvent atoms

Glancing through the trajectories, the cluster is always found to contain a trimer ion core. This basic structure remains unchanged even at the internal energy of 80 K. At high internal energy, one of the solvent atoms is occasionally substituted for one of the atoms that constitute the ion core. Excepting the period of the substitution reaction (about 1 ps per event), the trimer core is readily discriminated from the other solvent atoms. The solvent atoms are thus distinguished from the ion core, and their distribution around the ion core may be calculated.

Because of the additivity of the red shift with respect to the solvent atoms, a first approximation of the amount of the red shift may be estimated from the distribution of the solvent atoms around the ion core. The number of solvent atoms per unit volume is calculated as a function of a relative position from the ion core, and plotted in Fig. 4.5 for $n = 7$, 11, and 15. Note that the integration around the ion core axis is not performed, therefore the concentration near the axis is emphasized.

The distribution of the solvent atoms is not uniform, but it is clearly separated into two regions: the axial site and the equatorial site. They roughly correspond to the two potential wells in the Fig. 4.3a. At 10 K, for the cluster size between $n = 5$ and 13, all the solvent atoms are located in the equatorial site. The solvent atoms start to attach at the axial site from $n = 14$ to 18, but are slightly apart from the ion core axis (x axis in the figure); some of them are placed just on the axis from $n = 19$. The distribution of the solvent atoms described above closely reflects the most stable structure of Ar_n^+ [10], because many other isomers are still not accessible at 10 K. The tetramer ion is exceptional: not negligible amount of the sampled structures have a linear shape with the solvent atom positioned at the axial site [16]. In the larger clusters, the solvent atoms are likely to gather in the equatorial site to gain the van der Waals binding energy, because the potential well in the axial site is not broad enough to keep multiple solvent atoms. The tetramer has only one solvent atom, so that it is free from the van der Waals forces among the neutral solvent atoms, and the linear isomer is accessible. The peak due to the linear isomer is thus seen at 640 nm in the calculated spectrum in Fig. 4.1a. This peak becomes obscure as the internal energy of the cluster is raised. The experimental observation of the peak can be a good candidate for a thermometer of the cluster, though a good S/N ratio might be required.

There is a clear threshold between $n = 13$ and 14 at 10 K, where the solvent atoms start to attach at the axial site. The threshold becomes less clear as the internal energy is increased to 20 K. The axial solvent atoms are observed for $n = 4$ and 6, but are absent for $n = 5$ and 7. A weak peak appears at the axial site from $n = 8$, and becomes intense from $n = 10$. A difference from the distribution at 10 K is less significant for the larger clusters. Note that the structure of the cluster is still rigid at 20 K, at least for the smaller clusters. A few local minima on the potential surface can be assigned to each trajectory, and the cluster is just vibrating around them.

At 40 K the geometry of the cluster fluctuates greatly. Because the potential barrier that separates the two potential wells in Fig. 4.3a is 3.5 meV (40 K), the solvent atoms can move around the ion core at this internal energy. Many isomers are now accessible on a single trajectory calculation, and the axial solvent atoms are always observed for $n = 4$ thru 25. At 60 K, the solvent atoms move much more vigorously, but the distributions of them are similar to those calculated at 40 K.

The distribution of the solvent atoms described above is strongly reflected on the calculated spectra shown in Fig. 4.1. In Fig. 4.1a, there is a small peak at 640 nm in the spectrum of Ar_4^+, which is attributed to the linear isomers. The peak disappears from $n = 5$ to 13 and re-emerges suddenly at $n = 14$, being coincident

with the appearance of the axial solvent atoms. This peak can be used as an indicator showing whether axial solvent atoms are there or not. The shoulder at 640 nm appears at 40 K in the spectra of Ar_7^+, in coincident with the appearance of the axial solvent atoms. For Ar_{11}^+, the shoulder grows as the internal energy is increased and the distribution of the axial solvent atoms becomes intense and broad. The axial solvent atoms are always observed for Ar_{15}^+, so that the peak at 640 nm is resident for all internal energy investigated.

4.4.3 Solvated ion core model

The correlation between the spectral red shift at $n \simeq 14$ and the geometry of the cluster is revealed in the previous section. However, the early red shift near $n \simeq 10$ shown in Fig. 4.1 is not resolved yet. Here, the solvated ion core model [10] is applied on the ensemble of the present MD structures.

The detail of the solvated ion core model is described in Chapter 3. Briefly, the space spanned by a set of wavefunctions is divided into two subspaces: an ion core subspace and a solvent subspace. In the ion core subspace, the positive hole is localized on the trimer ion core, while in the solvent subspace, it is scattered among the solvent atoms. When the electronic Hamiltonian is diagonalized within the ion core subspace, nine eigen states are obtained. They are the electronic states of the ion core under the absence of the interaction with the solvent atoms. Among them, an eigen state that has maximum transition probability from the ground core state is picked up: it is taken as a photo-excited state of the ion core. A solvent state that interacts exclusively with the excited ion core state is extracted from the solvent subspace. The interaction between the solvent state and the rest of 8 core states causes the shift in the energy level of the solvent state, which is accounted for variationally.

The distributions of the energy levels of the excited ion core state $E_{\rm core}$ and the solvent state $E_{\rm solv}$ are calculated at 10 K, and are plotted in Fig. 4.6a. The distribution of the interaction energy $H_{\rm int}$ between them are also plotted in Fig. 4.6b. The distribution of $E_{\rm core}$ is resident near 520 nm. Meanwhile, the energy level of the core state $E_{\rm solv}$ is first distributed below $E_{\rm core}$ but shift to a higher energy as the cluster size is increased. The peak of the core state distribution crosses $E_{\rm core}$ at $n = 10$, settles down near 470 nm, and shifts further to 450 nm at $n = 20$. The interaction energy $H_{\rm int}$ becomes large as the cluster size is increased. It first increases asymptotically up to 0.24 eV from $n = 4$ to 13, jumps to 0.45 eV at $n = 14$, and then shifts further to 0.57 eV from $n = 20$.

The shift of $H_{\rm int}$ correlates with the distribution of the solvent atoms around the ion core. The abrupt increase of $H_{\rm int}$ at $n = 14$ is a result of the appearance of the axial solvent atoms. As no prominent changes are found in the distribution of $E_{\rm core}$ and $E_{\rm solv}$, the spectral shift at $n = 14$ in Fig. 4.1a is attributed to this increase of $H_{\rm int}$. Here, $E_{\rm core}$ is smaller than $E_{\rm solv}$, so that it is pushed down by the strong interaction. To see the correlation more clearly, the ensemble of $n = 14$ at 10 K is divided into two groups regarding the magnitude

of H_{int} (see Fig. 4.7). There are two peaks at 0.25 eV and 0.45 eV in the distribution of H_{int}. The structures belonging to the first peak ($H_{int} < 0.3$) are collected as the small H_{int} group, and those for the second peak ($H_{int} > 0.4$) are attributed to the large H_{int} group. The distribution of the solvent atoms is calculated for each group, and is shown in Fig. 4.7. The numbers of the structures in the small and the large H_{int} groups are 835 and 1250, respectively. As expected, the small H_{int} group has few axial solvent atoms, while large amount of axial solvent atoms is observed in the large H_{int} group.

The other small shift of H_{int} started at $n = 20$ coincides with a completion of the solvent cap at one end of the ion core. The distribution of H_{int} for Ar_{21}^+ shown in Fig. 4.6b is bimodal, peaking at 0.45 eV and 0.6 eV. The typical structures contained in both peaks are shown in Fig. 4.8. The solvent shell is opened at one end of the ion core in the small H_{int} structure (Fig. 4.8a). The structure is principally close to the most stable structure, where two solvent atoms attach on one end of the ion core besides the pentagonally pyramidal cap on the other end. Those solvent atoms is moved to the second solvation shell in Fig. 4.8a, leaving one end of the ion core free from the solvent atom. On the contrary, the high H_{int} structure has no similarity to the most stable structure. The solvent cage is constructed from two three-membered rings capping both ends of the ion core, and two distorted six-membered rings sandwiched between them. Those three-membered rings interact effectively with the core state, resulting in the large H_{int}. Though the increase of H_{int} is detected at $n = 20$, there is no noticeable change in the calculated photoabsorption spectra. It is because E_{solv} is shifted to the higher energy at the same time and the gap between E_{core} and E_{solv} is widened, canceling the increase of H_{int}.

Discrepancy between the calculated peak shift and the experimental one shown in Fig. 4.2 indicates that H_{int} is overestimated in our calculation. It is possible that our potential energy function is deficient, and the axial solvent atoms do not in reality appear until $n \simeq 20$. However, an experimental study on the photodissociation of Ar_n^+ [15] indicates the existence of the axial solvent atoms from $n = 14$. The location of the potential wells in Fig. 4.3a are closer to the ion core than that in an *ab initio* result [13], probably due to the neglect of the overlap integrals in the DIM calculation. The interaction energy H_{int} might become large enough only after both ends of the ion core are capped by the solvent atoms, as the spectral red shift is sensitive to the position of the solvent atoms (see Fig. 4.3b).

There is no change at $n = 10$ in the distribution of H_{int}, though the spectral shift is observed in Fig. 4.1. The red shift here is due to the crossover between E_{core} and E_{solv}. In the smaller clusters, E_{core} is pushed up as a result of the interaction between the core and the solvent state. A little blue shift is observed in Fig. 4.2, as H_{int} is small. For the larger clusters, E_{core} becomes lower than E_{solv}, and is pushed down considerably by the large H_{int}. The solvent state also gets contaminated with the core state, and acquires small transition probability from the ground state. Since the energy level E_{solv} is pushed up by H_{int}, it appears as small peaks around 450 nm.

The internal energy dependencies of the distributions of E_{core}, E_{solv}, and H_{int} are shown in Fig. 4.9 for

$n = 7$, 11, and 15, along with the calculated photoabsorption spectra. As the internal energy is increased, the distributions of E_{core} and E_{solv} become slightly broader, but the overall tendency is the same. The distribution of H_{int} becomes much broader, indicating that the spectral broadening is mostly controlled by the distribution of H_{int}. The peak at 0.45 eV appears at smaller cluster sizes for the high internal energy, as a result of the early appearance of the axial solvent atoms.

4.4.4 Characterization of the ensemble

Since the magnitude of H_{int} is sensitive to the geometry of the cluster, it can be used as a probe for this geometry. As shown in Fig. 4.7, there are two types of structures in Ar_{14}^+; one has axial solvent atoms, and the other doesn't. The former has a large H_{int} and the latter a small one, so that it is possible to monitor the transition between these structures through H_{int}. A single long trajectory is calculated for Ar_{14}^+, and the variation of H_{int} is plotted in Fig. 4.10. At 10 K, the cluster vibrates around the structure with large H_{int}. One of representative structures is shown in Fig. 4.11a. The stable triangular cap is formed on the right axial region, which is responsible to the large H_{int}. At 20 K, the trajectory stays basically at the small H_{int} structures, but the large H_{int} structure appears on occasion. The typical small and large H_{int} structures in the trajectory are shown in Fig. 4.11b and c, respectively. The small H_{int} structure is close to the most stable structure of Ar_{14}^+, in which one solvent atom is hanging from the solvent shell of Ar_{13}^+. The solvent atom occasionally moves to the axial region, and the large H_{int} structure as in Fig. 4.11c appears. The large H_{int} structure at 20 K is different from that at 10 K: only a single atom is attached at the axial region, and its position is not so stable. Besides the axial solvent atom, the other equatorial solvent atoms form a firm solvation shell around the ion core. At 40 K and 60 K, the solvent atoms move vigorously and the substitution reaction involving the exchange of ion core and solvents atom takes place frequently. No solid solvation shell can be assigned to the trajectories.

The distribution of H_{int} for the long trajectory is compared with that of the ensemble of structures used in the spectrum calculation, to view the property of the ensemble from the interaction energy. The results are shown in Fig. 4.12. At 10 K and 20 K, there are significant differences between the distribution for the long trajectory and that for the aggregate of short trajectories. The potential barrier between several isomers is too high for the clusters to overcome at these internal energies. Therefore, the single long trajectory is not sufficiently long to cover the accessible phase spaces. It would require an impractically long trajectory to accomplish this. The fifty short trajectories are employed in the spectrum calculation, but it might be still unsatisfactory, as the number of the structural isomers increases explosively with the degree of freedom [17]. If more trajectories were incorporated in the calculation, the spectrum shown in Fig. 4.1a and b might be much broader. On the other hand, both of the distributions are similar at 40 K and 60 K, due to the highly variable configurations adapted by the solvent atoms around the ion core. At these internal energies, the system behaves

ergodically with respect to $H_{\rm int}$. The fluctuation within each short trajectory is narrower, indicating long time fluctuations play an important role in the distribution of $H_{\rm int}$.

In addition to the constant internal energy ensemble, constant temperature ensembles are also calculated. The kinetic energy of the cluster is kept constant in this ensemble, so that all the isomers are accounted for equally, even though the potential barrier between them is too high to overcome. Note that in the constant internal energy ensemble, a high energy isomer has less kinetic energy, and even higher energy isomers are not accessible. The spectra are broader for the constant temperature ensemble, especially at low temperatures. The high $H_{\rm int}$ structures are observed even for the small clusters, since high energy isomers become accessible as described above. The overall spectral shapes are similar to those for the constant internal energy ensemble. At 10 K, however, the spectra for the intermediate sized clusters of $10 \leq n \leq 13$ are different: the prominent peak in Fig. 4.1a is corrupted and a tail toward long wavelength arises. The energy levels of $E_{\rm core}$ and $E_{\rm solv}$ distribute closely in this size range, so that the spectra are very sensitive to $H_{\rm int}$. In the constant temperature ensemble, the structures with different $H_{\rm int}$, such as those in Fig. 4.11a and b, are treated independently, which results in the flat spectra.

4.5 Conclusion

A formula to calculate a photoabsorption spectrum from classical trajectories is derived and applied for the argon cluster system. In the calculated trajectories, the trimer ion core is intact even at high internal energy, and can be distinguished from the solvent atoms. The calculated spectra shift toward red with increasing cluster size, qualitatively reproducing the experimental observations. The red shift at $n \simeq 10$ is explained from the crosover of the energy levels between the ion core and the solvent shell. The other shift at $n \simeq 14$ is due to the increase of the solvation interaction between the ion core and the solvent shell. The magnitude of the interaction energy is correlated well with the structure of the solvent shell around the ion core. The correlation is attributed to the anisotropic interaction between the photoexcited state of the ion core and the solvent atoms.

Bibliography

[1] Z. Y. Chen, C. R. Albertoni, M. Hasegawa, R. Kuhn, and A. W. Castleman Jr., J. Chem. Phys. **91**, 4019 (1989).

[2] N. E. Levinger, D. Ray, K. K. Murray, A. S. Mullin, C. P. Schulz, and W. C. Lineberger, J. Chem. Phys. **89**, 71 (1988).

[3] T. F. Magnera and J. Michl, Chem. Phys. Lett. **192**, 99 (1992).

[4] W. R. Wadt, J. Chem. Phys. **68**, 402 (1978).

[5] F. X. Gadea and M. Amarouche, Chem. Phys. **140**, 385 (1990).

[6] T. Ikegami, T. Kondow, and S. Iwata, J. Chem. Phys. **99**, 3588 (1993).

[7] N. E. Levinger, D. Ray, M. L. Alexander, and W. C. Lineberger, J. Chem. Phys. **89**, 5654 (1988).

[8] H. Haberland, B. von Issendorff, T. Kolar, H. Kornmeier, C. Ludewigt, and A. Risch, Phys. Rev. Lett. **67**, 3290 (1991); Issendorff, H. Kornmeier, W. Orlik, T. Kolar, C. Ludewigt, T. Reiners, and A. Risch, in *Physics and Chemistry of Finite Systems*, edited by P. Jena, S. N. Khanna, and B. K. Rao (Kluwer, Dordrecht, 1992).

[9] I. Last and T. F. George, J. Chem. Phys. **93**, 8925 (1990).

[10] T. Ikegami, T. Kondow, and S. Iwata, J. Chem. Phys. **98**, 3038 (1993).

[11] K. Hiraoka and T. Mori, J. Chem. Phys. **90**, 7143 (1989).

[12] P. J. Kuntz and J. Valldorf, Z. Phys. D–Atoms, Molecules and Clusters **8**, 195 (1988).

[13] H. -U. Böhmer and S. D. Peyerimhoff, Z. Phys. D–Atoms, Molecules and Clusters **11**, 239 (1989).

[14] T. Nagata, J. Hirokawa, and T. Kondow, Chem. Phys. Lett. **176**, 526 (1990).

[15] T. Nagata and T. Kondow, J. Chem. Phys. **98**, 290 (1993).

[16] T. Ikegami, W. Sakurai, and S. Iwata, unpublished data.

[17] M. R. Hoare, Adv. Chem. Phys. **40**, 49 (1979).

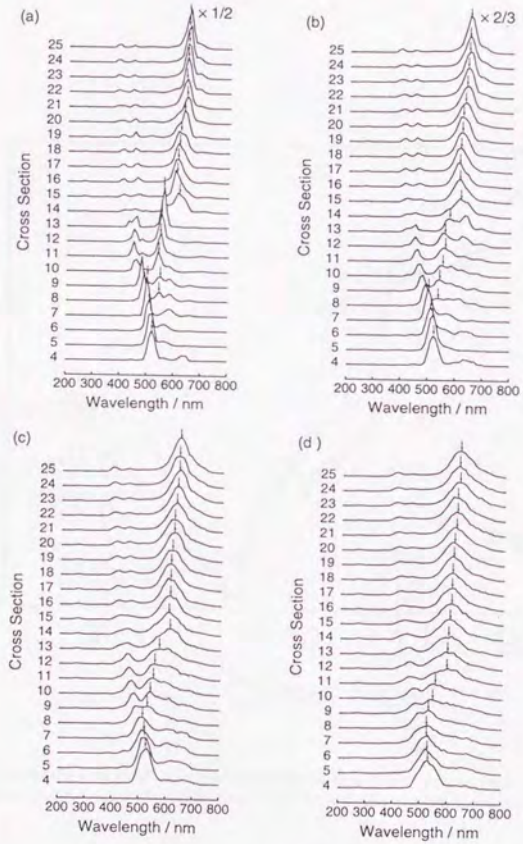

Figure 4.1: The photoabsorption spectra calculated from the trajectory calculations. The small arrow indicates the peak position obtained by fitting the first peak after 500 nm with the gaussian function. The temperature of the cluster is (a) 10 K (scaled by 1/4), (b) 20 K (scaled by 1/2), (c) 40 K, and (d) 60 K.

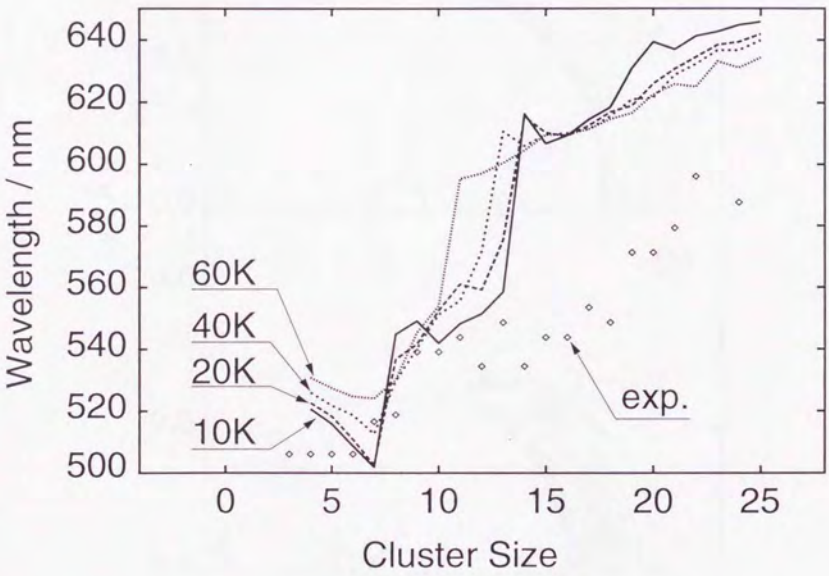

Figure 4.2: The positions of the first peak after 500 nm in the photoabsorption spectra are plotted as a function of the cluster size. Experimental results by Haberland *et al.* [8] are also plotted in diamond symbols.

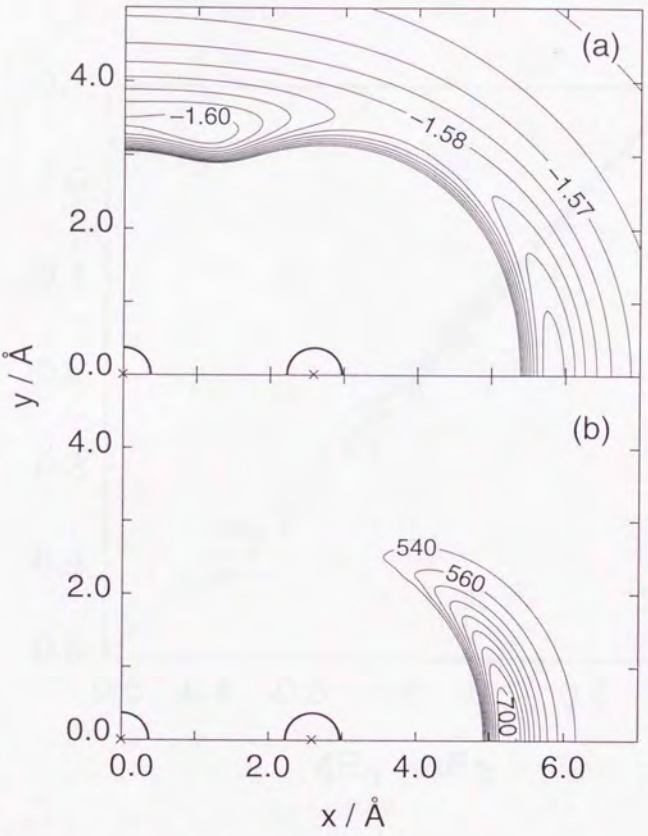

Figure 4.3: The potential energy surface of (a) the electronic ground state of Ar_4^+ and (b) the expectation value of the excitation wavelength. The geometry of the Ar_3^+ ion core is fixed at the symmetric linear shape with bond lengths of 2.6 Å, lying on the x-axis with the central atom placed at the origin. The abscissa and the ordinate represent the x- and y- coordinates of the solvent atom, respectively. Only the first quadrant is shown in the figure.

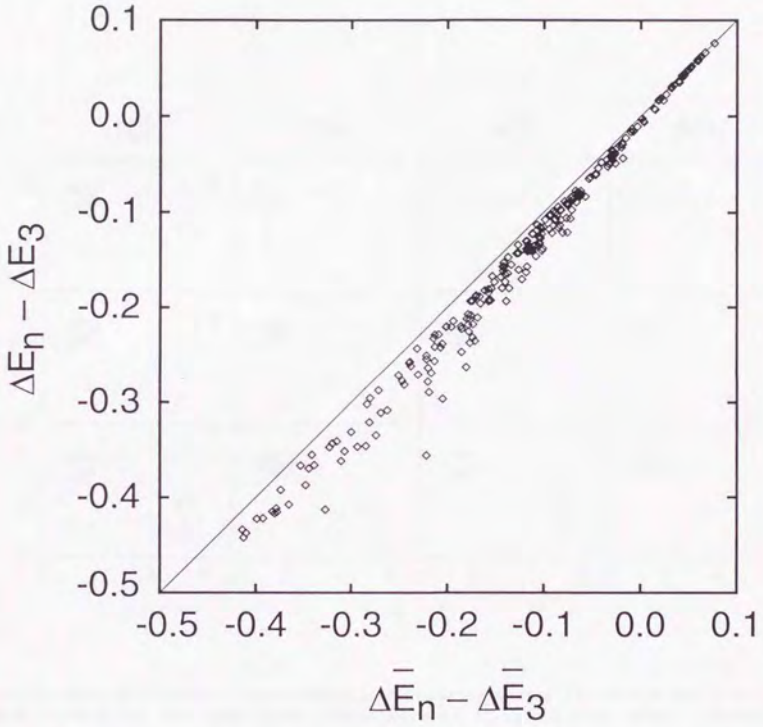

Figure 4.4: The additivity of the spectral red shift with respect to the addition of solvent atoms is demonstrated. The shift of the averaged excitation energy for Ar_{15}^+ is plotted on the abscissa. The shift of Ar_4^+ that constructed from the ion core and each solvent atom is summed up about the solvent atoms, and is plotted on the ordinate. The structures of Ar_{15}^+ are sampled from the trajectory calculation at 80 K. If the red shift were perfectly additive, all of the points would be plotted on the diagonal line.

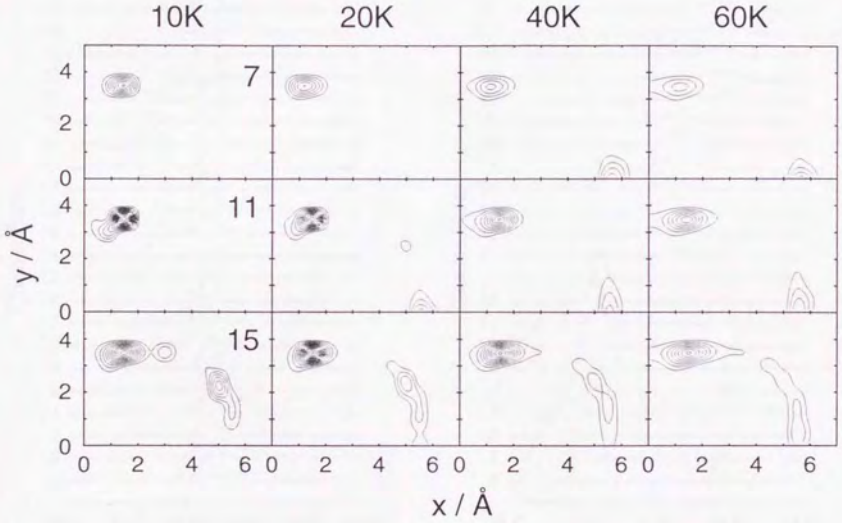

Figure 4.5: A number of the solvent atoms per unit volume around the ion core. The internal energies are 10 K, 20 K, 40 K, and 60 K from left to right, and the cluster sizes are 7, 11, 15 from top to bottom. The definition of the coordinate system is same as in Fig. 4.3. The integration around the ion core axis is not performed, therefore the concentration near the x axis is emphasized.

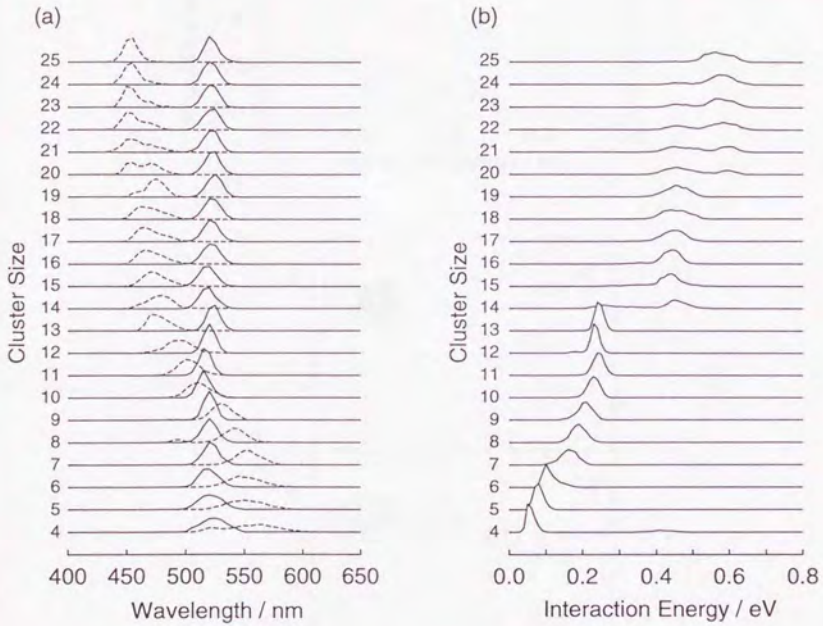

Figure 4.6: The excited ion core state and the solvent state is calculated for each structure sampled from the MD trajectory at an internal energy of 10 K. (a) The distributions of the energy levels of the excited core state and the solvent state. The core state is plotted in a solid line, while the solvent state is plotted in a broken line. (b) The distribution of the interaction energy between the excited core state and the solvent state.

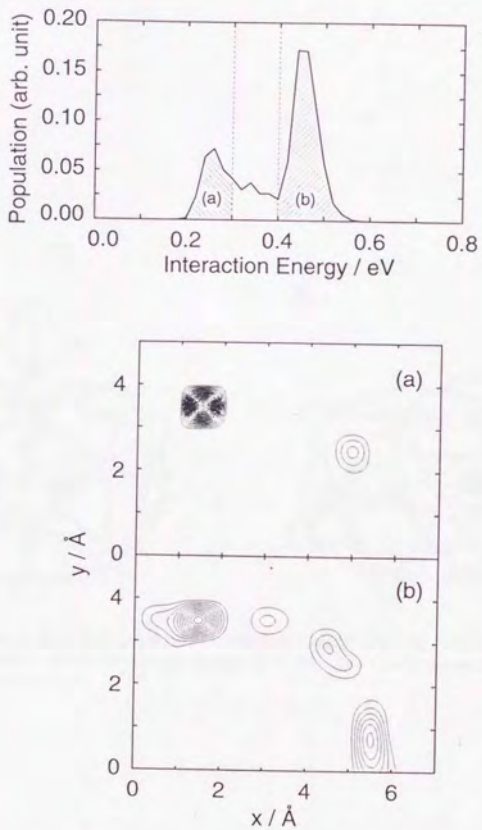

Figure 4.7: The distribution of the interaction energy between the core state and the solvent state for Ar_{14}^{+} at 10 K. The distribution of the solvent atoms for the structures with small interaction energy ($H_{\rm int} < 0.3$ eV) is shown in (a), while that with large interaction energy ($H_{\rm int} > 0.4$ eV) is shown in (b). The definition of the coordinate system in (a) and (b) is same as in Fig. 4.3.

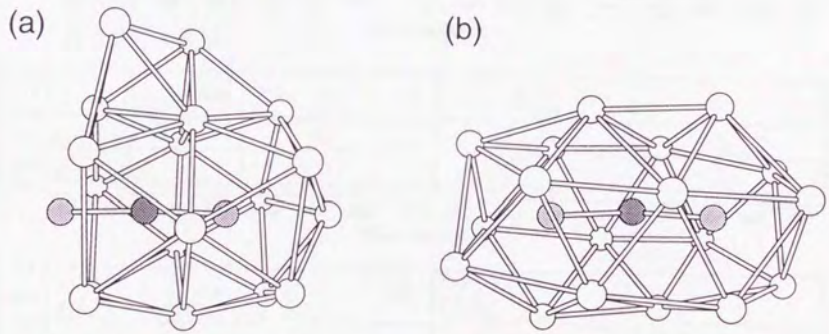

Figure 4.8: The structure of Ar_{21}^{+} with (a) a small interaction energy and with (b) a large interaction energy. The dark color of the atoms reflects the charge density on them. The bonds connecting between the solvent atoms are drawn as a guide of eyes.

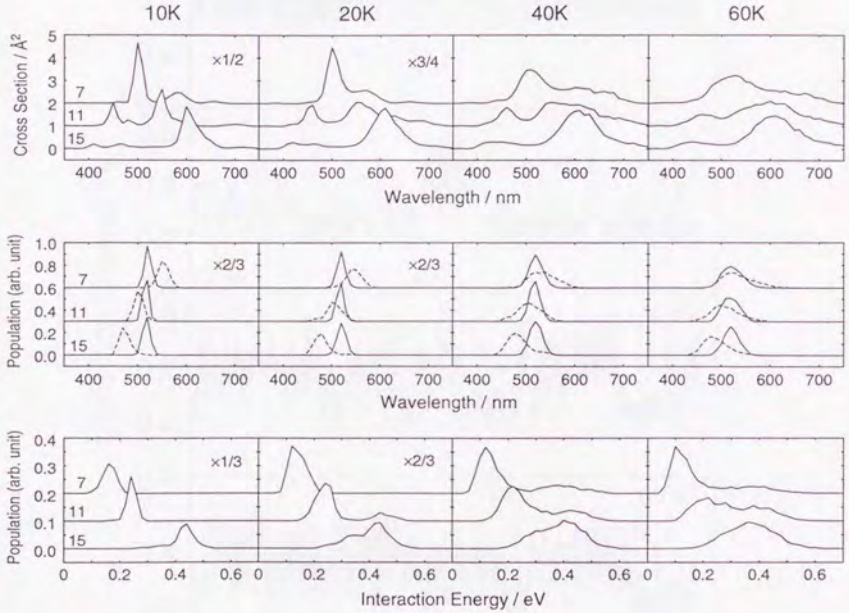

Figure 4.9: The internal energy dependence of the photoabsorption spectra, energy levels of the core state and the solvent state, and the interaction energy between them. Those cluster sizes of $n = 7$, 11, and 15 are shown in each figure from top to bottom. The internal energies are 10K, 20K, 40K, and 60K from left to right. In the middle figure, the distribution of the energy level of the core state is plotted in a solid line, and that of the solvent state is plotted in a broken line.

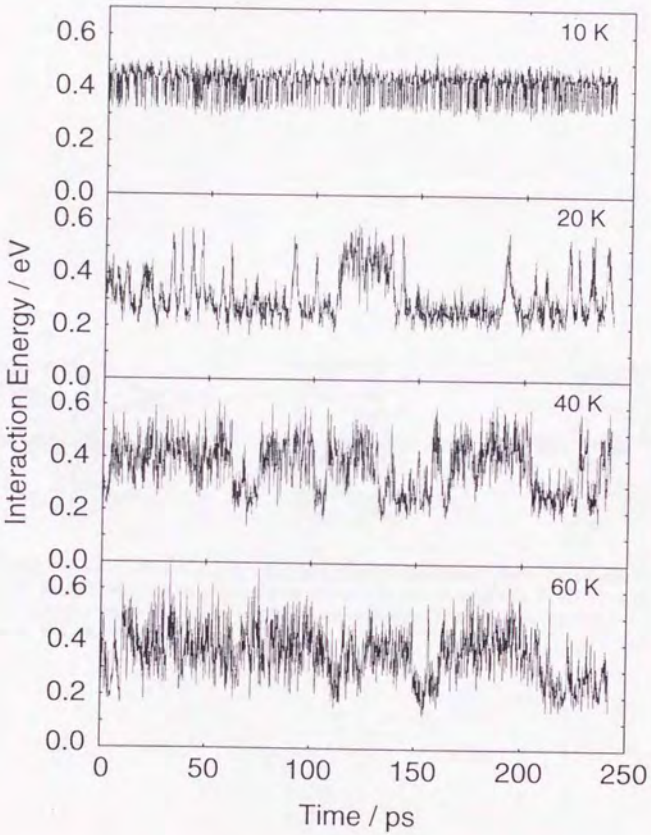

Figure 4.10: A single long trajectory of Ar_{14}^{+} is calculated up to 242 ps, and the variation of the interaction energy is plotted as a function of time. The internal energy is 10K, 20K, 40K, and 60K from top to bottom.

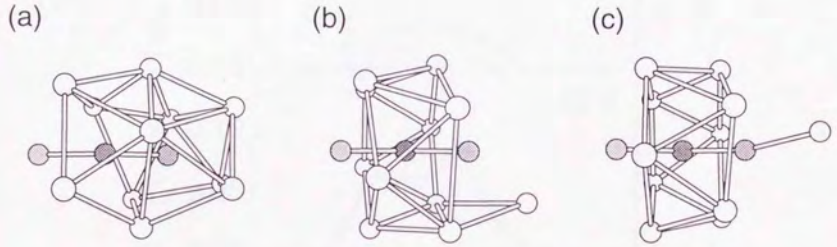

Figure 4.11: Some typical structures of Ar_{14}^{+}. The dark color of the atoms reflects the charge density on them. (a) The structure at 10 K with the large interaction energy. (b) The structure at 20 K with a small interaction energy. (c) The structure at 20 K with the large interaction energy. The bonds connecting between the solvent atoms are drawn as a guide of eyes.

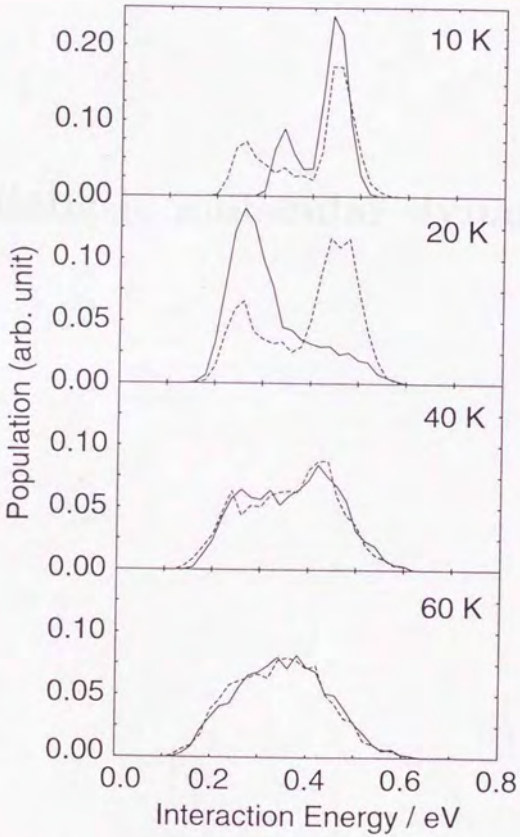

Figure 4.12: The distribution of the interaction energy between the core state and the solvent state. The distribution for the single long trajectory is plotted in a solid line, while that calculated from the ensemble of short trajectories (used in the calculation of the spectra) is plotted in a broken line. The internal energies of the trajectories are 10 K, 20 K, 40 K, and 60 K, from top to bottom.

Chapter 5

Non-adiabatic molecular dynamics

Abstract

The non-adiabatic trajectory calculations are performed for the photodissociation process of the argon cluster ion. Two methods, hemi-quantal dynamics and Tully's surface-hopping method, are examined for Ar_3^+, and their results are compared. The Tully's method is applied for Ar_7^+. Velocity distributions of photofragments are calculated for both neutral and ionic fragments, and compared with experimental results.

5.1 Non-adiabatic molecular dynamics

5.1.1 Born-Oppenheimer approximation

We start from the exact quantum treatment of the molecular system. The Schrödinger equation of molecules including the nuclear coordinates is written in the atomic unit as

$$\mathcal{H}\Phi = i\frac{\partial\Phi}{\partial t} \tag{5.1}$$

$$\mathcal{H} = T_N + T_e + V_{ee} + V_{eN} + V_{NN} \tag{5.2}$$

$$\equiv T_N + \mathcal{H}_{el}, \tag{5.3}$$

where $\mathcal{H}$ is the full Hamiltonian of the molecule. The first two terms in $\mathcal{H}$, T_N and T_e, are the kinetic energy parts of nuclei and electrons, respectively:

$$T_N = \sum_A -\frac{1}{2M_A}\nabla_A^2 \tag{5.4}$$

$$T_e = \sum_a -\frac{1}{2}\nabla_a^2, \tag{5.5}$$

where A is an index to atoms, a is an index to electrons, and M_A is a mass of the atom A. The rest of three terms are the Coulombic potentials; V_{ee} for electron-electron, V_{eN} for electron-nucleus, and V_{NN} for nucleus-nucleus term.

$$V_{ee} = \sum_a \sum_b^{a-1} \frac{1}{r_{ab}} \tag{5.6}$$

$$V_{eN} = \sum_A \sum_a \frac{Z_A}{r_{Aa}} \tag{5.7}$$

$$V_{NN} = \sum_A \sum_B^{A-1} \frac{Z_A Z_B}{r_{AB}}, \tag{5.8}$$

where Z_A is an nuclear charge of atom A, and r_{xy} is distance between x and y.

The eigen value and eigen functions of the electronic Hamiltonian, $\mathcal{H}_{el}$, is defined as

$$\mathcal{H}_{el}\Psi_i(q;Q) = V_i(Q)\,\Psi_i(q;Q), \tag{5.9}$$

where the nuclear coordinates Q appear as parameters in the electronic wavefunction Ψ_i. Total wavefunction including the nuclear coordinates is expanded in the set of $\{\Psi_i\}$ as

$$\Phi(q,Q,t) = \sum_i \Psi_i(q;Q)\,\phi_i(Q,t). \tag{5.10}$$

Inserting Eq. 5.10 to Eq. 5.1, multiplying Φ_j from the left, and integrating over the electronic coordinate q, we get

$$\{T_N + (V_j - i\frac{\partial}{\partial t})\}\phi_j = \sum_i \left\{ 2\sum_A \frac{1}{M_A}\langle\Psi_j|\nabla_A|\Psi_i\rangle\cdot\nabla_A\phi_i - \langle\Psi_j|T_N|\Psi_i\rangle\phi_i \right\}. \tag{5.11}$$

In the Born-Oppenheimer approximation, the right hand side of Eq. 5.11 is neglected. This approximation is justified as the right hand side is smaller by a factor of the mass ratio $1/M_A$ than the left hand side. Under the approximation, Eq. 5.11 is rewritten as

$$i\frac{\partial \phi_j}{\partial t} = (T_N + V_j(\boldsymbol{Q}))\phi_j. \tag{5.12}$$

If the electronic state is Ψ_k at $t = 0$,

$$\Phi(\boldsymbol{q}, \boldsymbol{Q}, 0) = \Psi_k(\boldsymbol{q}; \boldsymbol{Q})\phi_k(\boldsymbol{Q}, 0) \tag{5.13}$$

$$\phi_i(\boldsymbol{Q}, 0) = 0, \qquad (i \neq k), \tag{5.14}$$

equation 5.12 is solved as $\phi_{i\neq k}(\boldsymbol{Q}, t) = 0$. In other word, the electronic state does not change eternally under the Born-Oppenheimer approximation.

As is apparent from Eq. 2.75 (p. 14), the non-adiabatic coupling vector d_{ij}, which appears in Eq. 5.11, is not negligible where the difference between V_i and V_j is small. The Born-Oppenheimer approximation will be broken down there, and the electronic transition between Ψ_i and Ψ_j becomes possible.

5.1.2 Dynamics beyond the B-O approximation

Solving a set of Eq. 5.11 to obtain nuclear wavefunctions $\{\phi_i\}$ is still not possible for the large system as clusters. The hybrid method described in this section abandones the full quantum description of the system. Alternatively, the electronic system is drived by the quantum mechanics while the nuclear motion is treated classically.

Assuming the nuclei follow the trajectory $\boldsymbol{Q}(t)$ (calculation of which is discussed later), the electronic state is propagated in time as

$$i\frac{\partial}{\partial t}\Psi_{\mathrm{TD}}(\boldsymbol{q}, t) = \mathcal{H}_{el}(\boldsymbol{q}; \boldsymbol{Q})\, \Psi_{\mathrm{TD}}(\boldsymbol{q}, t). \tag{5.15}$$

Here, the electronic Hamiltonian $\mathcal{H}_{el}$ is indirectly dependent on time through the nuclear coordinate $\boldsymbol{Q}$. The electronic wavefunction Ψ_{TD} is expanded with the diabatic basis set, $\{\Xi_i\}$, as

$$\Psi_{\mathrm{TD}}(\boldsymbol{q}, t) = \sum_i C_i(t)\, \Xi_i(\boldsymbol{q}). \tag{5.16}$$

Inserting Eq. 5.16 into Eq. 5.15, the set of the equation determining $\{C_i\}$ is obtained:

$$\frac{\partial C_k}{\partial t} = -i\sum_i C_i \langle \Xi_k | \mathcal{H}_{el} | \Xi_i \rangle \tag{5.17}$$

The nuclear trajectory is calculated by integrating the classical equations of motion, Eqs. 4.1 and 4.2 (p. 54). In the present work, two schemes are examined to calculate the forces exerted on nuclei, $\boldsymbol{F}_i$: hemi-quantal

dynamics (HQD) method [1] and a method proposed by J. C. Tully [2]. The Tully's method is referred as CSH (coupled surface-hopping trajectory) method, hereafter.

Difference between two methods is in the selection of the electronic wavefunction that determines the motion of the nuclei. In the HQD method, the forces exerted on the nuclei are evaluated by $\Psi_{\rm TD}(t)$ by using the Ehrenfest theorem,

$$\boldsymbol{F}_i = -\langle \Psi_{\rm TD} | \nabla_i \mathcal{H}_{el} | \Psi_{\rm TD} \rangle. \tag{5.18}$$

As the electronic Hamiltonian $\mathcal{H}_{el}$ depends on time through $\boldsymbol{Q}$, $\Psi_{\rm TD}$ propagates in time as a mixture of the adiabatic electronic states, even if a single adiabatic state is taken as an initial state. Therefore, the nuclei move on an averaged adiabatic potential energy surface, and physically meaningless results may be produced, which will be demonstrated later.

In the CSH method, the forces are calculated from the gradient of the potential energy surface for a certain adiabatic state, Ψ_ξ [2]. In other words, the nuclei are restricted to move on the ξ-th adiabatic surface. The electronic state Ψ_ξ is selected statistically from the adiabatic states according to the "fewest switches" algorithm [2] as follows.

To begin with, a trajectory running on an arbitrary ξ-th adiabatic surface is considered. The population of the current adiabatic state Ψ_ξ in $\Psi_{\rm TD}$, a_ξ, is given by

$$a_\xi \equiv |\chi_\xi|^2, \tag{5.19}$$

$$\chi_\xi = \langle \Psi_\xi | \Psi_{\rm TD} \rangle. \tag{5.20}$$

The time dependence of a_ξ is monitored, and the transition to the other adiabatic states is invoked if

$$-\frac{\Delta t \dot{a_\xi}}{a_\xi} > \zeta, \tag{5.21}$$

where ζ is a uniform random number between 0 and 1, Δt is the interval between sequential evaluations of Eq. 5.21, and $\dot{a_\xi}$ is a_ξ differentiated by time, da_ξ/dt.

Once the transition is invoked, $\mathcal{H}_{el}$ is fully diagonalized and a set of adiabatic states, $\{\Psi_i\}$, is obtained. The electronic state $\Psi_{\rm TD}$ is now expanded as

$$\Psi_{\rm TD} = \sum_i \chi_i \Psi_i. \tag{5.22}$$

The time derivative of χ_i is calculated as

$$\frac{d\chi_i}{dt} = \frac{d}{dt}\langle \Psi_i | \Psi_{\rm TD} \rangle \tag{5.23}$$

$$= \langle \frac{d}{dt}\Psi_i | \Psi_{\rm TD} \rangle + \langle \Psi_i | \frac{d}{dt}\Psi_{\rm TD} \rangle. \tag{5.24}$$

Since Ψ_i is indirectly dependent on time through $\boldsymbol{Q}$, the first term may be represented as

$$\langle \frac{d}{dt}\Psi_i | \Psi_{\rm TD} \rangle = \sum_j \langle \nabla_Q \Psi_i | \Psi_j \rangle \dot{Q} \langle \Psi_j | \Psi_{\rm TD} \rangle \tag{5.25}$$

$$= -\sum_j \chi_j \, d_{ij} \cdot \dot{Q}, \tag{5.26}$$

where $\dot{Q}$ is the nuclear coordinate differentiated by time. The second term of Eq. 5.24 becomes, by using Eq. 5.15,

$$\langle \Psi_i | \frac{d}{dt} \Psi_{\rm TD} \rangle = -i \sum_j \chi_j \langle \Psi_i | \mathcal{H}_{el} | \Psi_j \rangle \tag{5.27}$$

$$= -i \chi_i V_i. \tag{5.28}$$

Finally, we get

$$\frac{d\chi_i}{dt} = -\sum_j \chi_j \, d_{ij} \cdot \dot{Q} - i \chi_i V_i. \tag{5.29}$$

The time derivative of a_ξ is calculated from Eq. 5.29 as

$$\dot{a_\xi} = 2\Re \left(\frac{d\chi_\xi}{dt} \chi_\xi^* \right) \tag{5.30}$$

$$= -\sum_{i \neq \xi} X_{\xi \to i}, \tag{5.31}$$

$$X_{\xi \to i} = 2\Re \left(\chi_\xi^* \chi_i \, d_{\xi i} \cdot \dot{Q} \right). \tag{5.32}$$

where χ_ξ^* is the complex conjugate of $\chi_\xi x$. The $j = \xi$ part and the last term of Eq. 5.29 is neglected, as these give pure imaginary numbers. The value $X_{\xi \to i}$ is proportional to the transition probability from the ξ-th adiabatic state to the i-th adiabatic state. In definition, $X_{\xi \to i}$ is real and anti-symmetric; that is, $X_{\xi \to i} = -X_{i \to \xi}$.

Now, the adiabatic state that governs the nuclear motion after the transition is selected by using the following procedure:

(1) An adiabatic state, Ψ_l, is selected from the set of the adiabatic states, $\{\Psi_i\}$. The probability that the state Ψ_l is selected is proportional to $X_{\xi \to l}$. If $X_{\xi \to l}$ is negative, the probability is set to zero.

(2) The nuclei are decelerated (or accelerated) in the direction of $d_{\xi l}$ to compensate the increase (or decrease) of the potential energy from V_ξ to V_l. This step is necessary for the energy conservation rule to hold. If the available kinetic energy is less than $V_l - V_\xi$, the transition from Ψ_ξ to Ψ_l is ignored and the trajectory calculation is continued on the ξ-th adiabatic state.

(3) A further transition from Ψ_l has to be considered next, because even if $X_{\xi \to l}$ is positive, $\dot{a}_l$ could be negative. Such a state is improper to be selected, as the transition is invoked by watching the reduction of a_ξ, and the reduction of a_ξ requires a_l to increase. The probability to remain on Ψ_i is given by $\dot{a}_l$, while the probability to invoke a further transition to Ψ_m is $X_{l \to m}$. The negative probability is treated as zero, as in the first step. When the further transition to Ψ_m is determined, then replace ξ with l and l with m, and go back to step 2. Otherwise, the trajectory calculation is restarted on the l-th adiabatic state.

In the original prescription proposed by Tully, the variation of the projection of $\Psi_{\rm TD}$ onto every adiabatic states, $\{\chi_i\}$, are monitored in time to determine whether or not the non-adiabatic transition takes place [2]. This procedure requires full diagonalization of $\mathcal{H}_{el}$ at every steps. To avoid the diagonalization, the original prescription is slightly modified as described above. In the present work, the adiabatic state Ψ_ξ, which is necessary to calculate ξ, is obtained with the inverse iteration method associated with the Cholesky decomposition of the Hamiltonian matrix. The initial value in the iteration is taken from the previous time step, and the origin of the energy is properly shifted to accelerate the convergence. The derivative of ξ with time is numerically evaluated by using the 3rd order Newton backward difference formula:

$$\frac{d}{dt}a_\xi(t) \simeq \frac{1}{h}\left\{\frac{11}{6}a_\xi(t) - 3a_\xi(t-h) + \frac{3}{2}a_\xi(t-2h) - \frac{1}{3}a_\xi(t-3h)\right\}, \tag{5.33}$$

where the time step h is taken as same as the integral step in Eqs. 4.3 and 4.4 (p. 55). Thus, the full diagonalization of $\mathcal{H}_{el}$ is required only when the non-adiabatic transition is invoked.

With the procedure above, the swarms of trajectories are branched into the adiabatic states, $\{\Psi_i\}$, with branching ratios proportional to a_i. The following two simple examples verify the validity of the procedure:

Case 1 A linearly-connected three-state model shown in Fig. 5.1a is examined first. We assume that the transition probabilities between the pairs of the states satisfy the following relations: $0 < X_{2\to3} < X_{1\to2}$, and $X_{1\to3} = 0$. The initial trajectories are on the state Ψ_1, that is, $N_1(0) = N$ and $N_2(0) = N_3(0) = 0$, where $N_i(t)$ is the number of trajectories running on Ψ_i at time t. N is the total number of trajectories, $N = N_1 + N_2 + N_3$, and is constant. In terms of a_i (the probability staying on the state Ψ_i), the initial condition is $a_1(0) = 1$ and $a_2(0) = a_3(0) = 0$. In this model, the number of trajectories on Ψ_1, $N_1(t)$, decreases with time; its rate follows Eq. 5.21 as

$$\frac{dN_1}{dt} = N_1\frac{\dot{a}_1}{a_1}. \tag{5.34}$$

The solution of this equation is simply

$$N_1(t) = Na_1(t). \tag{5.35}$$

Following the first step of the procedure, only Ψ_2 is the candidate for the state to be jumped non-adiabatically. From the third step, the branching ratio of staying on Ψ_2 versus the transition further to Ψ_3 is $\dot{a}_2/(\dot{a}_2 X_{2\to3})$ as shown in Fig. 5.1a. Therefore, the number of trajectories on Ψ_2 changes with time as

$$\frac{dN_2}{dt} = -\left(\frac{dN_1}{dt}\right)\left(\frac{\dot{a}_2}{\dot{a}_2 + X_{2\to3}}\right). \tag{5.36}$$

By inserting Eqs. 5.31 ($\dot{a}_1 = -X_{1\to2}$ and $\dot{a}_2 = X_{1\to2} - X_{2\to3} > 0$) and (5.35) in the Eq. 5.36, we have

$$\frac{dN_2}{dt} = N\dot{a}_2. \tag{5.37}$$

The number of the trajectories on Ψ_3 increases monotonously, as no out-flow from the third state is allowed. The rate equation is

$$\frac{dN_3}{dt} = -\left(\frac{dN_1}{dt}\right)\left(\frac{X_{2\to 3}}{\dot{a}_2 + X_{2\to 3}}\right), \tag{5.38}$$

and by inserting Eqs. 5.31 ($\dot{a}_1 = -X_{1\to 2}$ and $\dot{a}_3 = X_{2\to 3}$) and 5.35 in the Eq. 5.38, we have

$$\frac{dN_3}{dt} = N\dot{a}_3. \tag{5.39}$$

Thus, consistency between the numbers of trajectory (N_i) and the probability of the state (a_i), $N_i(t) = Na_i(t)$, always holds. This result is not trivial.

Case 2 A cyclically-connected three-state model defined in Fig. 5.1b is examined next. The transition probabilities are assumed to satisfy the inequality, $0 < X_{3\to 1} < X_{2\to 3} < X_{1\to 2}$. The initial conditions are the same as in case 1. For the first state, Ψ_1, we have the same equation as in case 1;

$$\frac{dN_1}{dt} = N_1\frac{\dot{a}_1}{a_1}. \tag{5.40}$$

For the rate equations of Ψ_2 and Ψ_3, we have a sum over an infinite series as

$$\frac{dN_2}{dt} = \sum_{n=0}^{\infty} -N_1\frac{\dot{a}_1}{a_1}\left(\frac{X_{2\to 3}}{\dot{a}_2 + X_{2\to 3}}\frac{X_{3\to 1}}{\dot{a}_3 + X_{3\to 1}}\right)^n \frac{\dot{a}_2}{\dot{a}_2 + X_{2\to 3}} \tag{5.41}$$

$$\frac{dN_3}{dt} = \sum_{n=0}^{\infty} -N_1\frac{\dot{a}_1}{a_1}\left(\frac{X_{2\to 3}}{\dot{a}_2 + X_{2\to 3}}\frac{X_{3\to 1}}{\dot{a}_3 + X_{3\to 1}}\right)^n \frac{X_{2\to 3}}{\dot{a}_2 + X_{2\to 3}}\frac{\dot{a}_3}{\dot{a}_3 + X_{3\to 1}}. \tag{5.42}$$

By inserting Eq. 5.31, the sum can be easily evaluated and we have $N_i = Na_i$ again.

With the above modification, the CSH method becomes practical for studying multi-level non-adiabatic processes with many degrees of freedom such as the Ar_n^+ ($n > 3$) system.

5.1.3 Comparison between HQD and CSH method

The HQD and CSH methods described above are applied to the strongly non-adiabatic system to examine their credibility. On the potential energy surfaces of Ar_3^+, there is a conical intersection between the electronic ground state (Ψ_0) and the first excited state (Ψ_1) in a C_{2v} conformation (see Fig. 5.2b). The initial conditions for the trajectory calculations are artificially to be set up to examine the non-adiabatic transition near the conical intersection.

In the examples shown here, the initial geometry has C_{2v} symmetry with 2.6 Å of the bond lengths and 130° of the bond angle. The initial electronic state is the first excited adiabatic state, Ψ_1. About 0.1 eV kinetic energy is deposited at $t = 0$, and the trajectories are pursued 20000 integration steps ($\sim$ 1 ps). All other details of the numerical procedure are the same as those described in the section 5.2.3.

The results of the HQD and CSH calculations are summarized in Figs. 5.3 and 5.4, respectively. As is seen in Fig 5.3c, the sudden changes of the HQD wavefunction are found at $t \simeq 0.14$, 0.30, and 0.46 ps. At $t \simeq 0.14$ ps, the non-adiabatic interaction is relatively small, and $\Psi_{\rm TD}$still maintains the character of Ψ_1. At $t \simeq 0.30$ ps, the interaction is large enough that the transition to Ψ_0 practically takes place. At $t \simeq 0.46$ ps, however, the interaction is not large enough and the back-transition to Ψ_1 ends only halfway, so that $\Psi_{\rm TD}$ becomes the mixture of Ψ_0 and Ψ_1 hereafter. The energy expectation value of $\Psi_{\rm TD}$(the solid line in Fig. 5.3b) reflects the character of the HQD wavefunction, and eventually it becomes the middle of the V_0 and V_1. As shown in Fig. 5.3a, one of the bond length oscillates periodically while the residual atom dissociates monotonously after $t \simeq 0.46$ ps, which indicates the dimer formation. However, the dimer vibrates on an averaged potential energy surface of V_0 and V_1; V_0 is strongly bound while V_1 is weakly dissociative. Thus, the resulting HQD trajectory is rather meaningless as was correctly pointed out by Tully [2].

On the other hand, in the CSH calculation, the transition from Ψ_1 to Ψ_0 occurs only once at $t \simeq 0.12$ ps, as seen in Fig. 5.4c. The nuclear motion is governed by Ψ_0 after the transition, that is, a dimer is formed at this point. The dimer vibrates definitely on the potential energy surface of the adiabatic electronic ground state, and thus the trajectory is qualitatively different from that of the HQD calculation. In the trajectory shown in Fig. 5.4a, the center atom and one of the outer atoms form a dimer ion. If we run many trajectories, however, the timing of the non-adiabatic transition changes with the sequence of random numbers in Eq. 5.21, and thus the final product does. For example, a dimer ion can be formed from both of the side atoms, or a meta-stable triangular Ar_3^+ can be formed, even if the trajectories start from the identical initial condition. These various dissociation pathways cannot be considered separately in the HQD calculation, but, in some sense, they are averaged.

5.2 Photodissociation dynamics of Ar_3^+

5.2.1 Introduction

The structures and dynamics of argon cluster ions have attracted extensive attention both experimentally and theoretically [3–26]. A positive hole is thought to be localized on an ion core formed of either two or three atoms in the cluster ion. The rest of the atoms solvate the ion core. In the precedent chapters, we have shown that the size effects on the photoabsorption spectra observed in the cluster ions [11,12] can be explained in terms of the solvent effect, even though the solvent and solute consist of the same elements. In several theoretical studies, the diatomic ion, Ar_2^+, is assumed to be the ion core [3–6], because of its large binding energy (1.33 eV [27]), and a few experimental results have been analyzed in terms of this dimeric ion core model [17,18]. On the other hand, many recent theoretical and experimental studies strongly suggest that the trimer is the ion core in the

Ar cluster rather than the dimer [7–12]. Under the impulse of these studies, the electronic structures and the photodissociation dynamics of Ar_3^+ have been studied extensively.

The photoabsorption spectrum of Ar_3^+ has been observed by several groups [20–22]. There is a strong visible band near the wavelengths of $480 \sim 540$ nm [21,22] and a relatively weak UV band near $270 \sim 310$ nm [20]. The trimer ion dissociates into $Ar^+ + 2Ar$ by excitation of either band. The velocity distribution of Ar^+ fragments produced by excitation of the visible band has been determined experimentally [17–19,23]. A bimodal distribution is clearly observed; $75 \sim 90$ % of the Ar^+ fragments produced have a kinetic energy of about 0.4 eV (fast fragment) while the rest of $25 \sim 10$ % have almost zero kinetic energy (slow fragment). The ratio of the slow fragments to the fast ones increases with the excitation energy [19,23].

On the basis of the theoretical calculations, the visible band is assigned to $^2\Sigma_g^+ \leftarrow 1^2\Sigma_u^+$ [10,24,25]. The equilibrium structure of the electronic ground state ($1^2\Sigma_u^+$) is linear [7–10,15–17], so that the fast Ar^+ fragment is produced from the side atoms of Ar_3^+ while the slow Ar^+ fragment is produced from the central atom. However, if the dissociation proceeded adiabatically, no slow Ar^+ fragment should be produced, because the central atom possesses no charge in the excited state ($1^2\Sigma_g^+$). Therefore, the experimental observation implies that non-adiabatic transition to the other electronic states must occur during the course of the dissociation. To simulate the photodissociation process of Ar_3^+ consistently, the non-adiabatic molecular dynamics, namely, the HQD and CSH methods are applied.

5.2.2 Sampling of the initial conditions

The initial geometries and momenta for the HQD and CSH calculations are sampled from the classical trajectories on the electronic ground state of Ar_3^+. The geometries and momenta are assumed not to be changed by the electronic excitation. In the classical trajectory calculations on the ground state, the internal energy is deposited among 4 vibrational and 2 rotational motions so that the micro-canonical temperature of Ar_3^+ becomes 100 K. The details of the numerical methods are given in the section 4.2.1 (p. 54). The equilibrium structure of Ar_3^+ in the electronic ground state is symmetric linear, but it is very floppy and several vibrational quanta are thermally excited [7, 10, 19, 25, 26]. The classical sampling method is justified in this way. From 20 trajectory runs, 1000 points are sampled for the initial geometries and momenta. Though the number of the sampled points is not very large, it is sufficient because of simplicity of the potential energy surface of the ground state.

The first, third, seventh, and eighth excited electronic states are selected as the initial electronic states of the trajectory calculations. The first, third, and seventh excited states correspond to $1^2\Pi_u$, $1^2\Sigma_g^+$, and $2^2\Pi_u$ in $D_{\infty h}$ geometry, and have considerable oscillator strengths between the ground state ($1^2\Sigma_u^+$) in the visible region [10]. The eighth excited state, which corresponds to $2^2\Sigma_u^+$ in $D_{\infty h}$ geometry, has a comparable oscillator

strength, but the absorption band appears in the UV region. The photoabsorption spectrum is calculated from the sampled points by using the method described in the section 4.2.2, and shown in Fig. 5.5. The wavelength resolution of the spectrum is 30 nm. The experimental spectrum [20,21] is also shown by square and diamond symbols in the figure. The calculated spectrum is in good agreement with the experimental one, although neither of the peak position nor the peak height are adjusted. This agreement guarantees the credibility of the current model.

5.2.3 Trajectory calculations

The HQD and CSH methods are used for the non-adiabatic trajectory calculations. Equations 4.1, 4.2 and 5.17 are numerically integrated by using the fourth/fifth order Adams' formula (see Eqs. 4.3 and 4.4 on p. 55). As the electronic coefficients $\{ C_i \}$ in Eq. 5.17 oscillate rapidly with time, the integration time step must be as short as 0.05 fs. The intermediate representation to accelerate the integration [1] does not work properly in the present case, because some of the off-diagonal elements $(\mathcal{H}_{el})_{ij}$ are as large as the energy difference of the corresponding diagonal elements, $(\mathcal{H}_{el})_{ii} - (\mathcal{H}_{el})_{jj}$. In the CSH method, the equation 5.21 is evaluated every four integration steps to facilitate the numerical derivative of a_ξ (Eq. 5.33).

Starting from the initial conditions described in the previous section, each trajectory is pursued for 10000 integration steps, which corresponds to *ca.* 0.5 ps. The potential energy surfaces of the excited states are all repulsive, and 0.5 ps is long enough for the fragments, $Ar^+ + 2Ar$, to separate far away each other. The statistical averages of some physical properties are evaluated at the end-points of the trajectories, and they are summarized in tables 5.1 and 5.2. The averages are taken with a weight factor proportional to the oscillator strength between the ground and excited states at the initial geometry.

The velocity distributions of the ionic and neutral fragments are shown in Figs. 5.6 and 5.7 for the HQD and CSH calculations, respectively. The velocity of the center of mass is taken as zero. The resolution of the velocity distribution spectrum is 0.1 km/s. In HQD, $\Psi_{\rm TD}$ is expanded in terms of the adiabatic states at the end of the trajectory, and the charge distribution over the fragments is evaluated with the adiabatic wavefunctions. In CSH, Ψ_ξ at the end of the trajectory can be used directly to evaluate the charge distribution. As experimentally reported [16–19,23], the bimodal velocity distribution of the Ar^+ fragment is clearly seen in both the HQD and the CSH distribution spectra for the third, seventh, and eighth excited states. The calculated velocity distribution of the neutral fragments is also bimodal, which has also been observed experimentally [16]. The peak positions of the slow and fast neutral fragments are equal to those of the corresponding ionic fragments. The kinetic energy of the fast fragments are 0.41 eV, in agreement with the experiments [16–19]. The ratio of the slow to the fast neutral fragments is different from that for the ionic fragments, because one dissociation event produces two neutral Ar atoms and one Ar^+ ion.

5.2.4 Discussion

Photoabsorption spectrum

As shown in fig. 5.5, the major excited state in the visible absorption band is the third excited state. The first and seventh excited states, however, have considerable contribution to the spectrum, in the longer and shorter wavelength, respectively. Both excited states have $^2\Pi_u$ symmetry, and therefore the optical transition from the ground state, $1^2\Sigma_u^+$, is forbidden in $D_{\infty h}$ geometry. The optical transition becomes allowed mainly by bending vibration [10, 25] (see Fig. 2.4 in p. 24), so that they are enhanced when the cluster temperature is increased. Experimentally, a shoulder has been observed in the absorption spectrum of Ar_3^+ at the longer wavelength, $545 \sim 555$ nm [21, 22]. Chen *et al.* [22] have noted that the shoulder is enhanced as the temperature of the cluster increases. Therefore, this shoulder can be assigned to the transition from the ground state to the first excited state [25]. It should be noted that fourth and fifth excited states, both of which correspond to $1^2\Pi_g$ in $D_{\infty h}$ geometry, have almost zero oscillator strength from the ground state [10], and do not contribute to the spectrum.

The transition to the eighth excited state, which is $2^2\Sigma_u^+$ in $D_{\infty h}$ geometry, also becomes allowed by vibrational excitations. In this case, the antisymmetric stretching mode plays an important role (see Fig. 2.4 in p. 24). The potential surface of the ground electronic state is very flat along this coordinate, and several vibrational quanta can be readily excited. Therefore, the UV band is also expected to enhance when the temperature of the cluster increases. The position of the absorption band at $280 \sim 300$ nm in Fig. 5.5 is in good agreement with the experimental spectrum [20]. It should be emphasized that the asymmetric linear conformer $(Ar\,Ar)^+Ar$, which DeLuca and Johnson claimed [20], is unnecessary to explain the UV band.

Photodissociation dynamics

As shown in Figs. 5.6 and 5.7, the HQD and CSH methods give similar results on the velocity distributions of the photofragments, as well as those on some of physical properties listed in Tables 5.1 and 5.2. The CSH method gives the identical result to the HQD method if the nuclei moves on the the same trajectory [2]. Therefore, the agreement of these two results probably arises from the similarity of the nuclear trajectories. It is found in the CSH method that non-adiabatic jumps occur well after the electronic excitation, where the potential surfaces are converged nearly to the dissociation limit. Therefore, the nuclear trajectory is not much affected by the non-adiabatic jumps. On the other hand, the nuclear trajectory is strongly affected by the non-adiabatic jumps in the photodissociation process of the larger clusters, which will be discussed in the section 5.3. In such a case, the CSH method should be used in the trajectory studies, as demonstrated in the section 5.1.3.

The third excited state, which is correlated to $1^2\Sigma_g^+$ in $D_{\infty h}$ symmetry, contributes mostly to the visible photoabsorption spectrum of Ar_3^+. There are two peaks in the velocity distributions of the fragments dissociating

from the third excited state (see Fig. 5.6b and 5.7b). The velocities at both of the peaks are nearly equal to the averaged velocities of the center and the outer atoms shown in Tables 5.1 and 5.2. Therefore, the slow fragments come from the center atom of Ar_3^+ and the fast one from the outer atoms. The hole orbital of the $1^2\Sigma_g^+$ state is the σ_g orbital that has no charge on the central Ar atom, and the state is strongly repulsive on the $D_{\infty h}$ surface. If the dissociation proceeds on this surface without the non-adiabatic jumps, the production of the slow Ar^+ fragment cannot be expected. That is, non-adiabatic jumps are responsible for the production of the slow Ar^+ fragments. It must be noted that $1^2\Sigma_g^+$ cannot be coupled with the other states as long as the symmetry is restricted to $D_{\infty h}$. For example, the non-adiabatic coupling vectors with $^2\Sigma_u^+$ states are aligned to the anti-symmetric vibrational coordinate. Accordingly, the slight asymmetry at the starting point, which is amplified during the dissociation process, is essential in the non-adiabatic transition from $1^2\Sigma_g^+$ state. The similar two peak structure is observed in the velocity distributions of the fragments from the seventh and eighth excited states. In these cases, the fraction of charge on the center atoms is 0.28 and 0.38, respectively, whereas it is expected to be 0.5 in the adiabatic and symmetric dissociation.

On the other hand, the velocity distribution of the fragments from the first excited state shows only one peak. The center atom acquires a comparable velocity with the outer atoms as shown in Tables 5.1 and 5.2. The "bond angle" of the product given in the tables indicates that the bending motion is strongly coupled with the dissociation process. As shown in Fig. 5.2b, the potential surface of the first excited state is unstable toward the bending mode in the excitation region. Therefore, the bending motion is initiated adiabatically on the potential energy surface at the beginning of the trajectory, and a considerable amount of kinetic energy is deposited on the center atom. Note that the bending motion on the ground state has little effect on the velocity distribution, though it is necessary for the optical excitation to the first excited state to be allowed. The same bending-dissociation coupling is also observed in the dissociation from the eighth excited state, but not as large as in the first excited state. In this case, the potential surface is much steeper in the direction of the symmetric dissociation, so that the dissociation proceeds before the cluster starts to bend, and two peaks appear in the velocity distribution. The bending-dissociation coupling is not observed in the dissociation from of the third and seventh excited state, which proceeds almost linearly along the axis.

The ratio of the slow to the fast fragments is evaluated with the HQD trajectories as a function of the excitation wavelength and is plotted in Fig. 5.8. The slow/fast threshold values are 0.9, 1.0, and 1.7 km/s for the third, seventh, and eighth excited state, respectively. All the fragments from the first excited state are regarded as the fast fragments. The resolution of the wavelength is 30 nm. The ratio of the slow Ar^+ fragment decreases with the excitation wavelength, in agreement with experimental results [19,23] shown in the figure. This excitation energy dependence of the ratio suggests the important contribution of the non-adiabatic transitions, because the non-adiabaticity (or diabaticity) is enhanced as the velocities of the nuclei increase. Indeed, the number of the non-adiabatic jumps is nearly proportional to the excitation energy as shown in the

last row of Table 5.2. We can also expect that the ratio depends on the temperature of the clusters. It increases with the temperature of the cluster, as the asymmetric dissociation is crucial in the production of the slow Ar^+ fragment, as mentioned before.

5.2.5 Conclusion

The HQD and CSH methods are applied to the dissociation process of Ar_3^+. Both methods give almost identical results in the applications to the direct photodissociation process of Ar_3^+, where the calculated nuclear paths are similar to each other. The non-adiabatic transitions are shown to be responsible for the production of the slow Ar^+ fragments, which have been observed in the photodissociation of Ar_3^+ by a visible light. The ratio of the slow fragments is calculated as a function of the excitation wavelength and the agreement with experimental results is satisfactory. It is also suggested that the photoabsorption spectrum and the slow to the fast ratio of the photofragment depend on the temperature of the cluster.

5.3 Photodissociation dynamics of larger clusters

5.3.1 Introduction

Several experimental and theoretical studies revealed that the argon cluster ion, Ar_n^+, consists of the trimer ion core, Ar_3^+, and the surrounding solvent atoms [7–16]. The trimer ion has a strong photoabsorption band in the visible region, and it photodissociates into Ar^+ ion and two Ar atoms on the photoabsorption [21,22,28]. So do the larger clusters, but the fragment ion is not always Ar^+, and several small cluster ions are produced as a result of the photodissociation [11,15,16]. All the excited states of these small cluster ions are unstable, so that the fragment ions must be in the electronic ground state. Therefore, the non-adiabatic transitions from the photo-excited state to the ground state are essential in the photodissociation process. In these experimental conditions, no collisions take place during the dissociation processes. Therefore, the transition process to the ground state is a typical example of the intramolecular energy relaxation process.

In this section, the CSH method proposed by J. C. Tully [2] is applied for the photodissociation process of Ar_7^+. The kinetic energy distribution, the angular distribution, and the size distribution of produced photofragments are calculated and compared with the experimental results.

5.3.2 Calculation

Sampling of the initial conditions

The initial configurations and momenta of the nuclei are sampled from the normal molecular dynamics (MD) calculation of the cluster ion in the electronic ground state. The initial internal energies of the trajectories are taken moderately high enough that a few trajectories dissociate through the thermal evaporation of the Ar atoms; the typical microcanonical temperature is $190 \sim 200$ K. After about 6 ps at high temperature, the cooling down process is started. The clusters are cooled down to 40 K, by removing the kinetic energy gradually. The annealing process takes about 15 ps, followed by the normal trajectory calculation for 1.2 ps. After that, 50 structures are sampled with the time interval of 0.1 ps. The total number of 2500 structures are obtained from 50 trajectories generated independently. The details of the numerical methods of the MD calculation is given in the section 4.2.1. The initial electronic state from which the CSH trajectory calculation starts is selected statistically from the adiabatic states. The probability to be selected is made proportional to the oscillator strength of the transition from the ground state.

Trajectory calculations

The photodissociation trajectory is calculated by using the CSH method, followed by the normal MD calculation. At first, each trajectory is evolved with the CSH method for ~ 0.5 ps. At the end of the CSH calculation, it is examined whether the electronic state drops down to the ground state, and whether the ground state is well isolated from all other excited states in energy. If both of the conditions are satisfied, the rest of the trajectory is calculated by using the normal MD calculation, which is much faster than the CSH calculation. Otherwise, the CSH calculation is restarted. The details of the numerical method used in the CSH calculation is given in the section 5.2.3.

5.3.3 Results

One of the photodissociation trajectories of Ar_7^+ is shown in Fig. 5.9. The actual potential energy surface on which the nuclei are moving is plotted in a solid line, while the other adiabatic potential energies are plotted in dashed lines. There are 21 adiabatic states in Ar_7^+, but only the lowest seven states are shown in the figure for clarity. The trajectory starts from the sixth excited electronic state at $t = 0$. After seven non-adiabatic transitions indicated by vertical arrows at the top of the figure, it finally settles down to the ground electronic state, to produce a dimer ion and five neutral atoms. The potential energy starts to oscillate regularly at 1 ps, which reflects the vibration of the dimer ion.

Several snapshots of the trajectory are shown in Fig. 5.10. The atoms labeled as "1", "2", and "3" form a linear Ar_3^+ ion core before the photoexcitation. Just after the excitation, "1" is ejected along the collinear axis

of the ion core ($t = 0.3$ ps), and it flies away. On the other side of the ion core, "3" also tries to escape, but it is blocked by "4" located on the collinear axis, and instead, "4" is slowly ejected along the axis. From 0.3 to 0.9 ps, the rest of the five atoms undergoes several non-adiabatic transitions and charge re-distributions, and finally, the charge is localized on the atoms labeled by "3" and "7" to form the dimer ion.

The photoabsorption cross section of Ar_7^+ is calculated at the starting points of 2500 photodissociation trajectories and plotted in Fig. 5.11. The resolution of the spectrum is 20 nm. To make a meaningful comparison with the experimental results [16], we concentrate on those trajectories such that their excitation energies fall within the range between 2.25 $\sim$ 2.75 eV (450 $\sim$ 550 nm). The region, indicated as a shaded area in the figure, contains 1575 trajectories. Among those trajectories, 13% of them are not completely terminated: 11% still remain in the excited state at 2.7 ps after the photoexcitation, while 2% do drop to the ground state but the internal energy is large enough for further dissociation. The remaining 87% trajectories are terminated normally: 54% produce an Ar^+ fragment ion, while 33% end up with an Ar_2^+ fragment ion.

The kinetic energy distribution of the monomer fragment ion, Ar^+, and that of the neutral fragments are calculated from those terminated trajectories, and are plotted in Fig. 5.12. The kinetic energy of the neutral fragments shows a bimodal distribution as is seen in Fig. 5.12(b). We refer to the components peaked at 0.4 eV as the fast fragments hereafter. The threshold energy is arbitrarily set to 0.2 eV. As shown in Fig. 5.12(a), the fast fragments dominate the distribution of the monomer fragment ion.

The translational energy (a) and the internal energy (b) distributions of the dimer fragment ion are shown in Fig. 5.13. Unlike the monomer ion and the neutral fragments, the dimer fragments carry little translational energy, and its distribution decreases monotonously. A large amount of energy is stored in the vibrational mode, as is evident in Fig. 5.13(b). As the binding energy of the dimer ion is 1.31 eV, the produced dimer ion is considered to be highly vibrationally excited, and besides, its energy distribution is far from the thermal one. Note that the plotted energy is that of the dimer, so that the average energy per atom becomes as large as the kinetic energy of the monomer fragment ion ($\sim$ 0.4 eV).

The angular distributions of the fast component of the monomer fragment ion and the neutral fragments are plotted in Fig. 5.14, as well as that of the dimer fragment ion. The angle is measured between the transition dipole moment of the photoexcitation and the velocity vector of the photofragment. The distribution of the fast monomer ions and that of the fast neutral fragments are anisotropic: they are mainly ejected along the transition dipole moment. The distribution for the dimer ions is isotropic.

5.3.4 Discussion

Excitation energy dependence

In this study, the multi-dimensional and multi-state non-adiabatic dynamics are directly treated. The non-adiabatic transitions are expected to occur more frequently as the nuclear velocity becomes large. In the present case of the photodissociation of Ar_7^+, the nuclear kinetic energy originates from the initial excitation energy, ΔE. To examine the dependence of the dynamics on ΔE, the 2238 normally terminated trajectories among 2500 samples are grouped into three parts: $\Delta E > 2.75$ eV (the left blank area in Fig. 5.11), $2.25 \leq \Delta E \leq 2.75$ eV (the shaded area), and $\Delta E < 2.25$ eV (the right blank area). The excitation energy ΔE and frequency of the non-adiabatic jumps are averaged separately in each part, and summarized in Table 5.3 with the other statistical values. The number of non-adiabatic jumps does become large with the excitation energy, but it is because more jumps are required to go down to the ground state, if the trajectory starts from higher excited states. The number of jumps *per unit time* is almost independent from ΔE. It is probably because the fast fragments are ejected in the early stage of the photodissociation as typically seen in atom '1' of Fig. 5.10. The fast fragments carry away the excess energy, leaving a much-the-same amount of the internal energy in the residuals. Note that the non-adiabaticity is determined by the relative velocities among atoms located within the interacting part of the cluster.

Origin of the fast fragments

The visible photoabsorption band of Ar_3^+ is mainly attributed to the $^2\Sigma_g^+ \leftarrow 1^2\Sigma_u^+$ transition [8,10,21,22,24,25, 28,29]. The transition dipole moment is parallel to the collinear symmetric axis of Ar_3^+, and when it is excited, both of the side atoms attached to the center atom of Ar_3^+ are ejected along the collinear axis. Because the charge is located on both of the side atoms in the photoexcited state $^2\Sigma_g^+$, a fast Ar^+ fragment [15,17,19,23], a fast neutral Ar fragment [16], and a slow Ar fragment are produced on the photoexcitation. These dissociation processes were elucidated in the section 5.2. Note that a few slow Ar^+ fragments are produced through non-adiabatic transitions during the photodissociation.

As discussed in the chapter 3, the photoexcited state of the larger clusters remembers the $^2\Sigma_g^+$ character of Ar_3^+. Naturally, the fast Ar^+ fragment is expected to be produced through the photoexcitation of Ar_7^+ and to be ejected along the transition dipole moment. The fast Ar^+ fragment is, however, no longer a major ionic product of the photodissociation. The non-adiabatic transitions now play a more important role in the photodissociation process of Ar_7^+. Most of the charge carried by the fast escaping atoms as atom "1" in Fig. 5.10 is drawn back to the residual part of the cluster. Fast neutral atoms are thus produced, and the majority of the neutral fragments that constitute the slow component in the velocity distribution are produced from successive evaporation from the residuals. Note that not all the fast neutral fragments originate from either of the two side atoms that

initially form an ion core with the center atom. The number of fast neutral fragments, the number of those originating from an ion core, and their kinetic energies are averaged and summarized in Table 5.4, as well as the number of fast Ar^+ fragments. For excitation energies between 2.25 to 2.75 eV, about 20 % of the fast neutral fragments originate from the solvent atoms. These atoms are likely to be generated from a rear-end collision between the solvent atoms and the atom ejected from an ion core, as atom "4" in Fig. 5.10.

When Ar_7^+ is excited higher than 2.75 eV, 96% of the trajectories produce Ar^+ fragment ions. Nevertheless, only 29% of the trajectories produce fast Ar^+ fragments. It is because when excited higher, ejected atoms from the ion core acquire much kinetic energy, which makes the non-adiabatic transitions (or the charge draw-back process) easier. Indeed, only 16% of the fast Ar^+ fragment originates from the ion core. On the other hand, when excitation energies are between 2.25 and 2.75 eV, 57% of the trajectories produce fast Ar^+ fragments, and 90% of them originate from the ion core. Since 62% of the trajectories end up with Ar^+ fragments, more than 80% of the Ar^+ fragment ions come from the ion core. When the excitation energy is lower than 2.25 eV, almost no Ar^+ fragment is produced. Since the binding energy of Ar_7^+ with respect to $Ar^+ + 6Ar$ is -1.79 eV at 0 K [10], it is energetically improbable to produce Ar^+. Instead, the cluster utilizes the binding energy of Ar_2^+ to evaporate solvent atoms.

Comparison with experiments

Nagata and Kondow observed the kinetic energy distribution of the neutral fragments from their time-of-flight mass spectra [16]. They found a bimodal distribution in the photodissociation of Ar_7^+ at 532 nm (2.33 eV), with an average kinetic energy of the fast components as ~ 0.35 eV. They also estimated the anisotropy parameter β of the fast neutral atoms to be $1.5 \sim 2$, and the number of the fast neutrals ejected per single photodissociation event to be two. The present calculation reproduces the experimental results very well. The average kinetic energy of fast neutral fragments calculated from Fig. 5.12 is 0.38 eV, the angular distribution shown in Fig. 5.14 indicates the positive anisotropy parameter, and the calculated number of fast neutral fragments per trajectory is 1.7.

There is, however, a discrepancy between the present calculation and the experimental result in the branching ratio between monomer ion productions and dimer ion productions, Ar^+/Ar_2^+. The observed branching ratio is almost 0, that is, no Ar^+ fragment ion is observed experimentally, while the calculated one is 1.6 for $2.25 \leq \Delta E \leq 2.75$. Because the branching ratio calculated for $\Delta E < 2.25$ is 0.01 and the one for $\Delta E > 2.75$ is 21.6, it is a steep function of the excitation energy. So that if the energy range were taken narrower around 2.33 eV (532 nm) in the calculations, the branching ratio might be reduced.

5.3.5 Conclusion

The photodissociation process of the argon cluster ion is studied by using the CSH method. The agreements with the experimental observation for the kinetic energy distribution and the angular distribution for the photofragments of Ar_7^+ are satisfactory. For the branching ratio between Ar^+ and Ar_2^+ fragment ion, however, the calculation overestimates the production of Ar^+. The poor resolution of the excitation energy seems to be responsible for the discrepancy, but the dependency of the ratio on the initial conditions of the trajectories, such as the rotational state or the temperature of the cluster, must be examined.

Bibliography

[1] M. Amarouche, F. X. Gadea, and J. Durup, Chem. Phys. **130**, 145 (1989).

[2] J. C. Tully, J. Chem. Phys. **93**, 1061 (1990).

[3] J. J. Sáenz, J. M. Soler, and N. García, Surf. Sci. **156**, 121 (1985).

[4] H. Haberland, Surf. Sci. **156**, 305 (1985).

[5] E. E. Polymeropoulos and J. Brickmann, Surf. Sci. **156**, 563 (1985).

[6] P. G. Lethbridge, G. Del Mistro, and A. J. Stace, J. Chem. Phys. **93**, 1995 (1990).

[7] P. J. Kuntz and J. Valldorf, Z. Phys. D–Atoms, Molecules and Clusters **8**, 195 (1988).

[8] I. Last and T. F. George, J. Chem. Phys. **93**, 8925 (1990).

[9] H. -U. Böhmer and S. D. Peyerimhoff, Z. Phys. D–Atoms, Molecules and Clusters **11**, 239 (1989).

[10] T. Ikegami, T. Kondow, and S. Iwata, J. Chem. Phys. **98**, 3038 (1993).

[11] N. E. Levinger, D. Ray, M. L. Alexander, and W. C. Lineberger, J. Chem. Phys. **89**, 5654 (1988).

[12] H. Haberland, B. von Issendorff, T. Kolar, H. Kornmeier, C. Ludewigt, and A. Risch, Phys. Rev. Lett. **67**, 3290 (1991); Issendorff, H. Kornmeier, W. Orlik, T. Kolar, C. Ludewigt, T. Reiners, and A. Risch, in *Physics and Chemistry of Finite Systems*, edited by P. Jena, S. N. Khanna, and B. K. Rao (Kluwer, Dordrecht, 1992).

[13] W. Kamke, J. de Vries, J. Krauss, E. Kaiser, B. Kamke, and I. V. Hertel, Z. Phys. D–Atoms, Molecules and Clusters **14**, 339 (1989).

[14] G. Gantefŏr, G. Bröker, E. Holub-Krappe, and A. Ding, J. Chem. Phys. **91**, 7972 (1989).

[15] T. Nagata, J. Hirokawa, and T. Kondow, Chem. Phys. Lett. **176**, 526 (1990).

[16] T. Nagata and T. Kondow, J. Chem. Phys. **98**, 290 (1993).

[17] J. T. Snodgrass, C. M. Roehl, and M. T. Bowers, Chem. Phys. Lett. **159**, 10 (1989).

[18] C. A. Woodward, J. E. Upham, A. J. Stace, and J. N. Murrell, J. Chem. Phys. **91**, 7612 (1989).

[19] M. T. Bowers, W. E. Palke, K. Robins, C. Roehl, and S. Walsh, Chem. Phys. Lett. **180**, 235 (1991).

[20] M. J. DeLuca and M. A. Johnson, Chem. Phys. Lett. **162**, 445 (1989).

[21] N. E. Levinger, D. Ray, K. K. Murray, A. S. Mullin, C. P. Schulz, and W. C. Lineberger, J. Chem. Phys. **89**, 71 (1988).

[22] Z. Y. Chen, C. R. Albertoni, M. Hasegawa, R. Kuhn, and A. W. Castleman Jr., J. Chem. Phys. **91**, 4019 (1989).

[23] T. Nagata, J. Hirokawa, T. Ikegami, and T. Kondow, Chem. Phys. Lett. **171**, 433 (1990).

[24] W. R. Wadt, Appl. Phys. Lett. **38**, 1030 (1981).

[25] F. X. Gadea and M. Amarouche, Chem. Phys. **140**, 385 (1990).

[26] H.-U. Böhmer, and S. D. Peyerimhoff, Z. Phys. D–Atoms, Molecules and Clusters **3**, 195 (1986).

[27] R. G. Keesee, and A. W. Castleman, Jr., J. Phys. Chem. Ref. Data **15**, 1011 (1986).

[28] T. Ikegami, T. Kondow, and S. Iwata, J. Chem. Phys. **99**, 3588 (1993).

[29] T. F. Magnera, D. M. Sammond and J. Michl, Chem. Phys. Lett. **211**, 378 (1993).

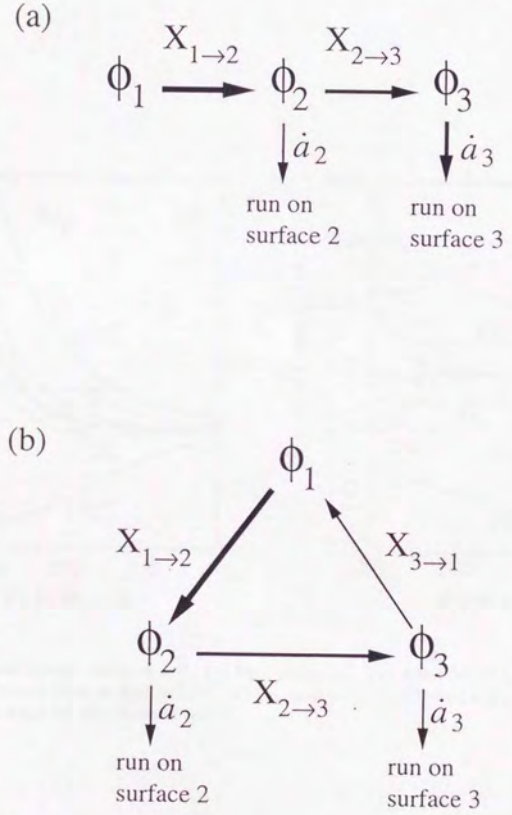

Figure 5.1: Two models to verify the appropriateness of the state-selecting procedure in the CSH method. (a) A linearly-connected three state model, (b) a cyclically-connected three state model.

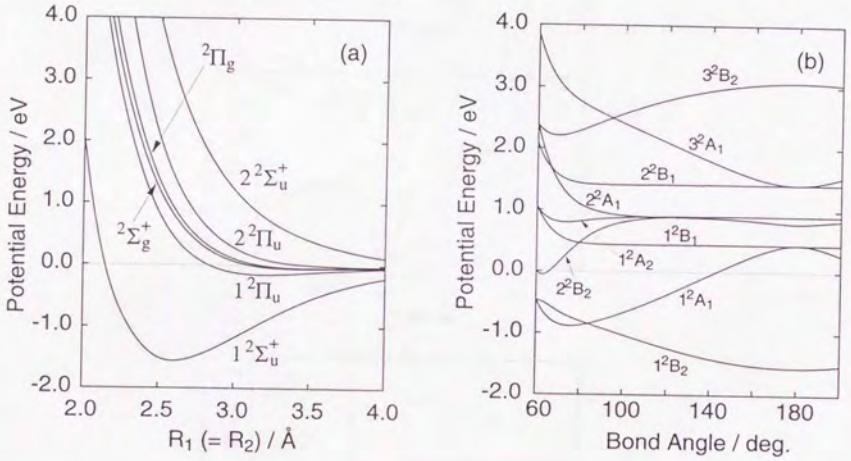

Figure 5.2: DIM potential energy curves of Ar_3^+. (a) $D_{\infty h}$ geometry. Two bond lengths, $R_1 = R_2$, are varied while the bond angle between them is kept at 180°. (b) C_{2v} geometry. Two bond lengths, $R_1 = R_2$, are fixed at 2.6 Å while the bond angle between them is varied.

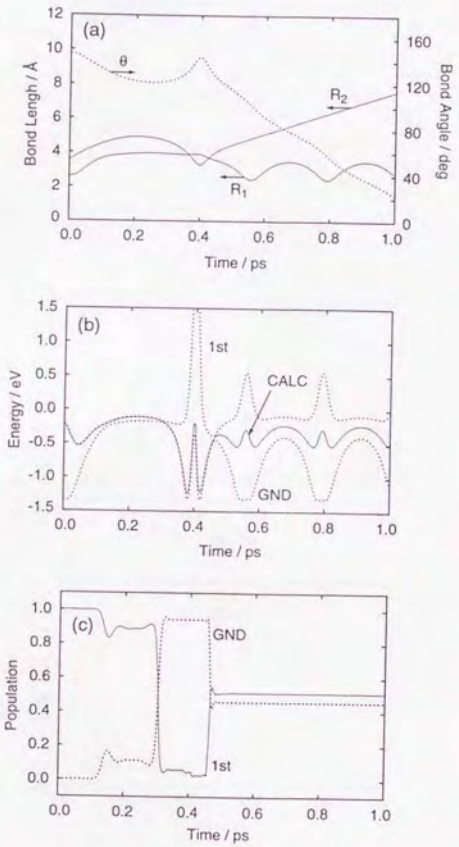

Figure 5.3: One of the representative trajectories calculated by the HQD method. (a) The geometrical parameters are plotted as a function of time. The value R_1 is the bond length between two atoms which forms dimer at the end of the trajectory, R_2 is the distance between the midpoint of the dimer and the other atom, and θ is the angle between R_1 and R_2. (b) The potential energies are plotted as a function of time. The potential energy on which the trajectory is running is drawn by a solid line. The energies of the adiabatic state, V_0 and V_1, are drawn by dotted lines. (c) The squared projections of $\Psi_{\rm TD}$ onto the adiabatic states are plotted as a function of time. The projection onto Ψ_0 and Ψ_1 are drawn by dotted and solid lines, respectively.

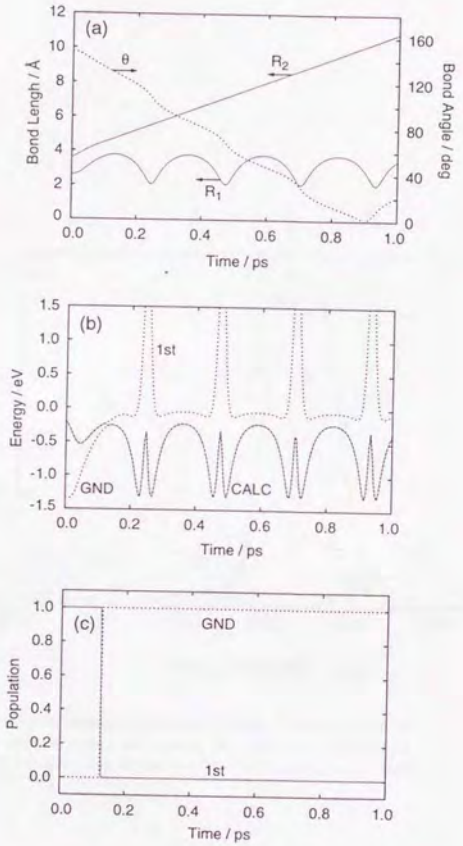

Figure 5.4: One of the representative trajectories calculated by the CSH method. (a) The geometrical parameters are plotted as a function of time. The value R_1 is the bond length between two atoms which forms dimer at the end of the trajectory, R_2 is the distance between the midpoint of the dimer and the other atom, and θ is the angle between R_1 and R_2. (b) The potential energies are plotted as a function of time. The potential energy on which the trajectory is running is drawn by a solid line. The energies of the adiabatic state, V_0 and V_1, are drawn by dotted lines. Before $t = 0.12$ ps, V_1 is the solid line, and then V_0 becomes the solid line. (c) The squared projections of Ψ_{TD} onto the adiabatic states are plotted as a function of time. The projection onto Ψ_0 and Ψ_1 are drawn by dotted and solid lines, respectively.

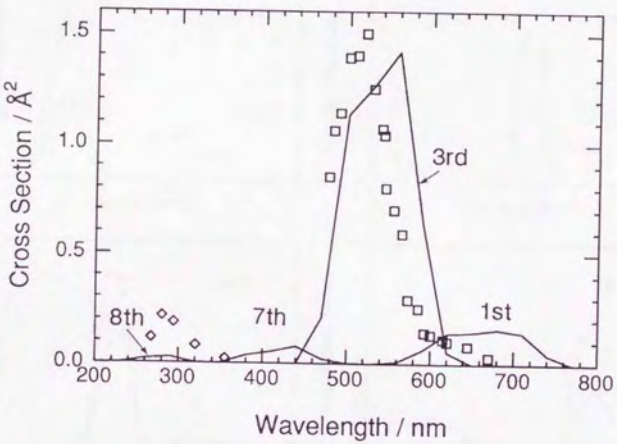

Figure 5.5: The simulated photoabsorption spectrum of Ar_3^+. The transition from the ground state to the first, third, seventh, and eighth excited states are shown. No artificial adjustments such as a normalization in the cross section nor a shift in the wavelength are made. The experimental results are also shown by diamonds (◇) [20] and boxes (□) [21].

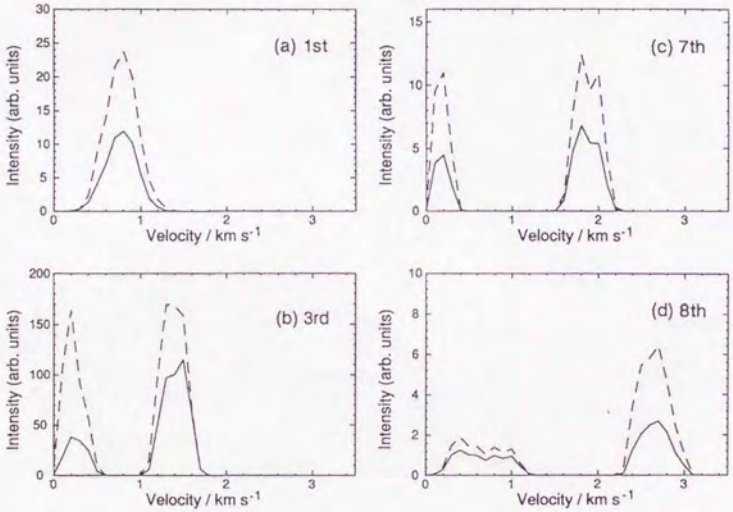

Figure 5.6: The velocity distributions of the photofragments calculated by the HQD method. The solid lines are the velocity distributions of the Ar^+ fragments whereas the broken lines are those of the Ar fragments. The initial electronic states are (a) the first excited state, (b) the third excited state, (c) the seventh excited state, and (d) the eighth excited state.

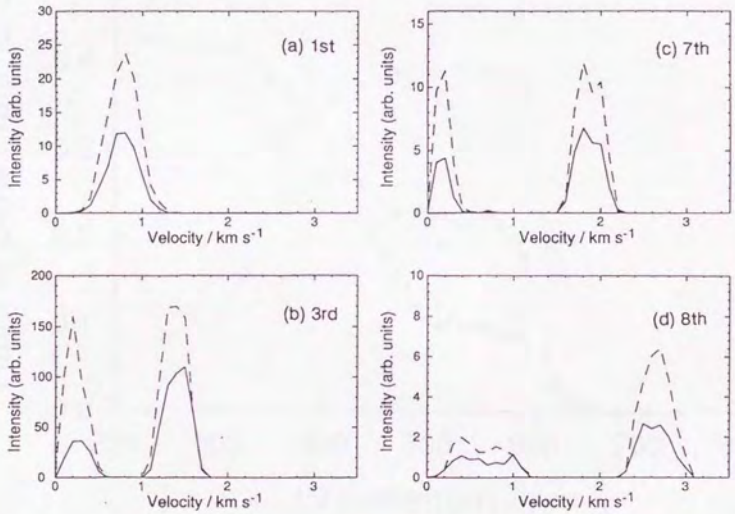

Figure 5.7: The velocity distributions of the photofragments calculated by the CSH method. The solid lines are the velocity distributions of the Ar^+ fragments whereas the broken lines are those of the Ar fragments. The initial electronic states are (a) the first excited state, (b) the third excited state, (c) the seventh excited state, and (d) the eighth excited state.

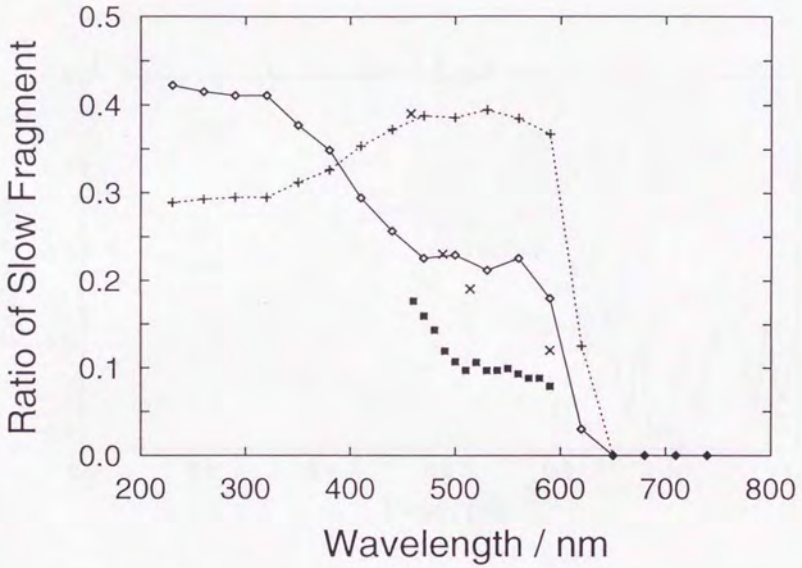

Figure 5.8: The ratio of the slow to the fast fragments as a function of the excitation wavelength. The HQD trajectories are used in the calculation. All the trajectories starting from the first, third, seventh, and eighth excited states are used in the calculation. Diamonds connected with solid lines show the ratio of the ionic Ar^+ fragments, while crosses connected with broken lines are that of the neutral Ar fragments. The filled boxes and X's are the experimental results for the Ar^+ fragments observed by Nagata [23] and Bowers [19], respectively.

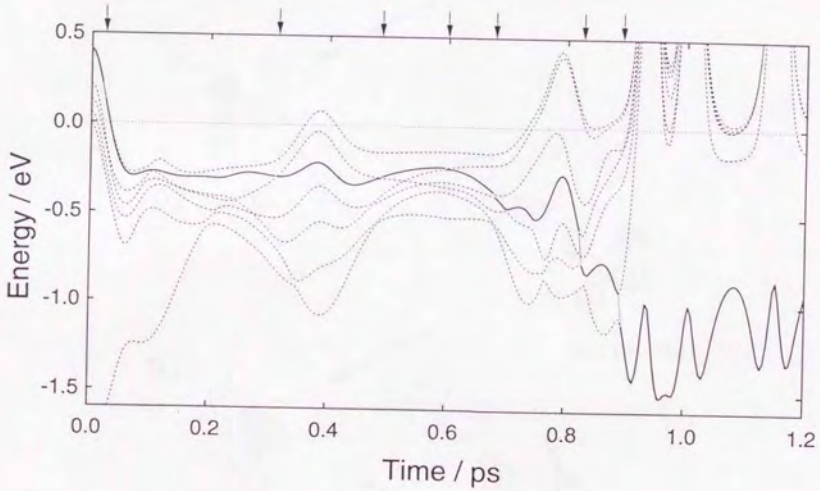

Figure 5.9: The potential energy curve along the photodissociation trajectory of Ar_7^+ is plotted in a solid line as a function of time. The adiabatic potential energies of the lowest seven states are also plotted in dashed lines. The trajectory starts from the sixth excited state at $t = 0$, commits seven non-adiabatic transitions (as indicated by arrows at the top of the figure), and finally settles down in the ground state.

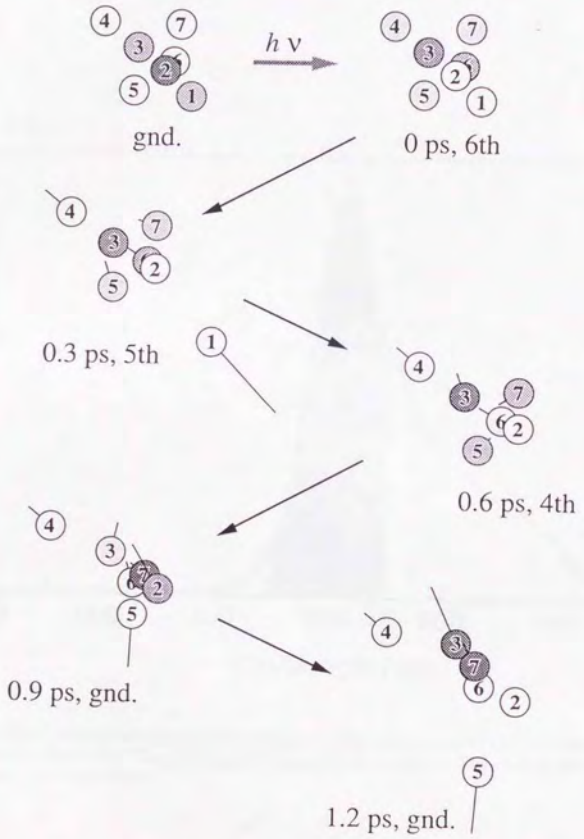

Figure 5.10: The snapshots on the trajectory shown in Fig. 5.9. The darkness on atoms reflects charge density on them. The lines drawn from atoms indicate the velocity, which correspond to the movements in the next 1 ps.

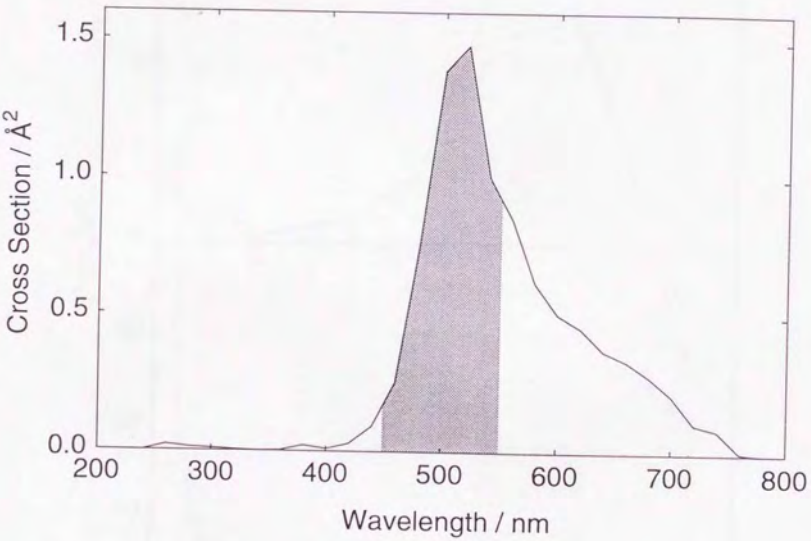

Figure 5.11: The photoabsorption spectrum of Ar_7^+ calculated from the ensembles of the initial configurations for the photodissociation trajectories. The resolution of the spectrum is 20 nm. The shaded area ($2.25 \sim 2.75$ eV) contains 63% of the 2500 trajectories.

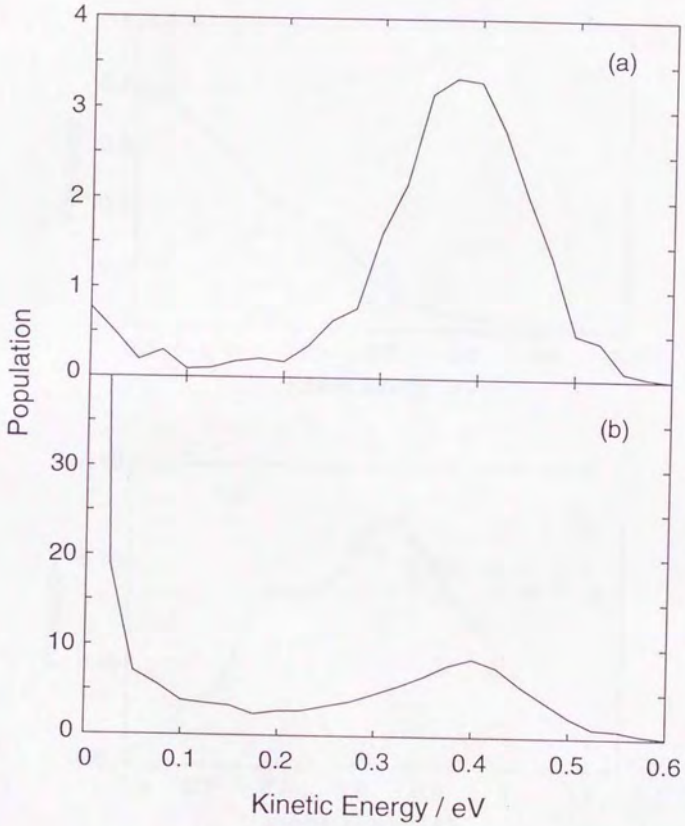

Figure 5.12: Kinetic energy distributions of monomer ions (a) and neutral fragments (b) produced from the photoexcitation of Ar_7^+ between 2.25 $\sim$ 2.75 eV. The distribution of neutral fragments is bimodal, while the distribution of ionic fragments has only the fast component.

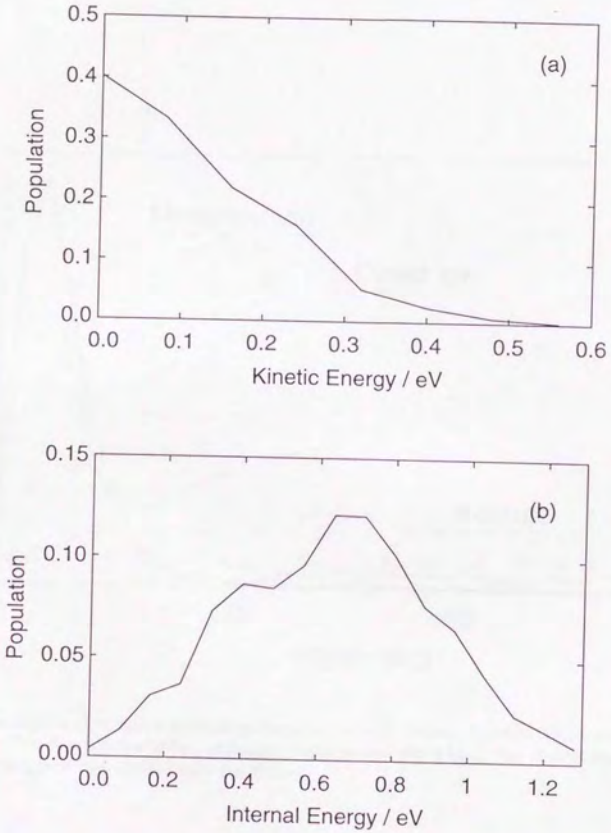

Figure 5.13: The translational (a) and the internal (b) energy distribution of the dimer fragment ion. The rotational energy is included in the internal energy.

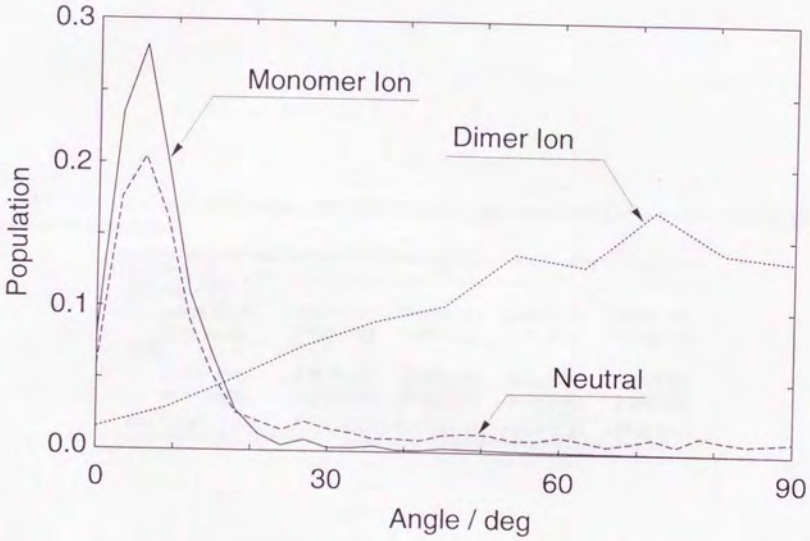

Figure 5.14: The angular distribution of the photofragments of Ar_7^+ around the transition dipole moment of the photoexcitation. The distributions of fast monomer fragment ions (solid line), fast neutral fragments (dashed line), and dimer fragment ions (dotted line) are plotted.

Table 5.1: The averaged final velocities, charges, and bond angles over the HQD trajectories (the standard deviations in parentheses).

initial state	1st	3rd	7th	8th
velocity / km				
center atom	0.76(0.14)	0.23(0.11)	0.19(0.07)	0.64(0.26)
outer atom	0.78(0.19)	1.40(0.13)	1.87(0.13)	2.65(0.16)
charge / e				
center atom	0.38(0.07)	0.22(0.09)	0.29(0.05)	0.41(0.02)
outer atom	0.31(0.07)	0.39(0.18)	0.35(0.08)	0.29(0.09)
bond angle / deg	93.3(18.1)	159.6(11.3)	166.2(6.1)	148.4(16.5)

Table 5.2: The averaged final velocities, charges, and bond angles over the CSH trajectories (the standard deviations in parentheses). The averaged numbers of the non-adiabatic jumps are also shown in the bottom row.

initial state	1st	3rd	7th	8th
velocity / km				
center atom	0.77(0.14)	0.24 ± 0.11	0.19(0.10)	0.64 ± 0.26
outer atom	0.78(0.19)	1.40 ± 0.13	1.87(0.13)	2.65 ± 0.16
charge / e				
center atom	0.39(0.22)	0.22(0.23)	0.28(0.38)	0.38(0.49)
outer atom	0.30(0.23)	0.39(0.31)	0.36(0.42)	0.31(0.46)
bond angle / deg	92.3(17.1)	159.4(11.3)	166.2(7.5)	148.4(16.5)
number of jumps	2.17(1.22)	3.17(1.51)	4.16(1.64)	5.83(3.55)

Table 5.3: Characteristics of the trajectories for the three regions of the excitation energy, ΔE.

Excitation energy /eV	> 2.75	$2.25 \sim 2.75$	< 2.25
No. of trajectories[a]	90	1365	783
Averaged ΔE^b /eV	3.58	2.44	2.04
No. of non-adiabatic jumps	12.4	8.2	4.4
Freq. of non-adiabatic jumps /ps^{-1}	7.6	7.7	7.0
No. of fast fragments[c]	2.25	2.27	2.06
Kinetic energy of fast fragments[3] /eV	0.75	0.38	0.43

[a] Number of the trajectories, which start after the excitation with ΔE and terminate normally.
[b] Averaged excitation energy ΔE over the trajectories.
[c] A fast fragment is defined as the one which have more than 0.2 eV of kinetic energy. Charges on the fragments are not considered here.

Table 5.4: Characteristics of the neutral fragments for the three regions of the excitation energy.

Excitation energy / eV	> 2.75	$2.25 \sim 2.75$	< 2.25
No. of fast neutrals[a]	1.96	1.70	2.05
No. of fast neutrals come from the ion core[b]	1.52	1.35	1.15
Kinetic energy of fast neutrals / eV	0.75	0.39	0.43
No. of fast Ar^+ fragments[c]	0.29	0.57	< 0.01

[a] Total number of fast neutral fragments per one photodissociation event.
[b] Number of the fast neutral fragments originating from the side atoms of the ion core.
[c] Number of fast Ar^+ fragments per one photodissociation event.

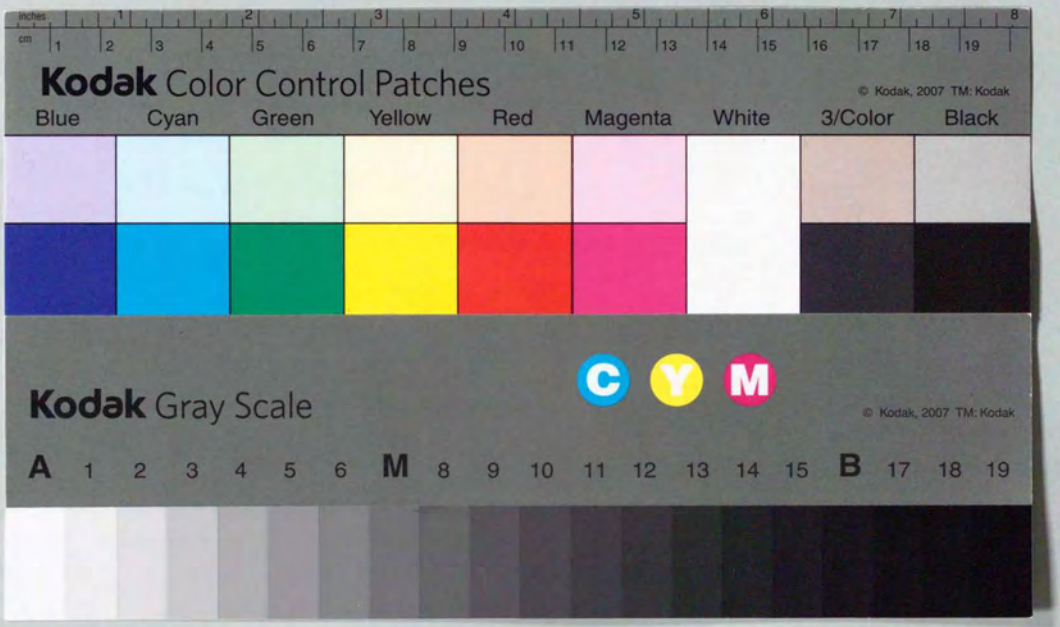
inches
cm
Kodak Color Control Patches
© Kodak, 2007 TM: Kodak
Blue
Cyan
Green
Yellow
Red
Magenta
White
3/Color
Black
Kodak Gray Scale
C
Y
M
© Kodak, 2007 TM: Kodak
A 1 2 3 4 5 6 M 8 9 10 11 12 13 14 15 B 17 18 19